Growth and Characterization of thin Al_2O_3 and Ga_2O_3 Films on Single-Crystalline Ni, Co, and CoGa Substrates

Inaugural-Dissertation

zur

Erlangung des Doktorgrades der

Mathematisch-Naturwissenschaftlichen Fakultät

der Heinrich-Heine-Universität Düsseldorf

vorgelegt von

Arno Wehner
aus Bonn

Dezember 2003

Gedruckt mit der Genehmigung der Mathematisch-Naturwissenschaftlichen Fakultät der Heinrich-Heine-Universität Düsseldorf

1. Referent: Prof. Dr. René Franchy

2. Korreferent: Prof. Dr. Klaus Schierbaum

Tag der mündlichen Prüfung: 30.01.2004

Contents

List of Figures

List of Tables

List of Abbreviations and Acronyms

AES	Auger Electron Spectroscopy
BZ	Brillouin Zone
DOS	Density of States
EELS	Electron Energy Loss Spectroscopy
FEL	Fast Entry Lock
FWHM	Full Width at Half Maximum
GMR	Giant Magneto Resistance
IMFP	Inelastic Mean Free Path
IPE	Inverse Photoemission
IR	Infrared
LDOS	Local Density of States
LEIS	Low energy Ion Scattering
LEED	Low Energy Electron Diffraction
MEIS	Medium Energy Ion Scattering
MIGS	Metal Induced Gap States
MTJ	Magnetic Tunnel Junction
PVD	Physical Vapor Deposition
QMS	Quadrupole Mass Spectrometer
QMB	Quartz Micro Balance
RT	Room Temperature
STM	Scanning Tunneling Microscope / Microscopy
STS	Scanning Tunneling Spectroscopy
TDS	Thermal Desorption Spectroscopy
TEAS	Thermal Energy Atom Scattering
TMR	Tunnel Magneto Resistance
UHV	Ultra High Vacuum
UPS	Ultraviolet Photoelectron Spectroscopy
UV	Ultra Violet
XPS	X-ray Photoelectron Spectroscopy

Chapter 1

Introduction

1.1 Motivation

Surface science was originally a section of solid state physics, but is nowadays established as a research field of its own located at the borderline of chemistry and physics [1]. This is reflected in the dramatic increase of the number of publications. Thereby, surface science is interesting from the perspective of basic research as well as applications such as corrosion, catalysis, or miniaturization of electronic devices.

Since the applications are of considerable economical impact and are present in everyday life (read heads of hard disks, coating of glasses) there is also a public interest, which is reflected by the frequent appearance of the words nanotechnology and information technology in the non-professional press. This in turn leads to improved financial support of this field inducing further growth of the field.

For basic research, e.g., the low dimensionality of surface structures is interesting, because it exhibits effects and properties that are different from those of the bulk material. Once these effects are understood, they can be utilized to deliberately fabricate certain structures for use as devices. This holds equally for the device and the fabrication process (e.g. self assembling).

This work is motivated by the investigation of the tunneling magneto resistance (TMR) effect. A TMR device consists of two ferromagnetic layers that are separated by an insulating layer (tunneling barrier). Devices of this kind show a tunneling current that depends on an externally applied magnetic field. The TMR effect was first observed by Julliere [2]. He measured a TMR of 14% at 4.2 K. Before this time the magneto resistance could only be changed by about 1% at fields as high as 1 Tesla. Renewed interest in magneto resistance effects arose after the discovery of the Giant Magneto Resistance (GMR) by Grünberg [3] and Fert [4]. The discovery of this effect can be seen as the origin of what is called magnetoelectronics. In this new concept the spin of the electron is exploited in

addition to the charge. The TMR also received new interest and magnetic tunnel junctions (MTJs) that exhibit TMR ratios of more than 10% at room temperature were fabricated by Moodera et al. [5], Miyazaki et al. [6], and by Rottländer et al. [7]. The TMR ratio at room temperature of the junctions was further increased in the recent years.

In order to understand the functioning of MTJs, the junctions should be crystalline, because only these are calculable with theoretical methods. Various materials are used as tunneling barriers in MTJs but Al_2O_3 seems to be the most promising.

In this work the aim is to fabricate ultrathin (10-20 Å) Al_2O_3 films that are well ordered on single crystalline ferromagnetic samples (Ni and Co). There should also be no interface layer between oxide film and substrate as is often the case when the Al is not completely oxidized. The preparation of well ordered Al_2O_3 films using ordered intermetallic alloys as a substrate is well established (NiAl(100) [8], NiAl(110) [9], NiAl(111) [10], Ni_3Al(100) [11, 12], Ni_3Al(111) [13, 14]). Aluminum [15] was also used as a substrate as well as other metals (e.g. Ru(0001) [16, 17], Re(0001) [18], Mo(110) [19], Ta(110) [20], Fe(110) [21], and Cu(111) [22]). However, the intermetallic alloys are not ferromagnetic at room temperature and are thus not suitable for use in MTJs. The experience with oxidation of intermetallic alloys can still be used by preparing a surface alloy of Al and a ferromagnetic substrate and subsequent oxidation of this surface alloy. In this way well-ordered alumina layers are prepared on the ferromagnetic substrates nickel and cobalt. Additionally, other methods for growing well ordered alumina films were tested, e.g., the deposition of aluminum in oxygen atmosphere on a ferromagnetic substrate.

The main part of the work deals with the growth and the structural characterization of Al_2O_3 layers on nickel and cobalt. Nickel crystallizes in the fcc structure and the (100) plane was chosen for the substrate in order to have a square lattice on the surface, whereas cobalt is hexagonal at room temperature and the (0001) plane was chosen for the substrate in order to have a hexagonal lattice on the surface. Additionally, electronic transport measurements were performed on the system β-Ga_2O_3 / CoGa(100). The structural properties of this system were previously thoroughly investigated by Franchy and co-workers [23, 24, 25, 26, 27, 28, 29].

1.2 Conception

In Chapter 2 the two UHV machines are introduced. In UHV apparatus 1 the preparation and structural characterization of the ultrathin Al_2O_3-films was performed, using the surface sensitive techniques Auger electron spectroscopy

(AES), low energy electron diffraction (LEED), and high resolution electron energy loss spectroscopy (EELS). In UHV apparatus 2, which is commercially available from Omicron, AES and LEED served only for characterization of the β-Ga_2O_3 / CoGa(100) system. Scanning tunneling microscopy (STM) is used for topographical characterization and the transport measurements were achieved by scanning tunneling spectroscopy (STS). The characterization tools AES, LEED, EELS, and STM/STS are discussed in Chapter 3 in detail. Here, the theoretical background as well as the specific instruments that were used in this work are treated. In chapter 4 the involved materials are introduced. The substrate materials nickel and cobalt are covered as well as the phase diagrams of the intermetallic alloys of NiAl and of CoAl. Also the properties of bulk alumina as well as alumina thin films, that occur in a variety of phases, are discussed. The chapter concludes with a brief discussion of gallium oxide.

The experimental results are presented in the following chapters. Chapter 5 starts with a more detailed motivation to grow alumina films on metallic substrates and an overview of existing studies. In section 5.1 the formation of Ni_3Al as a surface alloy on Ni(100) is presented, and in section 5.2 the oxidation of this alloy at room temperature is investigated. Upon annealing the aluminum oxide becomes well ordered and its structural properties are discussed. Section 5.3 deals with the oxidation of the Ni_3Al/Ni(100) system at 800 K. In section 5.4 the deposition and subsequent oxidation of an Al layer on Ni(100) at room temperature are discussed. In Section 5.5 the deposition of Al in oxygen atmosphere at room temperature is presented. For a deposition rate of $r = 0.48$ Å/min and a partial pressure of oxygen of $1 \cdot 10^{-7}$ mbar an alumina film is grown that contains no unoxidized Al. Annealing of this film results in the formation of γ'-Al_2O_3.

Chapter 6 starts with an outline of existing studies of metals deposited on oxide films. Here the growth of Co on Al_2O_3/Ni(100) is investigated. Co is deposited on γ'-Al_2O_3/Ni(100) at room temperature and afterwards annealed. Co seems to be stable on the alumina film for temperatures below 900 K. For temperatures above 900 K Co diffuses through the oxide into the substrate . After annealing to 1000 K there are Co free areas on the surface and the structural properties of the alumina film are unchanged in comparison to the oxide film before the deposition of cobalt.

Chapter 7 deals with the growth of alumina films on Co(0001). In section 7.1 the deposition and annealing of Al on Co(0001) is studied. It results in the formation of a thin Co_xAl_y alloy on Co(0001). In section 7.2 the oxidation of this alloy at room temperature is presented. Annealing of the oxidized Co_xAl_y/Co(0001) system results in the formation of a well ordered Al_2O_3 film and an interface layer of Co_xAl_y between the alumina film and the substrate. In section 7.3 the deposition and subsequent oxidation of Al on Co(0001) at room temperature is

investigated. Annealing of the oxidized Al/Co(0001) system leads to a well ordered γ'-Al_2O_3 film and an interface layer of Co_xAl_y between the alumina film and the substrate. In section 7.4 the deposition of Al ($r = 0.48$ Å/min) on Co(0001) in oxygen atmosphere of $1 \cdot 10^{-7}$ mbar at room temperature is presented. Annealing of the Al_2O_3 layer results in ordering. There is no evidence for an interface layer between the alumina and the Co(0001) substrate.

In chapter 8 electronic transport measurements are presented and discussed. Section 8.1 deals with measurements of I(V)-curves of the (7x7) reconstructed Si(111) surface. In section 8.2 first the structural properties of the CoGa(100) surface are summarized. Then I(V)-curves of the CoGa(100) surface are presented. In section 8.3 the structural properties of the β-Ga_2O_3/CoGa(100) system are briefly described. Then I(V)-curves are presented and compared to those of the clean CoGa(100) surface.

Chapter 2

The UHV Chambers

In order to study surfaces on an atomic scale, the surface has to be atomically clean for the time of the experiment, typically several hours. Therefore, the number of particles incident on the surface must be reduced, which is the case under vacuum conditions. A straightforward calculation based on the kinetic gas theory results in Table 2.1. Depending on the pressure the time is shown until a surface that contains 10^{15} atoms/cm^2 (see e.g. [30]) is completely covered by a monolayer of atoms or molecules. The calculation applies for a temperature of 300 K and an average molecular/atomic mass of $M_r = 29$ (valid approximately for air).

p[mbar]	10^{-7}	10^{-8}	10^{-9}	10^{-10}	10^{-11}
t	36 s	360 s	1 h	10 h	100 h

Table 2.1: Time until a surface is covered by one monolayer of residual gas for a sticking coefficient of 1.

It can be seen that a pressure less than 10^{-9} mbar is desirable to have a clean sample on a reasonable time-scale. This regime ($p \leq 10^{-7}$ mbar) is called *ultra high vacuum* (UHV). To obtain UHV, in addition to appropriate pumps and chambers a bake-out procedure is necessary. This can also be seen from kinetic gas theory: The time for the reduction of one monolayer of N_2 on a steel surface to 1% of a monolayer is $5.8 \cdot 10^9$ years at T = 300 K (room temperature) and 5 min at T = 600 K. It is suggestive to heat the chamber to temperatures well above room temperature before the experiment.

In the same way "flashing" the sample (annealing to high temperatures for a short time) tends to remove contaminating adsorbants from the surface.

In the following two sections the UHV chambers are described. First UHV apparatus 1 is described in detail, wherein most of the experiments have been

performed. It contains facilities for Auger electron spectroscopy (AES), low energy electron diffraction (LEED), and electron energy loss spectroscopy (EELS), which are discussed in the next chapter in detail. Then the UHV apparatus 2, which is equipped with AES, LEED, and a scanning tunneling microscope (STM), is briefly described. Here only the STM and STS measurements are of relevance and these techniques are also discussed in detail in the next chapter.

2.1 UHV Apparatus 1

The UHV apparatus 1 was mainly used for the growth of the alumina films on the Ni(100) and Co(0001) substrates and the characterization of these films. The chemical characterization with AES and EELS is combined with the structural characterization by LEED. The morphological characterization by STM was performed in UHV apparatus 2.

UHV is achieved by a combination of a turbo molecular pump, a rotary vane pump, and a titanium sublimation pump. The turbomolecular pump is a Pfeiffer TMU 521 (500 l/s for N_2) capable of a base pressure smaller than $1 \cdot 10^{-10}$ mbar after bake out. The rotary vane pump is a Trivac D16B (16 m^3/h) capable of an end pressure smaller than $1 \cdot 10^{-2}$ mbar. These two pumps were connected in series and supported by a titanium sublimation pump. To achieve the base pressure of $8 \cdot 10^{-11}$ mbar the chamber was baked out at 150°-170° for about 24 h. The pressure was measured by a Ionivac IM 510 from Leybold, which allows pressure measurements in the range between $1.5 \cdot 10^{-4}$ mbar and $1 \cdot 10^{-11}$ mbar.

The samples were single crystals cut by spark erosion and mechanically polished to an accuracy of 0.5°. They have a diameter of 8 mm and a thickness of 2.5 mm and are installed into a homemade sample holder, so that the surface normal is parallel to the two levels of the chamber. The sample movement is possible for three translational degrees of freedom and a rotational one via a differentially pumped feedthrough. The feedthrough is pumped by a Trivac rotary vane pump D1.6B (1.6 m^3/h). The manipulator contains heating and cooling facilities, so that the sample can be exposed to temperatures between 25 and 1400 K. Cooling is performed by pumping liquid nitrogen or helium through the manipulator by a membrane pump. Heating is achieved by electron bombardment, whereby the sample is on high voltage (0.8 kV).The temperature is controlled by a (WRe3% / WRe25%) thermocouple directly attached to the backside of the sample.

The gas inlet system can be locked up from the UHV chamber and is separately pumped by a series connection of a Leybold TurboVac 50 molecular pump and a Trivac D8B rotary vane pump.

The chamber has two experimental levels, the upper one of which is shown

in Fig. 2.1. The Auger electron spectrometer (AES) and the low energy electron

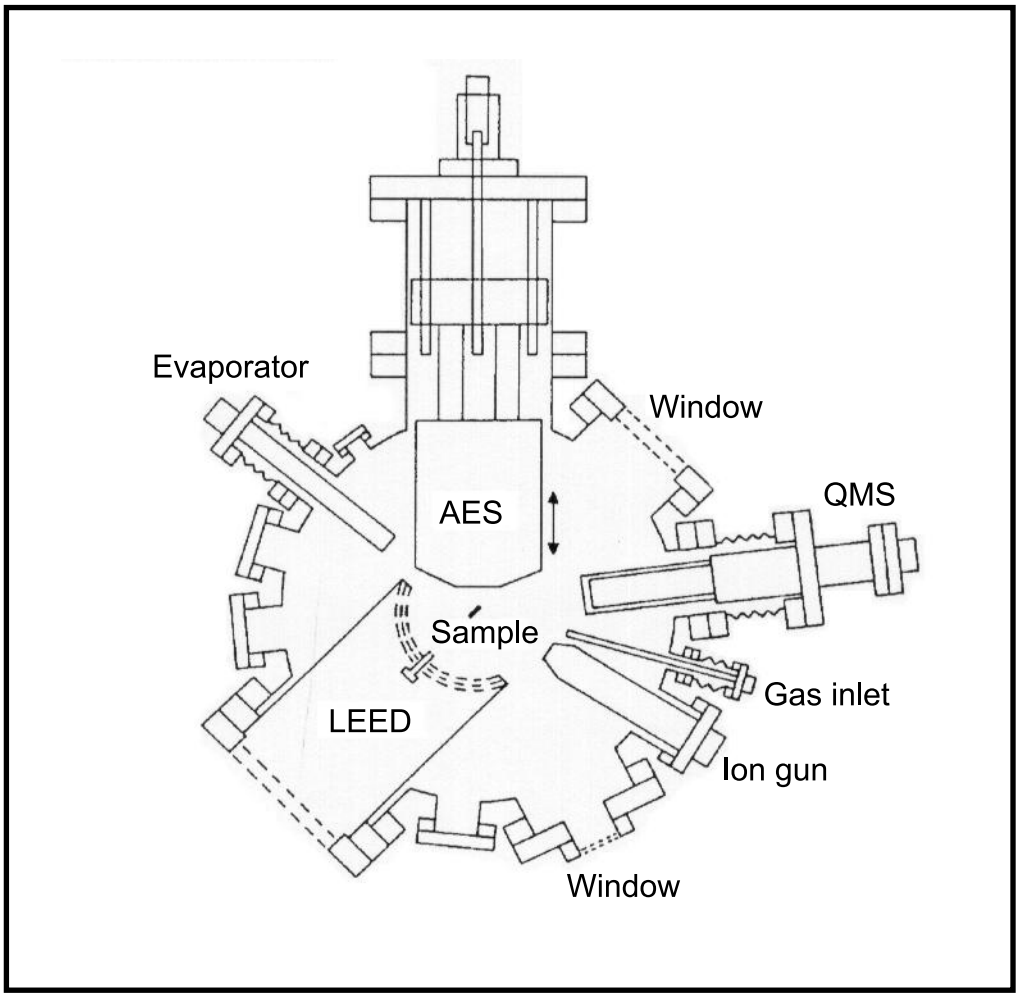

Figure 2.1: *Upper level of UHV1.*

diffraction (LEED) system are described in detail in the next chapter. The ion gun is used for sputtering with Ar^+-ions in order to clean the sample in UHV. It was typically operated at 1 kV with the sample current at $\sim 3\,\mu$A. The quadrupole mass spectrometer (QMS) is a Balzers QMG 311 with the lowest detectable partial pressure of $2 \cdot 10^{-11}$ mbar.

For deposition of cobalt and aluminum an Omicron EFM3T triple evaporator was used. The evaporator is described in more detail in section 2.3

The lower level contains a computer controlled electron energy loss spectrometer (type Ulti 100). The spectrometer is housed in a double-cylinder made of μ-metal to shield it from magnetic fields.

2.2 UHV Apparatus 2

The second UHV apparatus used in this work served mainly for morphological characterization of thin films by scanning tunneling microscopy (STM) and for electronic transport measurements by scanning tunneling spectroscopy (STS). These techniques are discussed in the next chapter. The apparatus was also equipped with a cylindrical mirror analyzer (CMA) for AES and a with LEED optics.

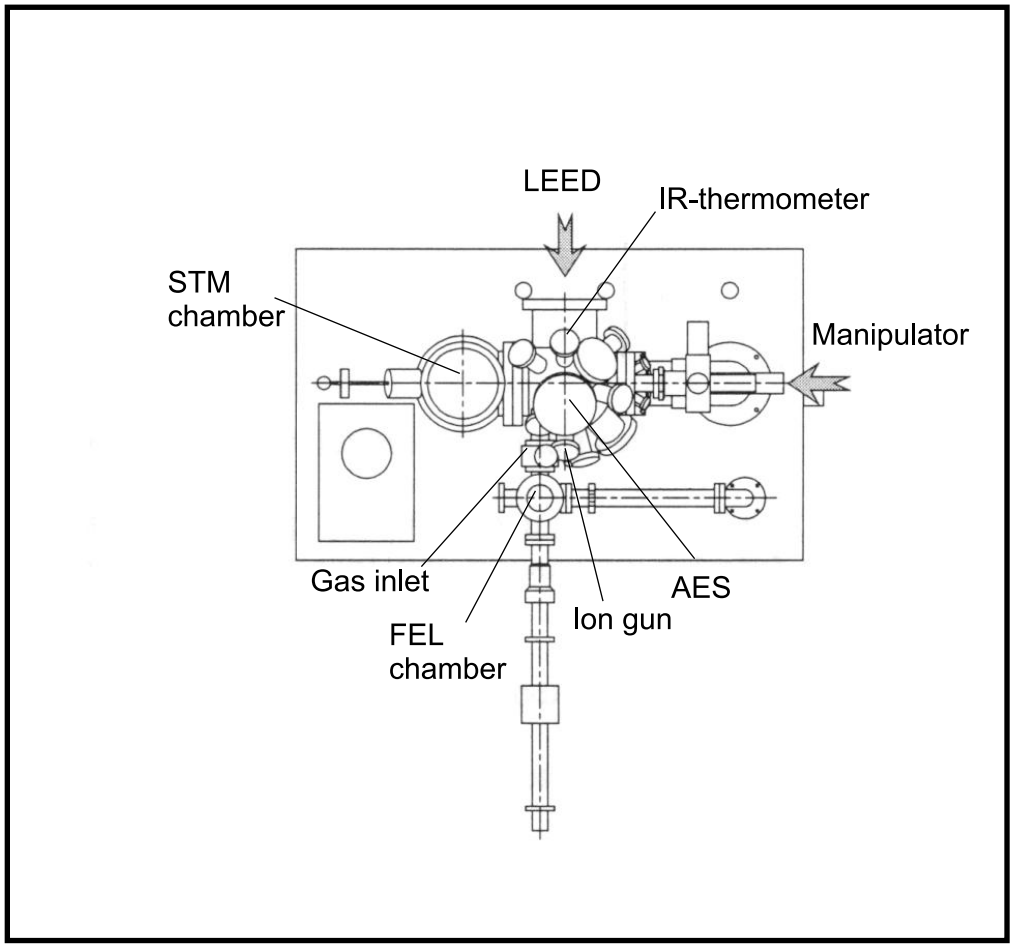

Figure 2.2: *Top view of the Omicron STM chamber (model MULITIPROBE COMPACT).*

The UHV chamber is shown schematically in Fig. 2.2. It is commercially available from Omicron (model MULITIPROBE COMPACT), it consists of three chambers: a fast entry lock (FEL) chamber, a preparation chamber, and an analysis chamber for scanning tunneling microscopy (STM).

The FEL chamber can be locked up from the preparation and analysis chambers. It is separately pumped via a bypass and thus allows introducing samples into the preparation chamber while UHV is maintained.

The preparation chamber is equipped with an ion gun for sputtering in order to clean the sample, a cylindrical mirror analyzer for AES, and a three grid LEED optics. Gases can be introduced into the chamber by a variable leak valve. Heating of the sample is performed by a solid-state heating element made of Si. The temperature was controlled by an infrared (IR) thermometer.

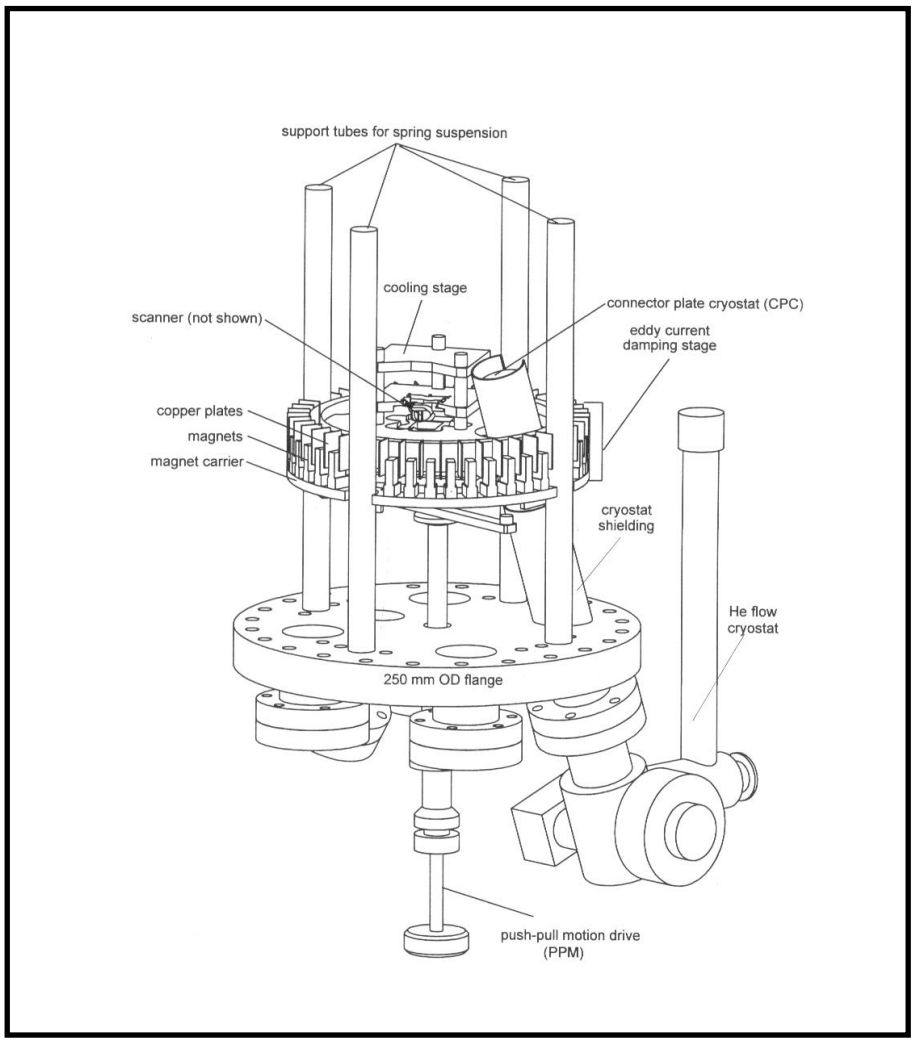

Figure 2.3: *Schematic of the Omicron VT STM.*

The OMICRON VT STM (variable temperature scanning tunneling microscope) is located in the analysis chamber to which the sample can easily be transferred. The main purpose of this UHV apparatus is the characterization of the

morphology of surfaces and the measurement of I(V)-curves by scanning tunneling spectroscopy (STS). To avoid vibrations of the system all mechanical pumps are switched off during STM or STS measurements. The measurements are entirely controlled by a personnel computer using the Scala Pro software package. The temperature of the sample during measurements can be adjusted between 25 and 1300 K. Heating is achieved by a Si solid-state or BN heating element and cooling is performed by helium or nitrogen flowing through a cryostat.

During STM measurements the sample is grounded and the tip is biased with a selectable voltage. For STS measurements the sample is also grounded, the voltage is sweeped over a specified range, and the current is recorded. Typical parameters for the STS measurements are summarized in Table 2.2. The acqui-

Range	-4...4 V
Step size	0.1 V
Acquisition time	2560 μs
Delay time	50 μs

Table 2.2: Typical parameters for STS measurements

sition time is the time for measuring at a single step. The delay time is the time that elapses between positioning of the tip and the start of the measurement of an I(V)-curve. These parameters are chosen independently of what kind of sample (metal, semiconductor, oxide) is measured, because for comparison of the measurements the same parameters have to be used.

A schematic of the STM is shown in Fig. 2.3.

2.3 The Solid State Evaporator

Deposition of material by evaporation belongs to the so-called physical vapor deposition (PVD) techniques. These include also the deposition by sputtering and ion plating. Evaporation was first used by M. Faraday in the 1850s, but is of importance only since the development of vacuum techniques. Technologically, evaporation is applied chiefly in optics, e.g., for the production of metallic mirrors or interference layers. For surface science the growth of films with high purity and controllable deposition rates is important.

For deposition by evaporation of a material in UHV the material must be heated, which is in this work achieved by electron bombardment. Electrons are generated by heating a filament, accelerated by a high voltage, and focused onto the evaporant. This leads to a local heating of the evaporant resulting in evaporation but not in complete melting of the target. Heating only a small spot of

the target also tends to keep the background pressure low. In the construction of an evaporator it is anticipated to have an ideal effusion cell (Knudsen cell), which is defined by the following assumptions:

- The liquid and vapor are in equilibrium in the cell.
- The mean free path of the evaporated particles inside the cell is much larger than the orifice diameter.
- The orifice diameter is much smaller than the distance to the receiving surface.

The vapor pressure p_v for a solid or liquid can be calculated from the Clausius-Clapeyrone equation

$$\frac{dp_v}{dT} = \frac{H}{T(V_v - V_{sl})}, \tag{2.1}$$

where H is the heat of vaporization, V_v the volume of one mole of vapor, and V_{sl} the volume of one mole of solid or liquid. For the assumptions that $V_{sl} \ll V_v$ and that for V_v hold the laws of ideal gases, i.e. $V_v = p_v/RT$, this equation can be integrated to give

$$p_v = A \cdot \exp\left(-\frac{B}{T}\right), \tag{2.2}$$

where A and B are constants. The exponential dependence of p_v on T indicates that a small change in temperature induces a large change in vapor pressure.

For practical use, tables of the dependence of the vapor pressure on the temperature are available [31]. However, it is more convenient to know the amount of material that is incident on the receiving surface (substrate) per area and time. For equilibrium, the flux F in $\mathrm{cm^{-2}s^{-1}}$ is given by [31]

$$F = \frac{ap(T)}{\pi L^2 \sqrt{(2mkT)}}, \tag{2.3}$$

where a is the area of the orifice of the cell in $\mathrm{cm^2}$, L the distance between orifice and substrate in cm, and m the atomic mass of the evaporant material. From equation (2.3) it can be calculated that for typical values of the geometry ($L = 5\,\mathrm{cm}$, $a = 0.5\,\mathrm{cm^2}$) and a deposition rate of $\sim 0.01\,\mathrm{ML/s}$ vapor pressures of $\sim 10^{-4}\,\mathrm{mbar}$ are necessary. For aluminum this means that a temperature of $\sim 1200\,\mathrm{K}$ is required [31] which is well above the melting point of Al (930 K).

For aluminum (as well as gallium) the evaporation from suitable compounds is convenient, because well defined stable beam fluxes are achieved. This is the case until all the Al (Ga) is exhausted, meaning that the deposition conditions are reproducible for a long time.

In this work a modified triple evaporator of the type Omicron EFM 3T was used. It contained a Co rod and two crucibles. One crucible was filled with a pestled crystal of NiAl for evaporation of Al, the other one was filled with a pestled crystal of CoGa for evaporation of Ga. The technical modifications and parameter settings were described by Jeliazova [32]. The EFM 3T is equipped with a flux monitor to detect the ion flux which is simultaneously generated by electron impact within the evaporator and directly proportional to the flow of the evaporated particles. The flux monitor operates independently of the shutter being open or closed. Thus the emission current (I_{EM}) and the acceleration voltage (HV) can be adjusted so that a certain flux appears. Hence, the evaporator can be calibrated with a quartz microbalance and thereafter for a defined ion flux the deposition rate is known.

Especially for small deposition rates (e.g. r = 0.48 Å/s for Al in this work) it is necessary to operate the evaporator at background pressures $\leq 5 \cdot 10^{-10}$ mbar. This is achieved for the Omicron EFM 3T by a water cooled copper cylinder that surrounds the evaporation cell.

The parameter settings used in this work are:

- for NiAl: $HV = 0.9\,\mathrm{kV}$, $I_{EM} = 30\,\mathrm{mA}$ resulting in $r = 0.48\,\text{Å} \pm 5\%$ Al/min
- for Co: $HV = 1\,\mathrm{kV}$, $I_{EM} = 15\,\mathrm{mA}$ resulting in $r = 0.8\,\text{Å} \pm 5\%$ Co/min

The thickness of the film calculated from the deposition rate is referred to as the nominal thickness. It will be explained in the next chapter that the thickness of the film can be determined from AES. The result of this determination will be referred to as the effective thickness.

In this chapter the UHV machines and its components, especially the evaporator were described. The next chapter deals with the physical processes that underly the measurement techniques.

Chapter 3

Basic Aspects of the Experimental Methods

3.1 Auger Electron Spectroscopy (AES)

3.1.1 The Auger Process

The Auger process was first observed by Pierre Auger in 1920 and is visualized in Fig. 3.1.

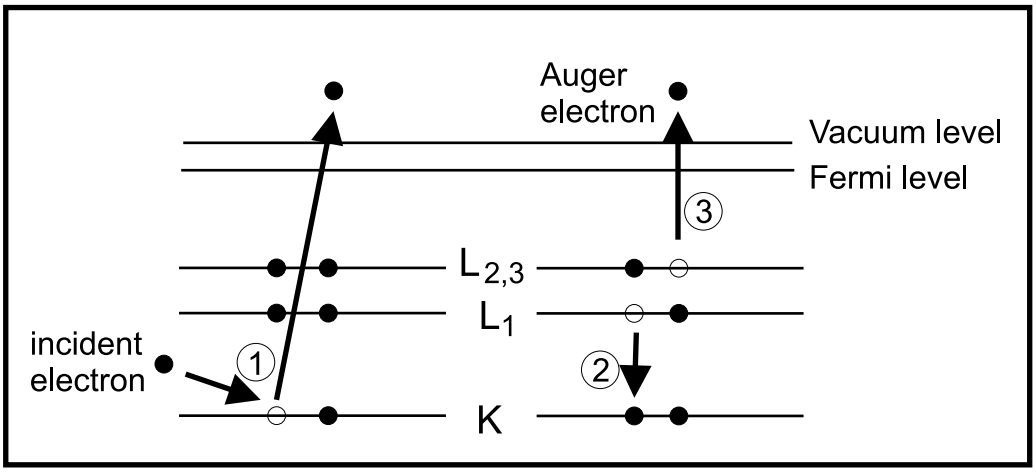

Figure 3.1: *Schematic representation of the Auger process.*

The Auger process proceeds via the following three steps:

1. An electron of one of the inner shells (here K-shell, with the binding energy E_K) is removed by an incident electron of typically $2-10\,\mathrm{keV}$

2. The vacancy is filled by an electron of a higher level (here L_1.)

3. The energy is transferred to an electron of the same level or a higher level (here $L_{2,3)}$. And this electron is emitted radiationlessly.

The kinetic energy of the emitted Auger electron is given by

$$E_{kin} = E_K - E_{L_1} - E_{L_{2,3}} - \Delta E, \tag{3.1}$$

where many-electron-effects are taken into account by the correction term ΔE. The transition is denoted according to the participating shells, e.g., in Fig. 3.1 a $KL_1L_{2,3}$-transition is shown.

E_{kin} depends merely on the element under consideration and thus the Auger process is an useful tool to identify the chemical composition of a material. In this work quantitative analyses of AES data are performed by comparison of peak-to-peak intensities of differentiated AES spectra as a function of layer thickness or by comparison of the ratio of peak-to-peak intensities of different elements. In this way the adsorption of an element on a surface and the desorption from the surface as well as the diffusion of an element into the bulk of the substrate is revealed. A determination of the chemical composition is also possible [33].

In the solid state the inner-shell levels remain almost unchanged compared to the free atom. Therefore, AES transitions allow identification of the chemical element. Since the outer-shell levels are strongly influenced by the chemical bonding, Auger transitions also probe the ionicity of the element.

	KLL	LMM	MNN
Al	1396	68	–
Al^{3+}	1378	35, 43, 51	–
Co	–	656, 716, 775	53
Ni	–	716, 783, 848	61, 102
O	483, 503	–	–

Table 3.1: Energies of the AES transitions that are regarded in this work .

Additionally, AES can be employed to estimate the thickness of a film grown on a substrate, if the substrate consists of materials different from the film. The emitted Auger electrons of the substrate must penetrate the film and, accordingly, the number of electrons that leave the system decreases with increasing thickness of the film. If the film grows layer by layer, the change in intensity dI is related to the change in thickness dx as

$$\frac{dI}{I} = -\frac{dx}{\lambda}, \tag{3.2}$$

where λ is the inelastic mean free path (IMFP) of the electrons of the specific Auger transition of the substrate in the material of the film. Integrating this equation results in:

$$I^S = I_0^S \cdot \exp\left(-\frac{d}{\lambda}\right), \tag{3.3}$$

where I_0^S is the intensity of the Auger signal of the substrate before deposition and I^S after deposition. Values of the mean free path λ for various elements and different energies can be taken from [34]. For some inorganic compounds values for different energies also exist [35].

3.1.2 The Auger Electron Spectrometer

The AES spectrometer used in UHV apparatus 1 is based on a cylindrical mirror analyzer (CMA). The CMA is shown schematically in Fig. 3.2.

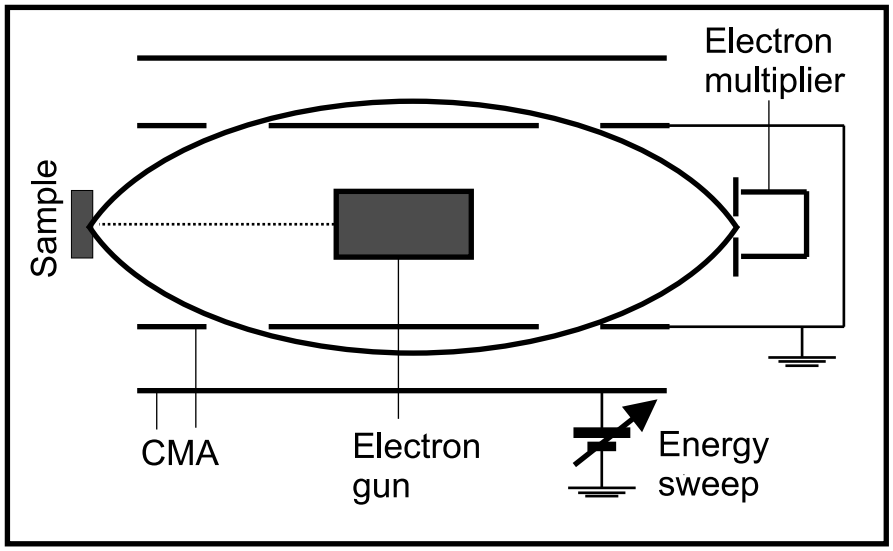

Figure 3.2: *Cylindrical mirror analyzer (CMA).*

The electron gun generates electrons of typically 3 keV and is located in the center of the CMA, so that the electron impact on the sample is perpendicular to its surface. It is operated at 1 mA emission current resulting in $\sim 2\,\mu$A sample current. As the voltage of the CMA is sweeped, the pass energy for the electrons changes and the N(E)-curve is measured. The step width is 1-2 eV and the acquisition time is adjusted between 20 and 50 ms. The spectra are recorded and numerically differentiated by a PC to suppress the background.

Since the electrons enter the CMA at an angle of 42° with respect to the surface normal, the estimation of the thickness from the Auger spectra must be

corrected by inserting the term $\cos(42°)$ in equation (3.3). For the particular spectrometer the equation

$$I^S = I_0^S \cdot \exp\left(-\frac{d}{\lambda \cos(42°)}\right), \tag{3.4}$$

is used.
The sensitivity of AES normally is not better than 1% of a monolayer [31].

3.2 Low Energy Electron Diffraction (LEED)

The diffraction of low energy electrons from an ordered surface was discovered by Davisson and Germer [36] in 1927. In the 1960s the technique of low energy electron diffraction (LEED) was developed [37]. In the following two subsections first the theory of LEED is briefly described, and then the LEED optics, which was used in this work, is introduced.

3.2.1 Theory of LEED

In 1924 L. de Broglie postulated the wave nature of electrons [38], where the wave length and momentum of electrons (and particles in general) are connected by the de Broglie relation: $\lambda = h/mv$, with h the Planck constant. Rewriting this equation gives $\lambda\,[\text{Å}] = \sqrt{150.4/E\,[\text{eV}]}$, and it follows that for electrons in the energy range from 10 to 500 eV the wavelength is between 3.88 and 0.55 Å, respectively, and hence comparable to atomic distances in solids.

The scattering of a plane wave at a periodic lattice in one dimension is shown in Fig. 3.3.

Constructive interference resulting in maxima in the scattered intensity takes place if the path difference of waves scattered from neighboring lattice points is a multiple of the wavelength λ. If the incident angle of the electrons is φ_0 constructive interference occurs at an angle φ with respect to the surface normal, if the condition

$$a(\sin\varphi - \sin\varphi_0) = n\lambda \tag{3.5}$$

is fulfilled. Two-dimensional lattices can be regarded as an ensemble of rows of scatterers with directions $[h'k']$ and mutual distances $d_{h'k'}$. In this case the condition for the interference maxima reads:

$$d_{h'k'}(\sin\varphi - \sin\varphi_0) = n\lambda\,. \tag{3.6}$$

In a LEED experiment an unknown surface structure with basis vectors $\vec{b}_1$ and $\vec{b}_2$ is superimposed on a known substrate lattice with basis vectors $\vec{a}_1$ and

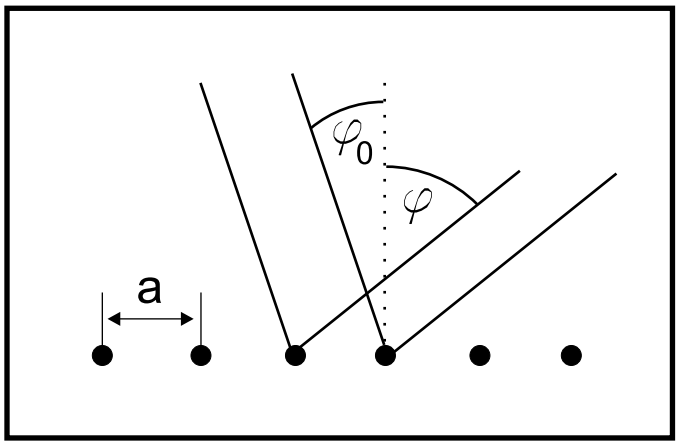

Figure 3.3: *Scattering of a plane wave at a periodic lattice.*

$\vec{a}_2$. These basis vectors are related by

$$\vec{b}_1 = m_{11}\vec{a}_1 + m_{12}\vec{a}_2 \tag{3.7}$$
$$\vec{b}_2 = m_{21}\vec{a}_1 + m_{22}\vec{a}_2. \tag{3.8}$$

In order to find the coefficients m_{ij} the concept of reciprocal space is applied. Reciprocal lattice vectors $\vec{a_1}^*$ and $\vec{a_2}^*$ are defined to obey

$$\vec{a}_i \cdot \vec{a_j}^* = \delta_{ij}, \qquad \delta_{ij} \text{ – the Kronecker symbol} \tag{3.9}$$

It follows immediately, that $\vec{a_1}^*$ is perpendicular to $\vec{a}_2$ and $\vec{a_2}^*$ is perpendicular to $\vec{a}_1$. For the lengths of the reciprocal lattice vectors it follows:

$$a_1^* = 1/(a_1 \sin\gamma) \tag{3.10}$$
$$a_2^* = 1/(a_2 \sin\gamma), \tag{3.11}$$

where the angle γ between $\vec{a_1}$ and $\vec{a_2}$ is related to the angle γ^* between $\vec{a_1}^*$ and $\vec{a_2}^*$ by

$$\gamma^* = \pi - \gamma \qquad \text{which means} \qquad \sin\gamma^* = \sin\gamma. \tag{3.12}$$

The vectors of the superimposed surface structure, $\vec{b}_1$ and $\vec{b}_2$, are analogously connected to the reciprocal lattice vectors $\vec{b}_1^*$ and $\vec{b_2}^*$, and these are correlated with $\vec{a_1}^*$ and $\vec{a_2}^*$ by

$$\vec{b_1}^* = m_{11}^*\vec{a_1}^* + m_{12}^*\vec{a_2}^* \tag{3.13}$$
$$\vec{b_2}^* = m_{21}^*\vec{a_1}^* + m_{22}^*\vec{a_2}^*. \tag{3.14}$$

The coefficients m^*_{ij} are correlated to the coefficients m_{ij} via

$$m_{11} = \frac{m^*_{22}}{m^*_{11} \cdot m^*_{22} - m^*_{12} \cdot m^*_{21}} \tag{3.15}$$

$$m_{12} = -\frac{m^*_{21}}{m^*_{11} \cdot m^*_{22} - m^*_{12} \cdot m^*_{21}} \tag{3.16}$$

$$m_{21} = -\frac{m^*_{12}}{m^*_{11} \cdot m^*_{22} - m^*_{12} \cdot m^*_{21}} \tag{3.17}$$

$$m_{22} = \frac{m^*_{11}}{m^*_{11} \cdot m^*_{22} - m^*_{12} \cdot m^*_{21}}. \tag{3.18}$$

In a LEED experiment the pattern of the substrate yields the reciprocal lattice vectors $\vec{a_1}^*$ and $\vec{a_2}^*$, while the pattern of the unknown structure yields $\vec{b}^*_1$ and $\vec{b_2}^*$. From these reciprocal lattice vectors the matrix elements m^*_{ij} can be calculated and by equations (3.15)-(3.18) the matrix elements in real space are obtained.

For the special case that the angle between the basis vectors of the substrate and the angle between the basis vectors of the superimposed structure are the same, another more convenient notation exists, which is called Wood notation, after E. Wood [39]. The scale factors m and n are defined as $m = |\vec{b_1}|/|\vec{a_1}|$ and $n = |\vec{b_2}|/|\vec{a_2}|$, and the surface structure is denoted $p(m \times n)\mathrm{R}\Theta$ for primitive unit cells and $c(m \times n)\mathrm{R}\Theta$ for centered unit cells, where R indicates a rotation of the surface unit cell with respect to the substrate unit cell and Θ specifies the angle. If $\Theta = 0^0$, then RΘ is left out and the structure is termed $c(m \times n)$ or $p(m \times n)$. For primitive unit cells even the p is sometimes left out.

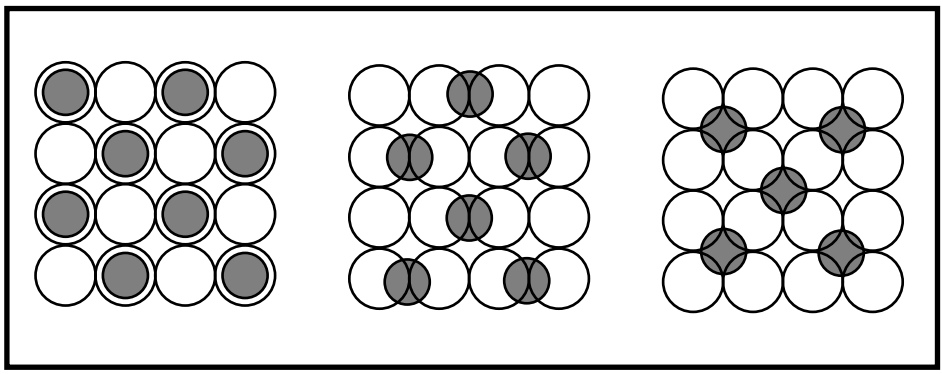

Figure 3.4: *Possible arrangements of a c(2 × 2)-structure.*

It is important to mention that LEED yields information only about the periodicity of the surface lattice and not about the atomic positions. If the LEED pattern of an adsorbate is identified as a c(2x2) structure in the Wood notation, there are three possible arrangements for the adsorbate atoms: on-top sites, bridge sites, and four-fold hollow sites. This is shown in Fig. 3.4.

In reality the periodicity of the lattices does not continue infinitely. This results in a finite half width h_d of the diffraction spots, which in turn can be used to estimate the mean diameter d of the periodic structures ("domain size"):

$$\frac{h_d}{a^*} \approx \frac{a}{d} \tag{3.19}$$

3.2.2 The Three Grid LEED Optics

The LEED apparatus used in the experiments here is schematically shown in Fig. 3.5. Electrons are emitted from the heated filament and collimated by the

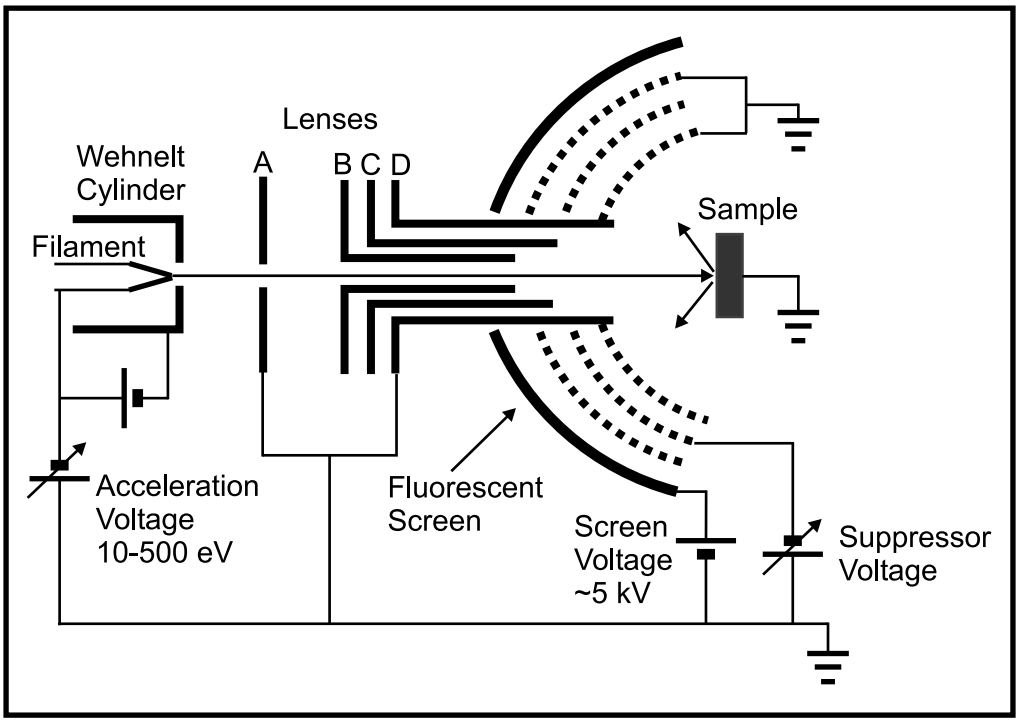

Figure 3.5: *Schematic of the three-grid LEED optics*

Wehnelt cylinder, which is biased slightly negative with respect to the filament. The electrons are then accelerated towards the grounded lens A. Lenses B and C focus the electron beam. Lens D and the grid in front of the sample are grounded in order to create a field free region between sample and grid. This prevents the electrons from being electrostatically deflected. The incident electrons are diffracted by the sample and drift towards and through the grid in front of the sample. The second grid is biased negative and its voltage is slightly smaller than the primary energy of the electrons. In this way inelastically scattered electrons from the first grid are repelled. The electrons are finally accelerated towards

the fluorescent screen by biasing the screen at $5-10\,\mathrm{kV}$. The grid in front of the screen is grounded.

The fluorescent screen is illuminated by the diffracted electrons resulting in a diffraction pattern and by inelastically scattered electrons resulting in a relatively homogeneous background. The image is recorded by a digital camera with rather long acquisition times (typically 15 s) to enhance the contrast between pattern and background. The visibility of the pattern is further enhanced by image processing.

3.3 Electron Energy Loss Spectrometry (EELS)

The fundamental idea of high resolution electron energy loss spectroscopy (EELS) is measuring the energy loss of electrons after being scattered (inelastically) from a surface. Prior to scattering, the electrons are monochromatic ($0.5-10\,\mathrm{meV}$ FWHM). Three different scattering mechanisms are relevant for EELS, which are briefly introduced. For this work the dipole scattering mechanism is the most important and its underlying theory (the so-called dielectric theory) is subsequently summarized. Afterwards the EEL spectrometer, which was used for this work (Ulti 100), is discussed.

3.3.1 Theoretical Background of EELS

The different scattering mechanisms

Dipole scattering means scattering of electrons from long-range oscillating electric fields. These fields originate from electric dipoles which are brought to vibration. Fig. 3.6 shows a dipole on a metallic substrate accompanied by its image dipole.

The components of the dipole moment parallel to the surface and its image dipole moment are of opposite sign and, consequently, they cancel. The components perpendicular to the surface add up and the effective dipole moment amounts to $2\,p_\perp$. This is the so-called dipole selection rule: Only those surface vibrations can be observed which have a component of the dipole moment perpendicular to the surface. In the framework of group theory the selection rule reads: Only those vibrations are observed in dipole scattering, that belong to the totally symmetric representations A_1, A' and A of the point group.

The scattering takes place at a distance of $\sim 100\,\text{Å}$ above the surface. Thus the change in wave vector is small, resulting in a distribution of the scattered electrons which is centered around the specular direction as shown in Fig. 3.7.

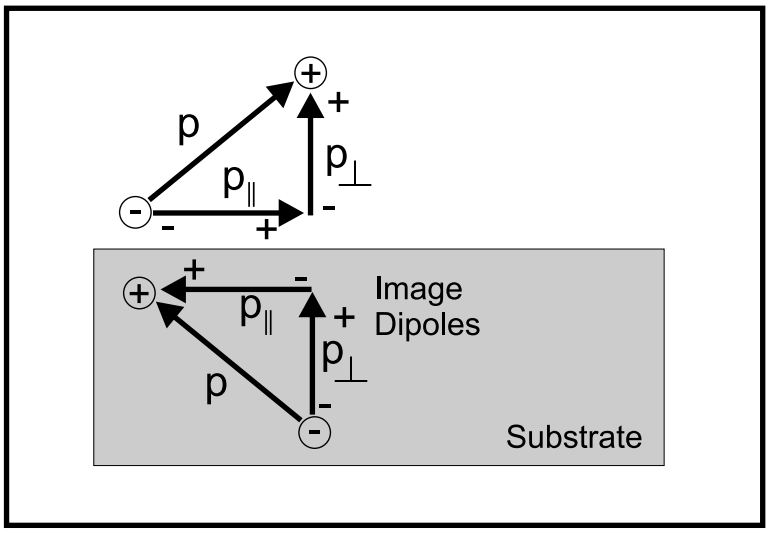

Figure 3.6: *Dipoles and image dipoles on a metallic substrate.*

Impact Scattering is electron scattering from the (atom cores) of the lattice. The interaction is short-ranged and the change in wave vector and energy is much larger than for dipole scattering. Impact scattering results in a broad angular distribution of inelastically scattered electrons as indicated in Fig. 3.7.

In investigations of the dispersion of surface phonons impact scattering is the relevant mechanism. However, the cross section of phonon creation depends strongly on the energy of the primary electrons and the scattering angle.

Negative Ion Resonance means the capturing of an electron of a certain energy. This results in a short-lived (10^{-10} to 10^{-15} sec) negatively charged ion. This process is dominant for molecules in the gas phase, but is also observed for molecules that are weakly bound on the surface. Upon decay of the negative ion, the electrons will adopt an angular distribution according to the symmetry of the excited level.

The Dielectric Theory

Several different approaches exist to treat the interaction of an electron with electric dipole fields of excitations at surfaces:

1. The Hamiltonian of the free electron is considered, and the dipole field of the excitation is treated as a perturbation of this Hamiltonian.

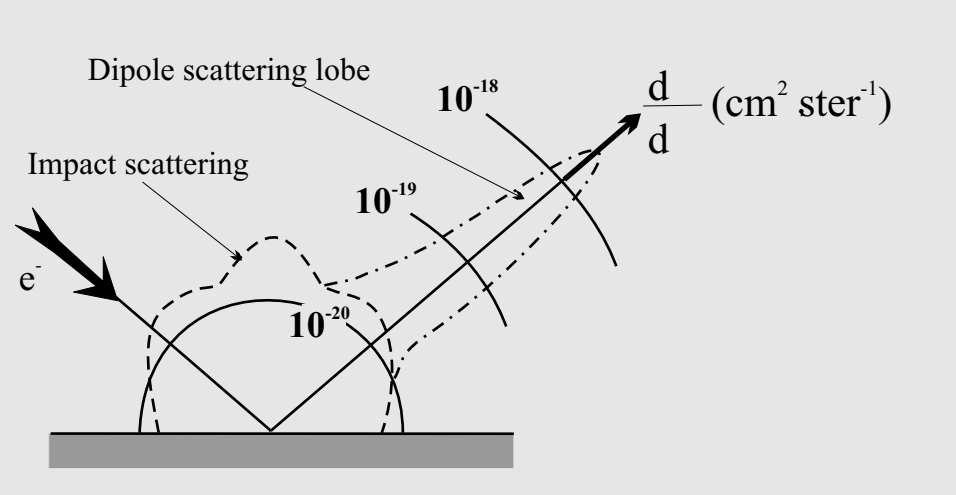

Figure 3.7: *The different cross-sections of dipole and impact scattering.*

2. The Hamiltonian of the excitation is considered while the electron is treated as a perturbation.

3. The solid is described by a local or nonlocal dielectric function. This is the so-called dielectric theory, which is independent of the specific excitation. The disadvantage is that the quantum mechanical properties of the excitation must be introduced *ad hoc*. This approach is summarized in the following.

The electric field of an electron passing a surface causes dielectric displacements in the solid, which results in a reduction of the kinetic energy of the electron. In the Fourier transformed mode the energy loss per unit volume can be written as [40, 31]

$$\mathrm{Re}\left[2\pi i \int_{-\infty}^{\infty} \omega E(\omega) D^*(\omega) d\omega\right], \tag{3.20}$$

where E is the electric field and D the dielectric displacement.

The classical scattering probability $P_{cl}(\vec{q}_{\|}, \hbar\omega)$ for an incident electron and a surface excitation with the wave vector $\vec{q}_{\|}$ and energy $\hbar\omega$ is given by

$$P_{cl}(\vec{q}_{\|}, \hbar\omega) \propto \int_D \frac{q v_{\perp}^2}{[(\vec{q}_{\|} \cdot \vec{v}_{\|} - \omega)^2 + (q v_{\perp})^2]^2} \,\mathrm{Im}\left[-\frac{1}{\epsilon(\omega)+1}\right] d\vec{q}_{\|}. \tag{3.21}$$

The integration is performed over all wave vectors being scattered into the acceptance angle of the analyzer, in accordance with energy and momentum conservation. The scattering probability consists of two terms: the kinematic prefactor

and the energy loss function Im $\left[-\frac{1}{\epsilon(\omega)+1}\right]$. The kinematic prefactor has a sharp maximum when the so-called "surfing condition" is matched:

$$v_{\parallel} = \frac{\omega}{q_{\parallel}} \tag{3.22}$$

For grazing incidence ($v_{\perp} \ll v_{\parallel}$) this condition results in a concentration of the electrons around the specular direction. Due to the change of the wave vector the maximum is shifted to smaller angles.

The classical differential scattering cross section $d^2S/(d(\hbar\omega)d\Omega)$, which describes the scattering of electrons with the energy $\hbar\omega$ into a solid angle $d\Omega$, is proportional to the classical scattering probability. The quantum mechanical properties of the excitation are introduced by treating the excitation as a Bose-particle. Mathematically this is achieved by multiplying the classical differential scattering cross section by

$$1 + \left[\exp\left(\frac{\hbar\omega}{k_B T}\right) - 1\right]^{-1}$$

3.3.2 The EEL Spectrometer

The development of different types of EEL spectrometers is in detail described in [41]. The spectrometer employed in this work is of the type Ulti 100, a photograph of which is shown in Fig. 3.8.

Electrons are emitted thermally by heating a LaB_6 cathode via a tungsten filament. Lenses A_1–A_3 focus the electron beam on to the entrance slit of the premonochromator. The premonochromator as well as the following monochromator are based on 127° cylindrical capacitors. They are made of copper and coated with a graphite layer. The scattering chamber is equipped with lenses B_1 and B_2 at the entrance side and lenses B_3 and B_4 at the outlet side. The scattered electrons that have suffered an energy loss are accelerated to the pass energy of the analyzer. This is achieved by appropriately biasing all the potentials on the analyzer side. The analyzer is a one-stage analyzer, and after passing this the electrons are detected by a channeltron which is operated in the counting mode.

The manipulation of all the potentials of the various components of the spectrometer is done by a personal computer and analog-digital converters. The channeltron signal is simultaneously recorded by an XY-plotter and a PC which allows further analysis of the data.

Two operation modes have been used for this work:

1. **Measuring surface vibrational modes:** The loss features range from 5 to 500 meV. The primary energy is typically 3 – 5 eV, the scans are taken

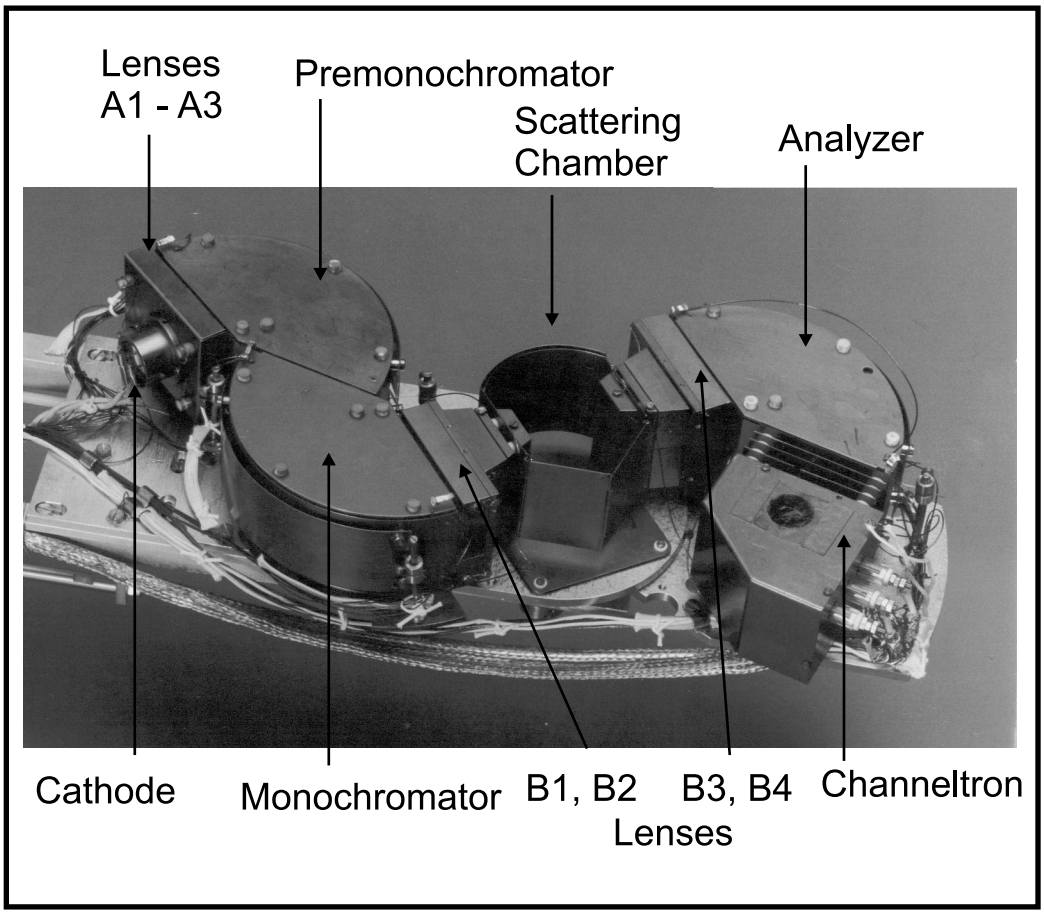

Figure 3.8: *Photograph of the EEL spectrometer Ulti100.*

within -1000 to +2000 cm^{-1}, with a step width of $3-5\,cm^{-1}$. The acquisition time is 1 to 4 sec per step. Although the Ulti 100 allows, in principle, a resolution of less than 1 meV, the spectra in this mode show a resolution of $6-10$ meV, which results from not perfectly ordered surfaces.

2. **Measuring electronic transitions:** The loss features range from 0.5 to 10 eV. The primary energy had to be increased to $15-30$ eV in order to excite transitions in the range of $0.5-10$ eV. The intensity was increased accepting a reduction in resolution, which was typically 30 meV. The scanned energy range is $0-10$ eV with a step width of $50-100\,cm^{-1}$ and acquisition times per step of $5-20$ sec.

3.4 Scanning Tunneling Microscopy (STM)

3.4.1 Fundamentals of Scanning Tunneling Microscopy and Spectroscopy

Scanning Tunneling Microscopy (STM) was invented in 1982 by Binnig and Rohrer [42, 43]. It is based on the wave-like nature of electrons that can undergo a quantum mechanical tunneling process. This was first described by Fowler and Nordheim [44]. For tunneling between two planar metallic electrodes with a vacuum barrier the tunnel current is given by:

$$I \propto \exp(-A\sqrt{\phi}d), \tag{3.23}$$

where A is a constant, d the distance between the electrodes, and ϕ the average work function.

If one electrode is an STM tip, the tunneling current can be written as

$$I_T \propto \frac{U}{d} \exp(-A\sqrt{\phi}d), \tag{3.24}$$

where $A = 1.025\,\text{Å}^{-1}\text{eV}^{-1/2}$. For d (in the range of Å) the current is of the order of nA which can be easily measured. If d changes by $\sim 1\,$Å, the tunneling current changes by about one order of magnitude. Therefore d has to be controlled with a precision of $0.05-0.1\,$Å. To achieve a lateral resolution that allows imaging of individual atoms, the movement of the tip across the surface under investigation must be controlled to within $1-2\,$Å [31].

Two kinds of measurements have been performed with the STM in this work. The classical scanning tunneling microscopy, which yields structural information of the surface, and the so-called scanning tunneling spectroscopy (STS), which is basically a measurement of an I(V)-curve and yields information about the electronic properties of the surface. These methods are described in the following.

Scanning Tunneling Microscopy (STM)

In this work the STM was operated in the *constant current mode*. This means that a voltage between tip and sample and a current are selected and kept fixed. The distance between tip and sample is then adjusted, so that equation (3.24) is fulfilled. The adjustment of the distance between tip and sample (z-direction) as well as the lateral motion (x-, y- direction) of the tip is achieved by applying appropriate voltages to Piezo-elements. If the tip is biased negatively with respect to the sample, tunneling takes place from filled states of the tip into empty states of the sample. If the tip is biased positively with respect to the sample, tunneling

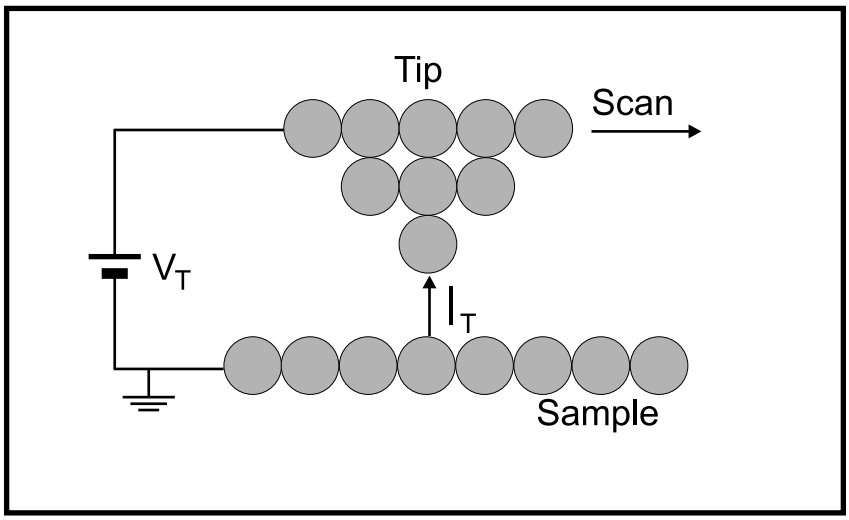

Figure 3.9: *Schematic of the tunneling process in STM*

takes place from filled states of the sample into empty states of the tip. The later situation is depicted in Fig. 3.9.

The tip is scanned over the surface and the distance d is converted to a grayscale image. The information contained in this image is strictly a map of the local electronic density of states (LDOS). However, since the LDOS is usually closely related to the atomic positions, the image can be interpreted as the crystal structure of the surface in real space. According to Tersoff and Hamann, who developed a theory of STM [45, 46], the lateral resolution of STM is given by $[(2\text{Å})(R+d)]^{1/2}$, where R is the tip radius and d the distance between tip and sample.

The above considerations apply strictly only for conducting substrates. If the sample is non-conducting as in the case of an oxide layer on top of a metallic substrate, tunneling may proceed into the substrate or into the oxide film depending on the bias voltage.

In Fig. 3.10(a) the bias voltage is smaller than $E_g/2$ (where E_g is the band gap of the oxide) and tunneling proceeds into the conduction band (CB) of the substrate. In this case the oxide only changes the potential barrier and STM is sensitive to the topography at the interface of substrate and oxide film [47].

If the bias voltage exceeds $E_g/2$ as shown in Fig. 3.10(b), tunneling takes place into the conduction band of the oxide. In this case the STM image contains information about the topography of the oxide [47]. These two situations were demonstrated by Bertrams et al. [48] for a thin alumina film on NiAl(110).

A third operation mode at low bias voltage is also possible. If the tip comes very close to the surface, so that repulsive forces between tip and surface become

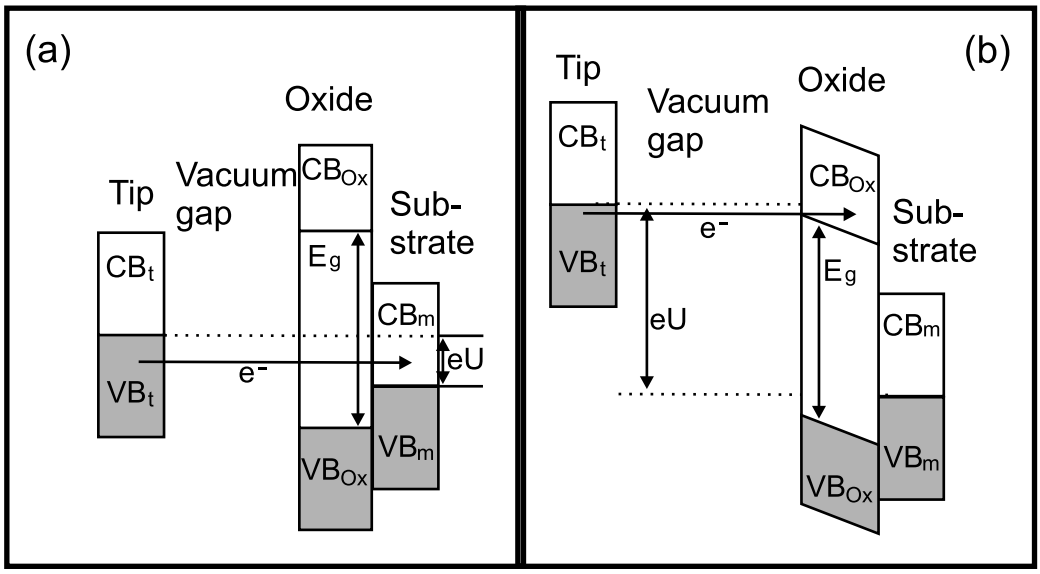

Figure 3.10: *Band structure of the tunneling process into the oxide covered metallic substrate (a) and tunneling into the oxide (b) depending on the tip voltage.*

important for the imaging process, the topography of the oxide film is probed rather than the interface [47, 49].

Scanning Tunneling Spectroscopy (STS)

In order to probe the local electronic properties of the sample, a special point on the surface is selected and an I(V)-curve is measured. To achieve this the tip is placed at the selected point meeting the specified tunneling conditions (i.e. the distance d between tip and sample is adjusted to obtain the values of U and I). The voltage applied to the Piezo-element that adjusts d is then kept constant. In this way the voltage sweep is performed with a fixed distance between tip and sample. Voltage and current are recorded electronically.

It is not straightforward to extract information from these I(V)-curves, because the curves depend on the setpoint (U, I) of the STM measurement. In other words, the setpoint must always be one point of the I(V)-curve and thus the curve does not represent purely properties of the sample. However a normalization of the curve can be performed [51, 52] by plotting $d(\log I)/d(\log V)$ vs. V. This tends to eliminate the dependence of the tip sample separation.

Assuming that in

$$\frac{dI/dV}{I/V} = \frac{d(\log I)}{d(\log V)} = \frac{\rho_s(eV)\rho_t(0) + A(V)}{B(V)}, \tag{3.25}$$

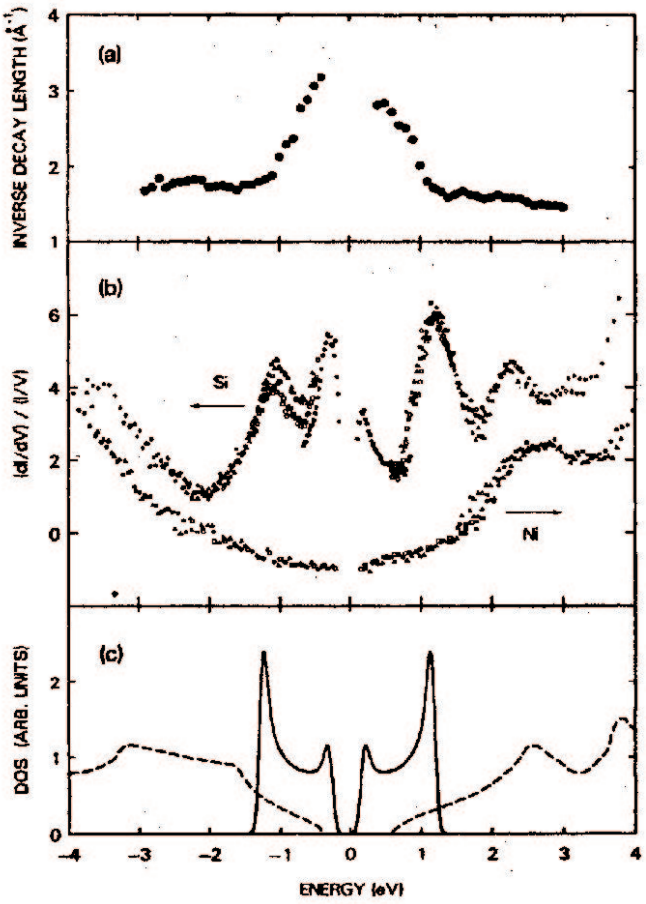

Figure 3.11: *Normalized I(V)-curve of Si(111)2×1, reproduced from ref. [50].*

where ρ_s and ρ_t are the DOS of the sample and tip, respectively, A(V) and B(V) are functions that vary only slowly with voltage, a structure in $(dI/dV)/(I/V)$ reflects $\rho_s(eV)$. This normalization yields reasonable agreement concerning the position of peaks in the DOS but not concerning the intensity [53].

Fig. 3.11(a) shows the inverse decay length of the tunneling current for the Si(111)2x1 surface. It was obtained by measuring the tunnel current as a function of the tip sample separation and fitting exponential curves to the experimental results. An example of the normalization procedure is shown in Fig. 3.11(b) for the Si(111)2x1 surface [50]. For comparison the normalized I(V)-curve of Ni is also shown. Fig. 3.11(c) shows the theoretical DOS for the bulk valence band and conduction band of silicon (dashed line) and the DOS from a one-dimensional tight-binding model of the π-bonded chains (solid line). The later model exhibits maxima in the DOS at the same energies as the measurement in Fig. 3.11(b). The approximate independence of the results from the tip-sample separation for

the Si(111)2x1 surface was demonstrated by Stroscio et al. [54].

Chapter 4

Survey of the Investigated Materials

4.1 Metals

4.1.1 Nickel

Nickel was discovered by Axel Frederik Cronstedt in 1751 in Sweden. At this time it was of value for coloring glass green. Nowadays nickel is chiefly valuable for the alloys it forms, such as stainless steel and other corrosion-resistant alloys.

Nickel is a hard, ductile metal, which has the face centered cubic (fcc) crystal structure with a lattice constant of $a_{Ni} = 3.52\,\text{Å}$. The (100) surface of Ni (or a fcc crystal in general) is shown schematically in Fig. 4.1.

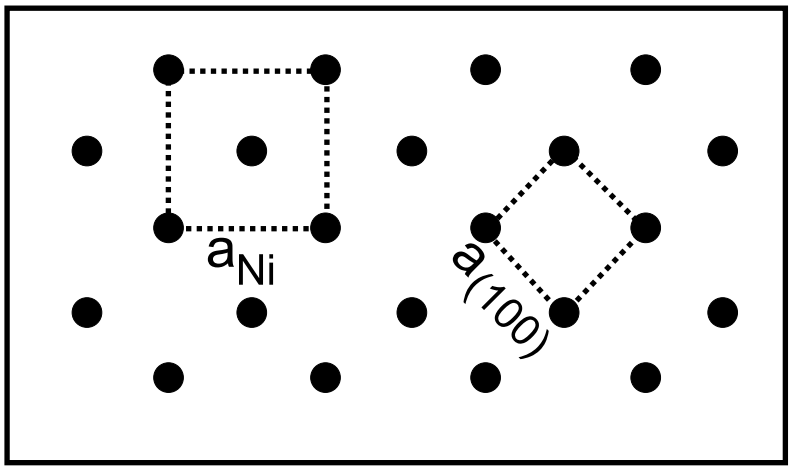

Figure 4.1: *Schematic representation of the (100) surface of Ni showing the lattice constant of Ni and the lattice constant* $a_{(100)}$ *of the two-dimensional unit cell.*

In contrast to bcc crystals the smallest periodic structure of the (100) surface does not correspond to the lattice constant. The two-dimensional lattice constant is defined in Fig. 4.1 and is given by $a_{(100)} = 1/\sqrt{2} \cdot a_{Ni} = 2.48\,\text{Å}$ for Ni. The Bragg spots in the LEED pattern of the Ni(100) surface correspond to the two-dimensional unit cell.

The melting point of nickel is $T_m = 1726\,\text{K}$. Nickel is ferromagnetic and has a Curie-temperature of $T_c = 645\,\text{K}$.

4.1.2 Cobalt

Minerals containing cobalt were used by early civilizations of Egypt and Mesopotamia for coloring glass blue. It was announced to be an element by Georg Brandt about 1739. Today it is used e.g. in alloys with iron, nickel, and other metals, which are used in jet engines and gas turbine engines. It is also a component in magnet steels and stainless steels. The artificial isotope ^{60}Co is an important γ-ray source.

Cobalt exists in two different crystal structures: Below 700 K it shows the hexagonally close packed structure (ϵCo) with lattice constants of $a_{hcp} = 2.51$Å and $b_{hcp} = 4.07$Å. Above 700 K it changes to the fcc crystal structure (αCo) with a lattice constant of $a_{fcc} = 3.54$Å. The melting point of cobalt is $T_m = 1765\,\text{K}$. As nickel, cobalt is ferromagnetic with a Curie-Temperature of $T_c = 1404\,\text{K}$.

4.2 Intermetallic Compounds

4.2.1 Ni–Al

Five ordered intermetallic alloys of Ni and Al are known: Ni_3Al, Ni_5Al_3, NiAl, Ni_2Al_3, and $NiAl_3$. The phase diagram of the Ni–Al system is shown in Fig. 4.2 and the crystal structure data are presented in Table 4.1.

Alloy	Atom % Al	Space group	Prototype
(Ni)	0 to 21.2	Fm3m	Cu
Ni_3Al	24 to 27	Pm3m	Cu_3Au
Ni_5Al_3	∼32 to 36	Cmmm	Pt_5Ga_3
NiAl	30.8 to 58	Pm3m	CsCl (bcc)
Ni_2Al_3	59.5 to 63.2	$P\bar{3}m1$	Ni_2Al_3
$NiAl_3$	75	Pnma	Fe_3C
(Al)	99.89 to 100	Fm3m	Cu

Table 4.1: Crystal structure data of the Ni–Al system from ref. [55]

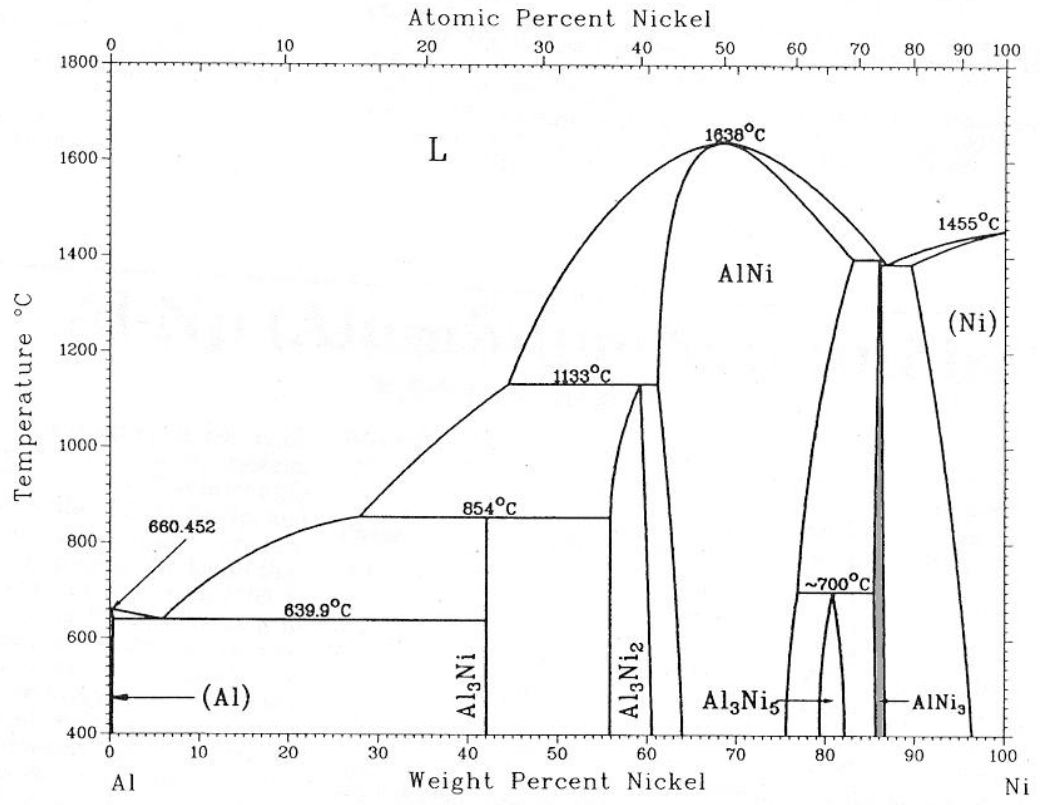

Figure 4.2: *Phase diagram of the Ni–Al system, from ref. [55]*

For this work Ni_3Al is of particular relevance since it is formed when Al is deposited on a Ni single crystal and then annealed [56, 57]. The lattice constant of Ni_3Al is 3.565Å and is thus close to that of Ni (3.52Å). The crystal structure is cubic and contains four atoms per unit cell. The Al atoms occupy the cube corners, while the Ni atoms are located in the face centers. Two terminations of the (100) surface of Ni_3Al are possible: For the first one, the first layer contains 50% Ni and 50%Al, and for the other one the first layer consists of 100% Ni. Ni_3Al is a ferromagnet with a Curie temperature of $T_c = 70\,K$ [58].

4.2.2 Co–Al

The ordered bulk alloys of cobalt and aluminum that are definitely known are presented in Table 4.2. The phase Co_3Al seems not to exist. For the lattice constants of Co_2Al_5 Elliot [61] gives slightly different values: a = 7.66 Å and c = 7.59 Å.

The solubility of cobalt in aluminum and aluminum in the hexagonally close

Alloy	Space Group	a, b, c [Å] / β	Reference
Co_2Al_9	monoclinic	a=8.56, b = 6.29 c=6.21, β=94.76°	[59]
Co_2Al_5	hexagonal	a=7.67, c=7.61 c/a=0.99	[59]
CoAl	bcc CsCl-type	a=2.86	[59]
Co_4Al_{13}	monoclinic Cm	a=15.18, b=8.12 c=12.34, β=107.9°	[60]

Table 4.2: Crystal structure data of the Co–Al system from ref. [55]

packed phase ϵCo is almost zero [59]. This is reflected in the phase diagram (Fig. 4.3) by the very narrow regions of Al and ϵCo. The solubility in the fcc phase (αCo) increases with temperature.

The heats of formation are given by Ageev [62] as 110.9 kJ/mol for CoAl, 161.7 kJ/mol for Co_2Al_9, and 294.0 kJ/mol for Co_2Al_5.

4.3 Oxides

4.3.1 Alumina

Al_2O_3 is known to have at least 14 different phases. Due to this large number of phases and their complex structure, Al_2O_3 has been studied extensively. In 1798, Greville reported about a mineral with the composition Al_2O_3, which was called "corundum" [63]. The name corundum is still used for α-Al_2O_3, the most stable phase of alumina.

Natural deposits are the aluminum hydroxides, among which a distinction is made between the trihydroxides $Al_2O_3 \cdot 3H_2O$ (e.g, Hydrargillite, Bayerite, Nordstrandite) and aluminumoxide-hydroxides (e.g. Diaspore, Boehmite)[64]. During the decomposition of these hydroxides numerous phases occur, which differ in crystal structure and lattice constant. The following decomposition sequences are found:

1. Oxide-Hydroxide
   - Diaspore $\xrightarrow{450°}$ α-Al_2O_3
   - Boehmite $\xrightarrow{450°}$ γ $\xrightarrow{600°}$ δ $\xrightarrow{1000°}$ θ $\xrightarrow{1200°}$ α-Al_2O_3

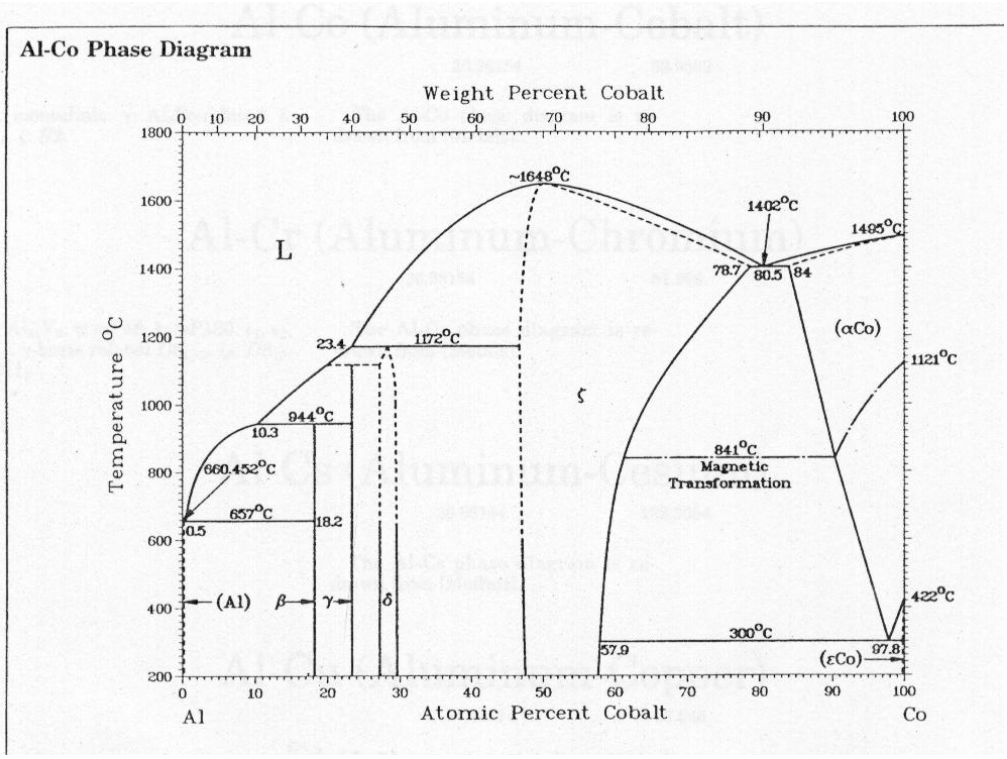

Figure 4.3: *Phase diagram of the Co–Al system from ref. [55]*

2. Trihydroxide

   - Hydrargillite $\xrightarrow{250^\circ}$ χ $\xrightarrow{900^\circ}$ κ $\xrightarrow{1200^\circ}$ α-Al_2O_3
     Hydrargillite $\xrightarrow[\text{dry atmosphere}]{180^\circ}$ Boehmite $\longrightarrow \ldots$
   - Bayerit $\xrightarrow{250^\circ}$ η $\xrightarrow{850^\circ}$ θ $\xrightarrow{1200^\circ}$ α-Al_2O_3
     Bayerit $\xrightarrow[\text{dry atmosphere}]{180^\circ}$ Boehmite $\longrightarrow \ldots$
   - In high vacuum:
     $\left[\begin{array}{c}\text{Nordstrandite}\\ \text{Bayerite}\\ \text{Hydrargillite}\end{array}\right]$ $\xrightarrow{400^\circ}$ γ $\xrightarrow{750^\circ}$ θ $\xrightarrow{1200^\circ}$ α-Al_2O_3

Two series of transformations, where dehydration is not involved, are:

- α-Al_2O_3 + Ion-implantation $\longrightarrow$ am-Al_2O_3 $\xrightarrow{950^\circ}$ γ-Al_2O_3 [65]
- Al $\xrightarrow{O_2}$ am-Al_2O_3 $\xrightarrow{900^\circ}$ γ-Al_2O_3 [66]

The properties of some phases of alumina are compiled in Table 4.3.

Oxide	Space Group	a,b,c [Å] β	Oxygen sublattice	Occupied interstices	Remarks
α-Al_2O_3	hexagonal D^6_{3d}	a=4,7589 c=12,991	hcp	octahedral	Corundum
β-Al_2O_3	hexagonal	a=5,60 c=22,50		octahedral+ tetrahedral	
γ-Al_2O_3	cubic O^7_h	a=7,911	fcc	octahedral+ tetrahedral	Spinel-Type
γ'-Al_2O_3	cubic	a=3,95		octahedral+ tetrahedral	
δ-Al_2O_3	tetragonal	a=7,96 c=11,70	fcc	octahedral+ tetrahedral	distorted Spinel-Typ
κ-Al_2O_3	hexagonal	a=9,71 c=17,86		octahedral+ tetrahedral	
θ-Al_2O_3	monoclinic C^3_{2h}	a=2,92 b=5,64 c=11,83 β=103°	fcc	octahedral+ tetrahedral	isomorphic with β-Ga_2O_3

Table 4.3: Crystal structures of some alumina phases

All phases of alumina are based on a close packed oxygen lattice (fcc or hcp). Within this oxygen lattice, the Al^{3+}-ions occupy sites with different symmetry (octahedral or tetrahedral). According to the stacking of the oxygen layers three groups of phases can be distinguished:

- ABAB...-group: The oxygen ions build a hexagonal close package. α-Al_2O_3 belongs to this group and the Al^{3+}-ions occupy exclusively sites with octahedral symmetry.
- ABCABC...-group: The oxygen ions build a face centered cubic crystal lattice and the Al^{3+}-ions occupy tetrahedrally as well as octahedrally coordinated sites. The phases (e.g. γ-Al_2O_3, γ'-Al_2O_3, θAl_2O_3) differ in the occupation probabilities of the two kinds of sites.
- ABAC...-group: In this group are all phases, which have neither a hexagonal nor a cubic stacking (e.g. β-Al_2O_3).

Two phases of alumina are discussed briefly. First, γ-Al_2O_3 belongs to the ABCABC...-group. The O^{2-}-ions form a fcc lattice, and the Al^{3+}-ions occupy octahedral and tetrahedral sites with a ratio between 5:3 and 3:1. It has a defect

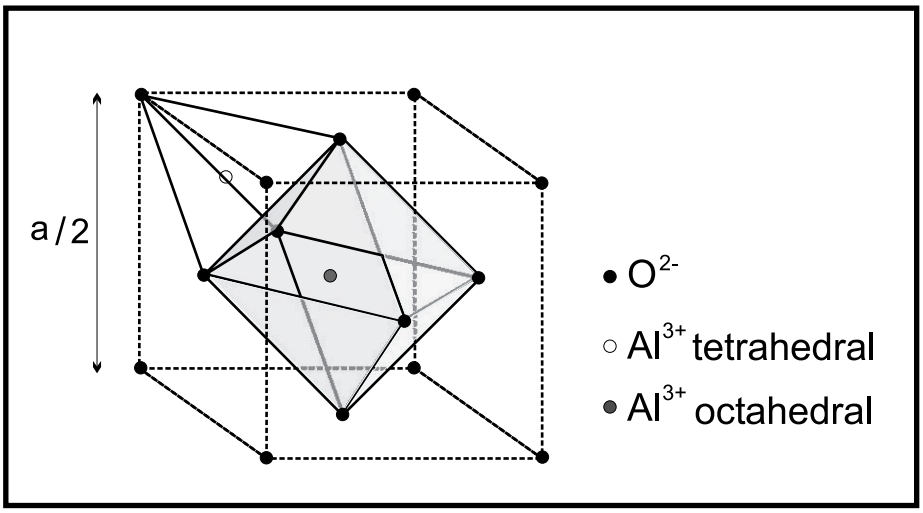

Figure 4.4: *Simplified defect spinel structure*

spinel structure, a simplified model of which is shown in Fig. 4.4. γ'-Al_2O_3 has also a defect spinel structure, but only half the unit cell of γ-Al_2O_3.

Amorphous Al_2O_3, which develops upon the oxidation of bulk aluminum, consists of a locally close packed oxygen matrix, where the Al^{3+}-ions occupy exclusively tetrahedrally coordinated sites. Since the Al^{3+}- and O^{2-}-ions display a local order, amorphous Al_2O_3 is also called vitreous.

The different phases of alumina exhibit different losses in EEL spectra (IR-active modes). These losses are assembled in Table 4.4 including references and temperatures.

4.3.2 Gallium Oxide

Ga_2O_3 is of interest due to its applications as a gas sensor at high temperatures [69] and as a tunneling barrier in magnetic tunnel junctions [70]. Since the structural characterization is not a topic of this work, only a short description is given. As Al_2O_3 also Ga_2O_3 exists in different phases, which are isomorphic to a corresponding phase of Al_2O_3.

The most important phase is β-Ga_2O_3, which is the most stable phase and isomorphic to θ-Al_2O_3 with a = 3.04 Å, b = 5.80 Å, c = 12.23 Å, and $\beta = 103.7°$ [71, 72]. α-Ga_2O_3 is isomorphic to α-Al_2O_3 with a = 4.98 Å and c = 13.43 Å and transforms into β-Ga_2O_3 upon annealing to 650°C. γ- and δ-Ga_2O_3 are isomorphic to γ- and δ-Al_2O_3, respectively.

The preparation of β-Ga_2O_3 on CoGa(100) has been investigated by Gassmann [23]. It is prepared by oxidation of the CoGa(100) surface at room temperature

	Ref.	Frequencies of the losses [cm^{-1}]				T [K]
a-Al_2O_3 / Ni_3Al(111)	[14]		629		810	300
a-Al_2O_3 / Ni_3Al(100)	[11]		635		850	300
γ'-Al_2O_3 / Ni_3Al(111)	[14]	440	648		910	1000
γ'-Al_2O_3 / Ni_3Al(100)	[11]	415	640		875	1100
α-Al_2O_3 / NiAl(100)	[8]			638	913	$>$ 1300
α-Al_2O_3 / NiAl(111)	[10]			630	911	$>$ 1100
bulk α-Al_2O_3 (0001)	[67]	500			800	
Al_2O_3 / Re(0001)	[18]		609		863	970
Al_2O_3 / Re(0001)	[18]	360	616		880	1170
Al_2O_3 / Ru(0001)	[68]	360	678		899	1173
Al_2O_3 / Mo(110)	[19]				790	110
Al_2O_3 Mo(110)	[19]		610		845	700
Al_2O_3 / Mo(110)	[19]	435	655		895	1100
Al_2O_3 / Al(111)	[15]			$\sim$695	$\sim$870	300

Table 4.4: Characteristic frequencies of Al_2O_3 on various substrates

and subsequent annealing to 550 K. Oxidation of the CoGa(100) surface at this temperature also leads to the formation of β-Ga_2O_3. It is characterized by a (2x1) LEED pattern and four characteristic loss features in the EEL spectra. The band gap of a film prepared in this way is 4.4 eV , but there are also metal induced states in the band gap [23].

β-Ga_2O_3 can also be prepared by oxidation of CoGa(100) at higher temperatures, e.g. [25]. The oxidation of the CoGa(100) surface at various temperatures was investigated by several authors: Schmitz et al. [25, 73], Eumann et al. [24], Franchy et al. [26], and Pan et al. [27, 28, 29].

Chapter 5

The Growth of Al_2O_3 on Ni(100)

In this chapter the growth of alumina films on the Ni(100) surface is presented. It is on the one hand well known that ordered Al_2O_3 films can be grown on Ni_3Al surfaces [11, 13]. On the other hand a thin Ni_3Al layer can be grown on Ni(100) [56, 57]. In my PhD work these results were combined to prepare a well ordered Al_2O_3 film by growth and oxidation of a Ni_3Al alloy on Ni(100)

Intermetallic alloys in general are interesting because of their physical and mechanical properties, like high melting point, low density, and good corrosion resistance. A review of some possible applications, e.g., in areas of energy storage and furnace hardware, has been presented by Stoloff et al. [74]. Thin films of metals and intermetallics are intensively studied, because the low dimensionality leads to some interesting properties that differ from the properties of bulk metals and intermetallics.

By deposition of one monolayer of Al on the Ni(100) surface and subsequent annealing at 820 K Lu et al. [56] and O'Connor et al. [57] prepared thin films of Ni_3Al. The surface structure of the Ni_3Al/Ni(100) system was studied by LEED [56, 57] and ion scattering [57]. The thin film of Ni_3Al grows with the (100) plane parallel to the (100) surface of Ni(100). A Ni_3Al(100)/Ni(100) system can also be prepared by deposition of Al on Ni(100) at 520 K.

Ultrathin metal oxide films are utilized in different fields of application as catalysis [75, 76] and microelectronics [77, 78]. In general, the controlled epitaxial growth of ultrathin oxide layers (Al_2O_3, Ga_2O_3) on ferromagnetic substrates with a well defined ferromagnet/insulator interface is of crucial importance for the understanding of spin-dependent tunneling [5, 79, 80]. Therefore, many attempts are carried out to find procedures to prepare well defined homogeneous oxide layers with a thickness in the range of few tenths of an Å. Recently, tunnel magneto resistance ratios of 40% at room temperature have been achieved.

The growth of ultrathin alumina films on metal and metal alloy surfaces has been reviewed recently by Franchy [81]. In general, the oxidation of the surface

of the intermetallic alloys of NiAl leads to the formation of a thin Al_2O_3 film on the surface [8, 9, 10, 12, 13, 82, 83]. For most studies in UHV no evidence for the oxidation of Ni was found [13, 9, 84]. Thin films of Al_2O_3 were prepared on $Ni_3Al(111)$ [13, 14], $Ni_3Al(100)$ [12, 11], NiAl(111) [10], NiAl(110) [9, 48], and NiAl(100) [8, 85, 86]. On these substrates ordering of the Al_2O_3 film takes place in the temperature range 700–1200 K. Other intermetallic alloys containing 3d metals were also used to grow thin Al_2O_3 films, e.g., CoAl [87] or FeAl [88].

The preparation of thin Al_2O_3 films was also studied on metal substrates like Ru(0001) [17, 16], Re(0001) [18], Mo(110) [19], Ta(110) [20], Fe(110)[21], and Cu(111) [22]. The preparation mostly proceeds in two steps: A thin Al layer is deposited on the substrate and the Al film is then oxidized. For this procedure the problem arises, whether the Al film is completely oxidized. Therefore, different ways to oxidize thin Al films have been tested: the natural oxidation, where the Al film is exposed to oxygen [89], the UV oxidation, where the film is illuminated with ultraviolet (UV) light during the exposure to oxygen [90], and the plasma oxidation [91].

Compared to bulk Al_2O_3 samples thin films of Al_2O_3 have the advantage that electron spectroscopic methods can be applied without generating charging of the film. Various techniques were used to study thin Al_2O_3 films:

- AES: [8, 92, 93, 94]
- EELS: [15, 95, 8, 10, 96, 14, 97, 98]
- LEED: [9, 13, 8, 10, 99, 18, 14, 85, 100, 101]
- XPS: [13, 18, 99, 94, 102]
- LEIS: [18]
- TEM: [103]
- STM: [96, 85, 86, 104, 105, 93]

The Ni(100) single crystal that was used in this work has a diameter of 8 mm and a thickness of 2.5 mm. The crystal was cut by spark erosion and the surface was mechanically polished. The orientation has an accuracy of 0.5°. Cleaning of Ni(100) in UHV was achieved by repeated cycles of sputtering with Ar^+ ions at 1 keV and a sample current of 0.8 μA and annealing to 1200 K for five minutes. Carbon was removed by oxidation with oxygen at 1000 K and subsequent annealing to 1200 K. The clean Ni(100) surface exhibits a sharp (1x1) LEED pattern and no transitions of contaminants by AES.

The chapter is organized as follows: In section 5.1 the growth of a thin Ni_3Al layer on Ni(100) is discussed, in section 5.2 the oxidation of the Ni_3Al/Ni(100)

system at room temperature is presented, and section 5.3 deals with the oxidation of the system Ni_3Al/Ni(100) at 800 K. In section 5.4 the deposition of an Al film and the oxidation of the Al/Ni(100) system is shown, while in section 5.5 the deposition of an Al film on Ni(100) in oxygen atmospheres of different partial pressures is discussed. Section 5.5 concludes these chapters with a brief summary.

5.1 Growth of Ni_3Al(100) on Ni(100)

To grow an alloy of aluminum and nickel on the Ni(100) surface, first Al was deposited on the Ni(100) surface by evaporation from a pestled crystal of NiAl.

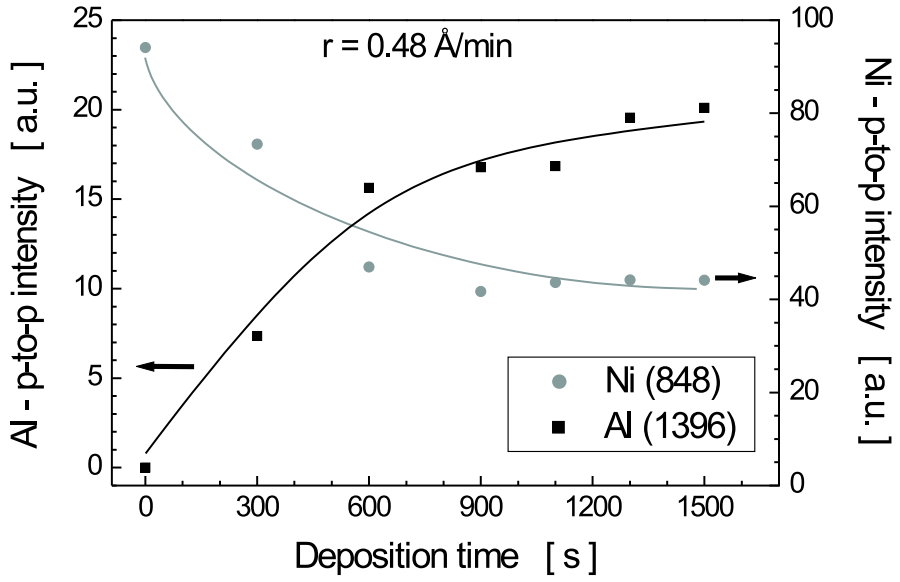

Figure 5.1: *Peak-to-peak intensity of the AES transitions of Al at 1396 eV and Ni at 848 eV as a function of the deposition time.*

Fig. 5.1 shows the peak-to-peak intensities of the KLL transition of aluminum at 1396 eV and the LMM transition of nickel at 848 eV as a function of the deposition time. The Al signal increases with deposition time but saturation is not reached here. The nominal thickness of the generated Al film can be calculated from the deposition rate and deposition time and is 12 Å. Saturation of the Al signal should be reached when the film thickness exceeds the mean free path of the 1396 eV-Auger-electrons in Al, which is 24 Å [34]. The exact shape of this curve depends on the growth mode of Al on Ni(100). The growth mode

cannot be determined by the methods used here, and thus the line in Fig. 5.1 represents only an approximate curve.

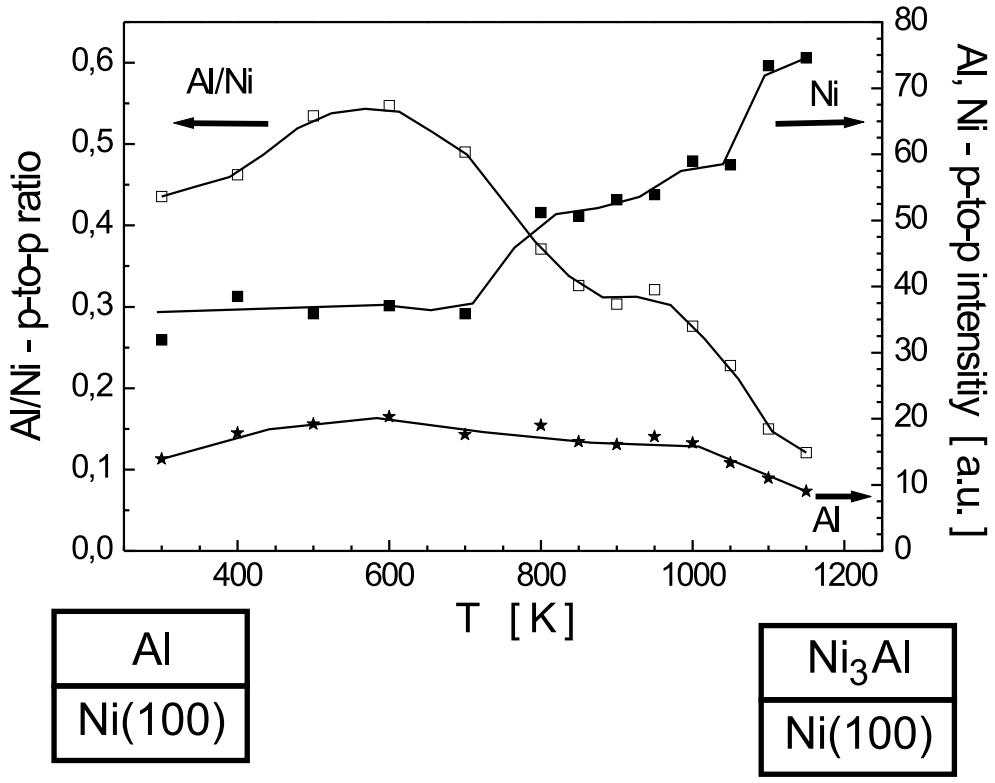

Figure 5.2: *Peak-to-peak intensity of the AES transitions of Al at 1396 eV and Ni at 848 eV as a function of the annealing temperature (right side scale). Also shown is the peak-to-peak ratio* Al_{1396}/Ni_{848} *(left side scale).*

The system Al/Ni(100) is then annealed beginning at room temperature up to 1200 K in steps of 50 K. Each annealing step lasted two minutes, and the sample was cooled to room temperature before the AES spectrum was measured. In Fig. 5.2, as in Fig. 5.1, the peak-to-peak intensities of Ni_{848} and Al_{1396}, together with the ratio Al_{1396}/Ni_{848}, are shown as a function of the annealing temperature. Up to 700 K the peak-to-peak intensity of Ni does not change significantly, whereas above 700 K the signal increases. The intensity of Al and, consequently, the ratio Al/Ni increase up to 700 K probably due to structural changes and ordering. Above 700 K, the ratio Al/Ni decreases in consequence of the increase of the Ni signal. This indicates that above 700 K interdiffusion (alloying) of Ni and Al takes place.

This is supported by the Auger spectra shown in Fig. 5.3. Spectrum (a) is

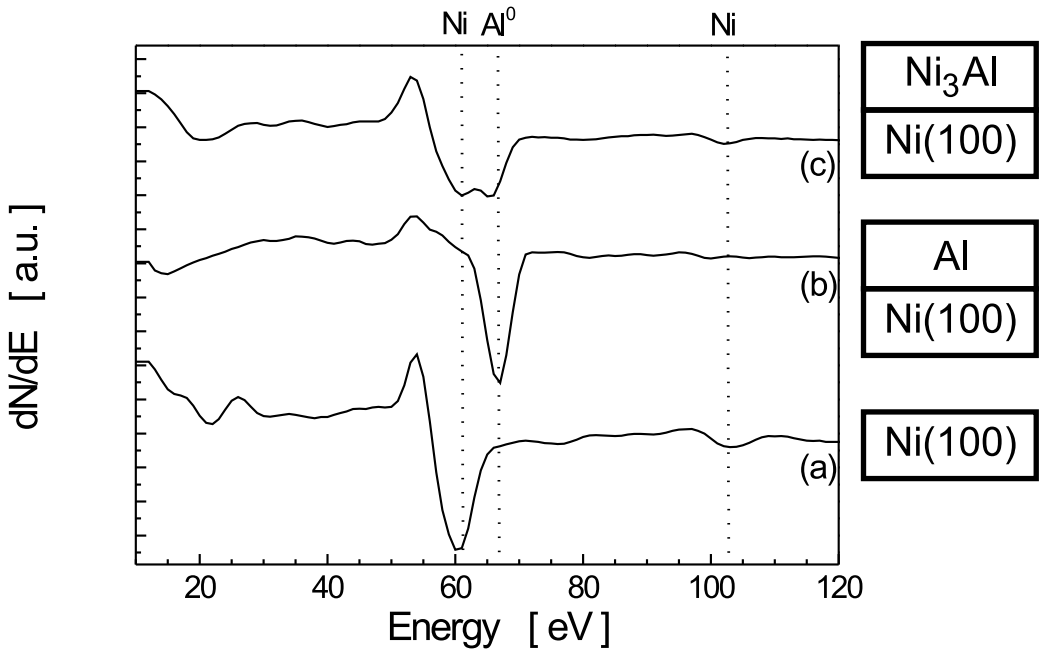

Figure 5.3: *AES spectra of clean Ni(100) (a), after deposition of 12 Å Al (b), and after annealing to 1150 K (c).*

taken from the clean Ni(100) surface and, accordingly, the MNN transitions of Ni at 61 and 102 eV are observed. Since the mean free path of electrons in metals is very small in this energy range ($\lambda_{Al}(50\,eV) = 3.2$ Å, $\lambda_{Al}(100\,eV) = 4.2$ Å, $\lambda_{Ni}(50\,eV) = 4.9$ Å, $\lambda_{Ni}(100\,eV) = 4.6$ Å [34]), the conclusions drawn from these parts of the spectra hold for the topmost layers. Spectrum (b) shows the situation after deposition of 12 Å of Al and only the LMM transition of Al at 68 eV is observed. There appears to be no nickel in the topmost layers within the sensitivity of AES. After annealing to 1150 K (Spectrum (c)) the transitions of Ni (61 and 102 eV) and of Al (68 eV) are observed indicating that both nickel and aluminum are in the topmost layers.

So far, only the chemical composition of the topmost layers was discussed. The structure of the surface was probed by LEED. The LEED pattern, that was obtained after annealing the Al/Ni(100) system to 1150 K, is presented in Fig. 5.4 (b). With respect to the clean Ni(100) surface (a) it exhibits a c(2x2) structure. This is in agreement with the findings of Lu et al. [56], who have prepared a Ni_3Al alloy on Ni(100) by deposition of one monolayer of Al and subsequent annealing to 820 K for five minutes. Later O'Connor et al. [57] investigated a

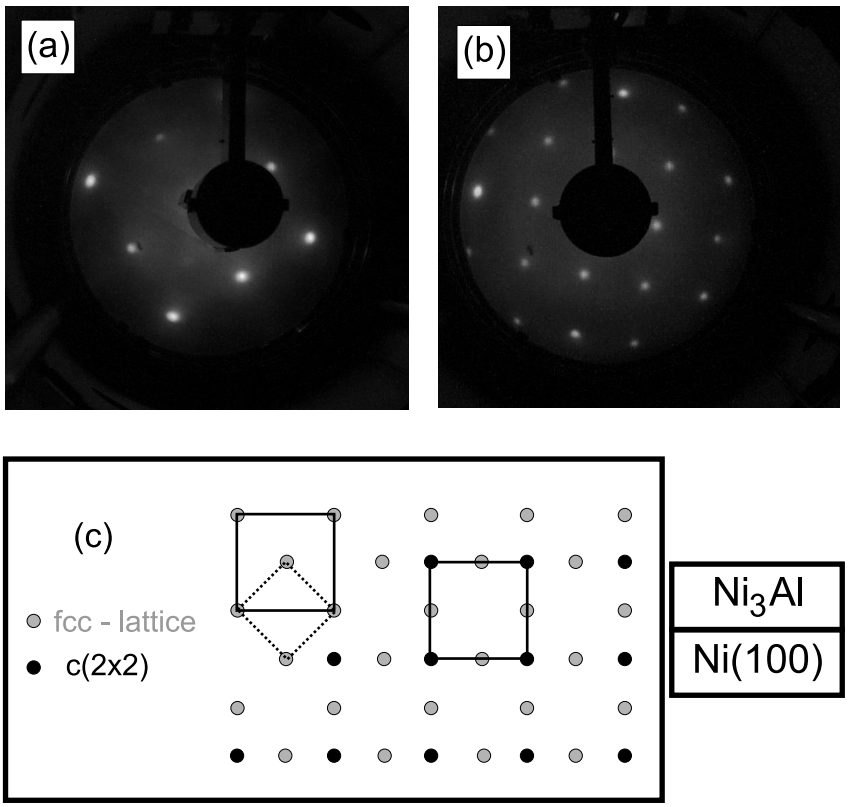

Figure 5.4: *LEED images of (a) the clean Ni(100) surface and (b) the Ni_3Al layer. The primary energy was 122 eV for both of the images. A schematic arrangement of the atoms forming the c(2×2) structure is shown in (c). Gray circles indicate the two dimensional lattice of the Ni(100) surface, black circles represent the Al atoms, that are incorporated into the Ni(100) surface.*

thin film of Ni_3Al prepared on Ni(100) by low energy ion scattering (LEIS) and medium energy ion scattering (MEIS). The film was prepared by deposition of one monolayer of Al on Ni(100) and annealing to 820 K. The LEIS and MEIS results show, that the Al is incorporated into the first layer, but does not form an overlayer. The Al content in the first layer was shown to be 50%, while the second layer contained little or no Al.

The two-dimensional lattice constant of the surface structure can be determined from the LEED pattern. Fig. 5.4(c) shows a schematic arrangement of the atoms that form the c(2x2) structure. The two-dimensional lattice of the Ni(100) surface is indicated by gray circles. The two-dimensional lattice constant of the Ni(100) surface is indicated by the solid lines combining the four atoms in the upper left corner of the schematic. However, the two-dimensional unit cell that corresponds to the LEED pattern of Fig. 5.4(a) is the one indicated by the dashed

lines in Fig. 5.4(c). A schematic arrangement of the atoms that form the c(2x2) structure in Fig. 5.4(b) is indicated by the black circles in Fig. 5.4(c). The two-dimensional unit cell of this structure is indicated by the solid lines combining the black circles. Thus, the two-dimensional lattice constant is the same as that of bulk Ni, i.e. (3.52 ± 0.1) Å. This is very close to the lattice constant of Ni_3Al (3.565 Å) and the difference may stem from a distortion of the Ni_3Al lattice.

The thickness of the film cannot be determined strictly with AES and equation (3.4), because the Ni_3Al film contains Ni, and thus the AES signal of Ni from the Ni_3Al layer contributes to the transitions of the Ni substrate. However, an upper limit can be given from the total amount of deposited Al and the lattice constant of Ni_3Al. Assuming that the 12 Å of Al are completely used to form Ni_3Al, then the thickness amounts to 35 Å. Although this determination is afflicted with a considerable error, it is likely that aluminum is situated in deeper layers than the first one (confirmed by [57]), and thus an ultrathin surface alloy in the strict sense is not formed.

In summary, in this section the formation of Ni_3Al/Ni(100) was investigated. Deposition and annealing above 700 K of a 12 Å thick Al film on a Ni(100) substrate leads to interdiffusion and alloying of Al and Ni. The LEED pattern of the Ni_3Al alloy exhibits a c(2x2) structure with respect to the Ni(100) substrate, and the two-dimensional lattice constant of the quadratic unit cell is (3.52 ± 0.1) Å.

5.2 Oxidation of $Ni_3Al(100)/Ni(100)$ at 300 K

In this section the oxidation of $Ni_3Al(100)/Ni(100)$ and annealing of the oxide that forms is discussed. The oxidation was studied at room temperature. Fig. 5.5 shows the peak-to-peak ratios of O_{503}/Ni_{848} and O_{503}/Al_{1396} taken from AES spectra.

Both ratios increase strongly up to an oxygen exposure of 200 L and above 500 L both ratios clearly reach their saturation level. The saturation value of the O/Al ratio (≈ 6.5) is approximately the one that is expected for bulk Al_2O_3 [33]. According to Cabrera and Mott [106] the growth rate for a metal oxide at low temperature is given by

$$\frac{1}{x} = A - B \ln t, \tag{5.1}$$

where x is the film thickness, t the time and A and B are constants. The curves in Fig. 5.5 represent fits with equation (5.1).

Information about the chemical composition of the surface can be gained from the Auger spectrum itself. The spectrum in the energy range $10-120$ eV taken after oxidation is shown in Fig. 5.6(a), and only the transitions at 51, 43, and 35 eV, which are characteristic for Al^{3+}, are observed [33]. This spectrum is com-

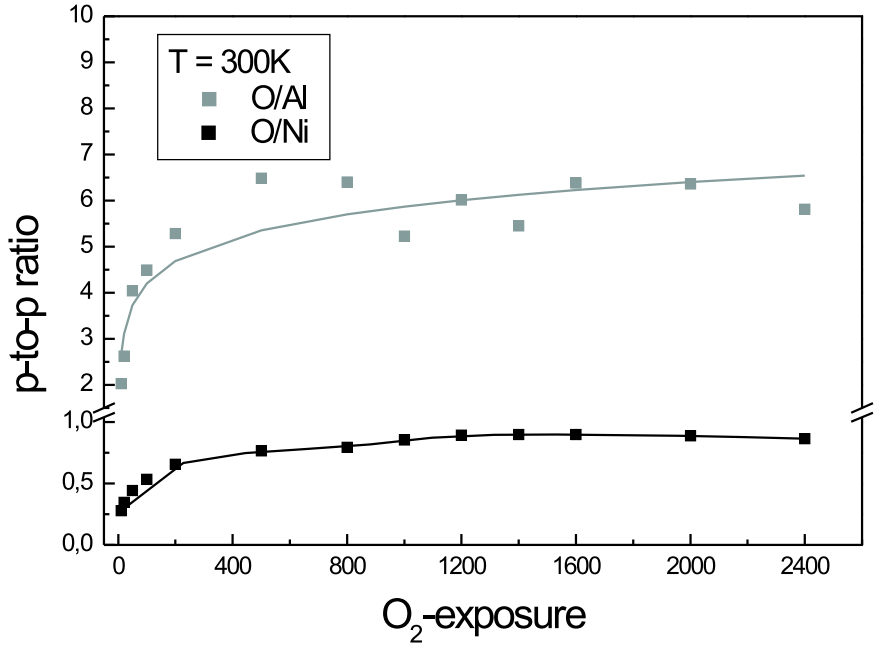

Figure 5.5: *Oxygen uptake curve for the $Ni_3Al(100)/Ni(100)$ system at room temperature. The analyzed transitions are: oxygen 503 eV, nickel 848 eV, and aluminum 1396 eV.*

pletely different from spectrum (c) of Fig. 5.3, where only transitions of metallic Al and Ni are observed. This proves the oxidation of aluminum. However, it is important to determine, whether Ni is also involved in the oxidation process. In an UPS study of the oxidation of NiAl [9], Ni_3Al [13], and FeAl [88] it was found that only Al atoms are oxidized. This suggests that in our case the same situation occurs.

Generally, the oxidation of aluminum is thermodynamically favored over the oxidation of nickel, because the heat of formation of Al_2O_3 is much larger than that of NiO ($\Delta H_f(Al_2O_3) = -1676\,\mathrm{kJ/mol}$, $\Delta H_f(NiO) = -240\,\mathrm{kJ/mol}$). The oxidation of exclusively one species of an intermetallic alloy is the so-called preferential segregation oxidation and can be described as follows: adsorption of oxygen atoms induces the segregation of Al atoms to the surface, where by reaction with the adsorbed oxygen an aluminum oxide film is formed. This process occurs frequently when intermetallic alloys of aluminum or gallium are concerned [81]. In principle, it is also possible that oxygen diffuses into the alloy. Then, however, a mixed oxide Ni, Al and O should form which could in turn be identified by AES

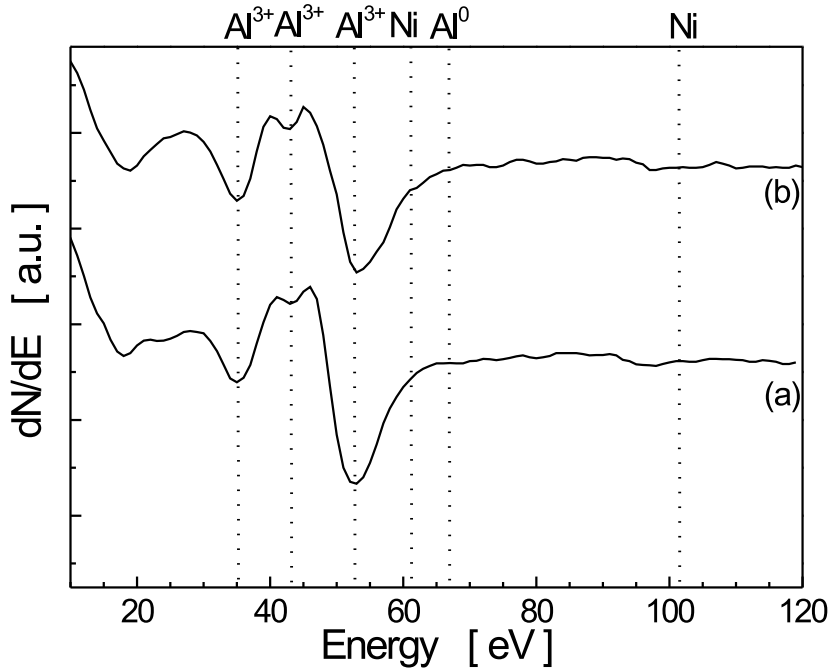

Figure 5.6: *AES spectra of the system Ni_3Al/Ni(100) after oxidation at room temperature (a) and after annealing of the oxidized system to 1200 K (b).*

and EELS.

Spectrum (b) in Fig. 5.6 is taken after annealing of the oxide film to 1200 K. The only difference compared to Spectrum (a) is the broader line width of the transition at 51 eV. This may originate from a decomposition and desorption of the alumina film resulting in overlapping of the Al^{3+} transition with the transition of metallic nickel at 61 eV. In Fig. 5.6 spectrum (a), taken after oxidation at room temperature, and spectrum (b), taken after annealing to 1200 K, are similar, which suggests that the ionicity of the aluminum does not change during annealing.

An estimate of the thickness of the oxide film can be given from AES data. Assuming that a pure Al_2O_3 film is grown on the Ni(100) substrate, the thickness of the film can be determined from the exponential decrease of the intensity of the AES transition of Ni at 848 eV. The relevant formula is equation (3.4), it was introduced in Chapter 3. The inelastic mean free path of electrons with energy 848 eV in Al_2O_3 is 18 Å [35]. The thickness of the Al_2O_3 layer amounts to $d = (11 \pm 2)$ Å, where the error has been estimated from the background in

the Auger spectra and the uncertainty of the mean free path. The thickness of an Al layer is known to increase upon oxidation. For example Chen et al. [107] observed that the thickness of an aluminum oxide film is nearly the double of that of the aluminum film. In our case probably some aluminum diffuses into the bulk of the nickel substrate during the formation of the Ni_3Al alloy, and thus the film thickness is less than $2 \cdot 12\,\text{Å} = 24\,\text{Å}$.

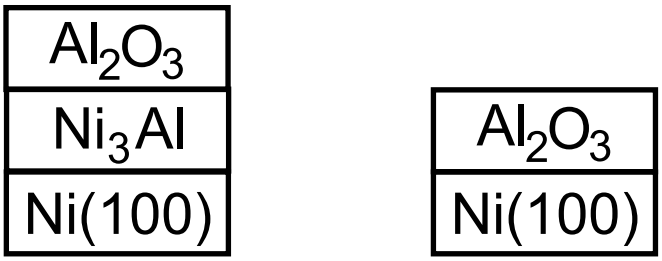

Figure 5.7: *Schematics of the possible layer composition.*

In principle, it should be possible to trace the oxidation of aluminum by the KLL AES-transition of metallic Al at 1396 eV and the transition of ionic aluminum (Al^{3+} at 1378 eV) [33]. However, these two transitions were not resolved separately, and only a broadening of the transition is observed during oxidation due to a coexistence of Al^0 and Al^{3+}. On the other hand, there is no hint of Al^0 in spectrum (a) of Fig. 5.6, and it is thus likely, that no neutral Al atoms are in the topmost 5 Å of the film. It cannot be determined if the unoxidized Al is within the film or in an interface layer between the Al_2O_3 and the Ni(100) substrate. Schematics of the possible layer structure are shown in Fig. 5.7, which suggest the presence of an interface layer between the oxide layer and the substrate.

The vibrational properties of the Al_2O_3 film were investigated by EELS. EEL spectra were recorded for each annealing step after the sample was cooled to room temperature. EEL spectra obtained after oxidation to saturation at room temperature (300 K) and after annealing to 1000 K and 1200 K are shown in Fig. 5.8. The spectrum taken after the oxidation (bottom) shows three broad losses at 420, 620, and 860 cm^{-1}. For an amorphous Al_2O_3 film only two dipole active modes are characteristic [81], because the Al^{3+} ions occupy exclusively tetrahedrally coordinated sites [108, 109]. In the present case, where already at room temperature three losses are observed, both tetrahedrally and octahedrally coordinated sites of the O^{2-} sublattice are occupied by the Al^{3+} ions. This means that the alumina film grown at room temperature does not only consist of an amorphous phase but rather of a mixture of different Al_2O_3 phases. This is supported by the information obtained from LEED. The LEED image after the oxidation is diffuse due to a lack of long-range order.

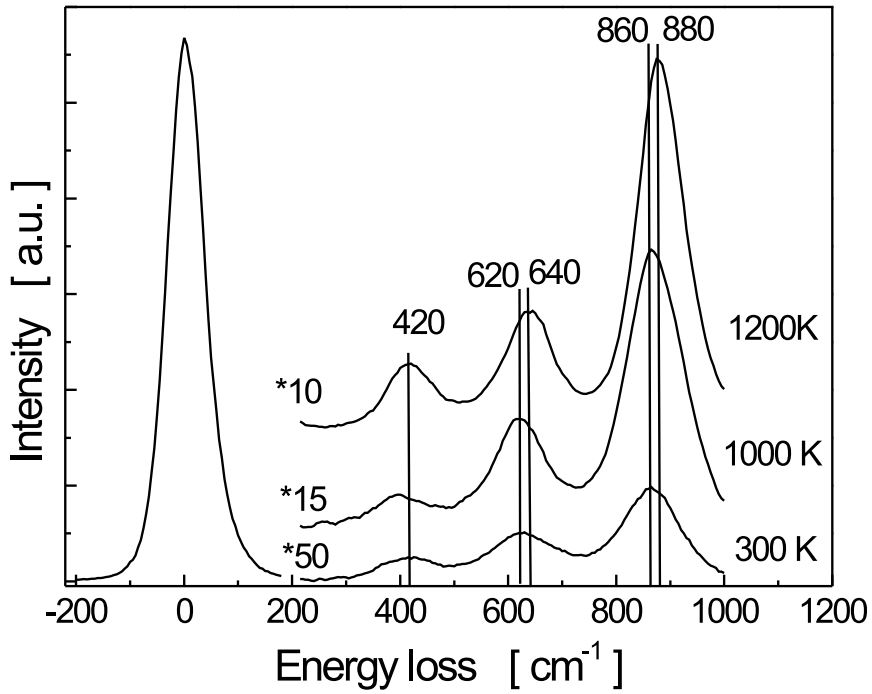

Figure 5.8: *EEL spectra taken after oxidation at room temperature and after annealing to 1000 and 1200 K. After annealing to 1200 K the losses at 620 and 860 cm^{-1} are shifted to 640 and 880 cm^{-1}, respectively. The spectra were recorded at room temperature.*

Between room temperature and 700 K the EEL spectra do not change significantly. At temperatures above 800 K the intensity of the losses and of the elastic beam increases. This is seen in Fig. 5.8 by the decrease of the magnification factor from 50 at 300 K to 10 at 1200 K. In the spectra taken after annealing to 1000 and 1200 K the loss at 420 cm^{-1} is at the same position as in the room temperature spectrum, whereas the other two losses are shifted to slightly higher frequencies (640 and 880 cm^{-1}). Generally, EEL spectra of well-ordered alumina films (γ-, γ'- and θ-Al_2O_3) on metal and metal alloy surfaces commonly show three (sometimes four) distinct phonon losses in the frequency regions 380 – 430, 620 – 660, and 850 – 890 cm^{-1} (see Table 4.4 in chapter 4 as well as Ref. [81] and references therein). Therefore, it can be concluded that the aluminum oxide that has formed upon annealing belongs to an ordered Al_2O_3 phase.

The increase of ordering is also reflected in the emergence of Bragg reflections

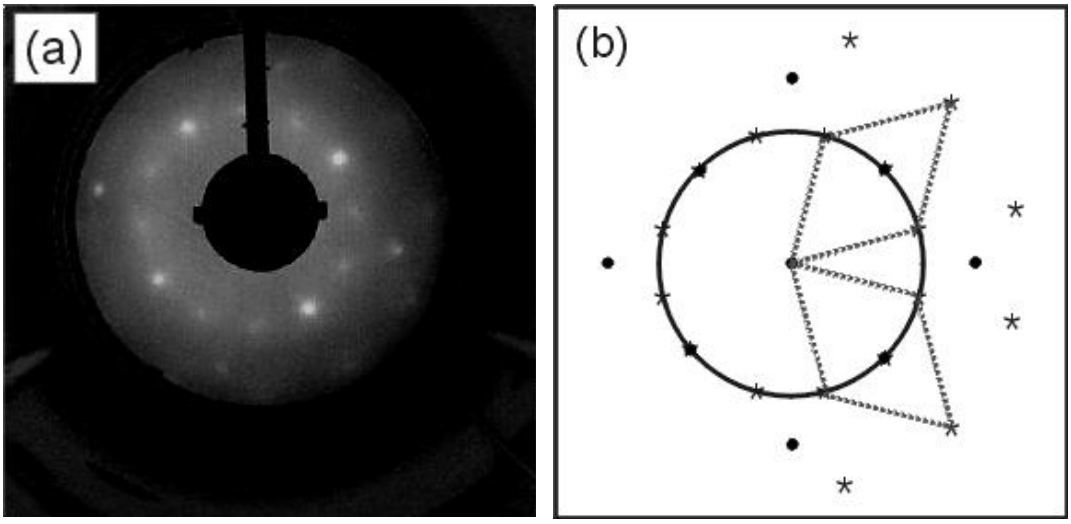

Figure 5.9: *(a) LEED image of the oxide after annealing to 1200 K. The primary energy was 122 eV. (b) Schematic representation: substrate spots are indicated by dots, spots stemming from the oxide are indicated by asterisks.*

in the LEED images at 900 K. Further annealing of the oxide layer results in enhanced contrast in the LEED images. The LEED image obtained after annealing to 1200 K is shown in Fig. 5.9(a) together with a schematic representation (b). 1200 K seems to be the temperature where the oxide has the best order. In the LEED pattern a twelvefold ring structure is observed, which can be interpreted in terms of two domains with hexagonal structure which are rotated by an angle of $n \cdot 30°$ (n odd) with respect to each other. An angle of rotation of 90° appears reasonable in view of the square lattice (C_4 symmetry) of the substrate. In order to determine the structure of the Al_2O_3 film the EELS data have to be considered again. In α-Al_2O_3 the Al^{3+} ions occupy only octahedrally coordinated sites resulting in two IR active modes, and therefore α-Al_2O_3 exhibits only two losses in the EEL spectra [67] and not three. Hence, the formation of α-Al_2O_3 can be ruled out. Consequently, the hexagonal surface structure has to be explained by the (111) plane of a cubic phase of Al_2O_3, that grows with the (111) plane of the oxide parallel to the (100) plane of the nickel substrate. The lattice constant of the hexagonal unit cell is $a_{\mathrm{hex}} = (2.87 \pm 0.2)$ Å, which agrees well with the distance of two adjacent O^{2-} ions in the (111) plane of numerous cubic phases of Al_2O_3 [110]. The EELS data agree with those obtained by Podgursky et al. [12], who found phonon losses at 415, 640, and 875 cm^{-1} for the $Al_2O_3/Ni_3Al(100)$ system that was prepared by oxidation of the $Ni_3Al(100)$ surface at 1100 K. In LEED investigations Bardi et al. [13] found a hexagonal surface structure with a lattice constant of ~ 2.9 Å. Podgursky et al. [12] found a hexagonal surface structure

with a lattice constant of ~ 3 Å and additionally two hexagonal superstructures with lattice constants of 17.5 and 54 Å. Both authors concluded the existence of the γ'-Al_2O_3 phase. In the present work also the γ'-Al_2O_3 phase is found which grows with the (111) plane parallel to the Ni(100) substrate.

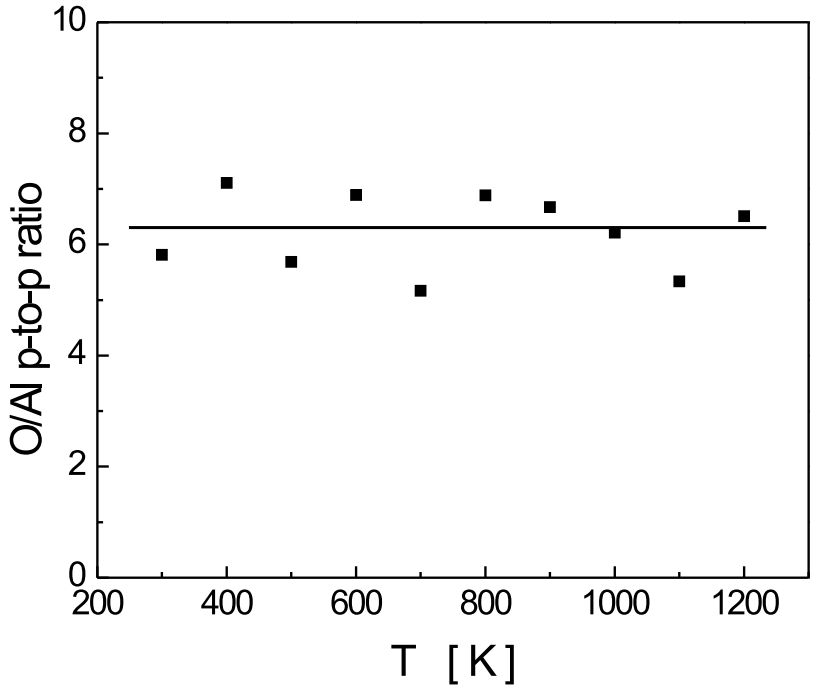

Figure 5.10: *Peak-to-peak ratio of O_{503}/Al_{1396} during the annealing of the oxide. The horizontal line is a guide to the eye.*

From the half width of the spots in the LEED image the domain size can be estimated, according to equation (3.19), to be about 30 Å. The thickness of the oxide film, after annealing to 1200 K, amounts to (8 ± 2) Å. However, it can not be claimed that the oxide film is grown on the Ni(100) substrate without an interface layer, since no information can be obtained from the experiments about the hidden interfaces Al_2O_3/Ni_3Al and Ni_3Al/Ni(100). However, the Ni_3Al film is destroyed at around 1200 K, and it is likely that this is also the case after the annealing of the oxide covered Ni_3Al layer.

Fig. 5.10 shows the ratio of the peak-to-peak intensities of O_{508}/Al_{1396} as a function of the annealing temperature, which does not change with temperature, and the average value is ~ 6.2. Thus it seems reasonable to assume that no change in the stoichiometry occurs. From the value of 6.2 for the ratio and the relative

sensitivity factors of 0.4 for oxygen and 0.09 for aluminum [30] the ratio between the amount of O and Al ions in the oxide layer is determined to be ≈ 1.4. This is close to the value of 1.5 for Al_2O_3, and the difference is readily explained by the experimental inaccuracy.

Summarizing, the oxidation of the $Ni_3Al/Ni(100)$ system at room temperature produces an aluminum oxide layer, which consists of amorphous and disordered phases of Al_2O_3. Upon annealing, the oxide transforms into γ'-Al_2O_3 which grows with the (111) plane parallel to the (100) plane of the substrate. The two-dimensional lattice constant is found to be 2.87 ± 0.2 Å, which agrees with the distance between two O^{2-}-ions in the (111) plane of fcc-oxygen. The thickness of the γ'-Al_2O_3 film is 8 ± 2 Å, which corresponds to approximately twice the lattice constant of γ'-Al_2O_3 (a = 3.95 Å).

5.3 Oxidation of the $Ni_3Al(100)/Ni(100)$ System at 800 K

The oxidation of the $Ni_3Al(100)$ surface at elevated temperatures has been studied by e.g. Bardi et al. [13] (800 K and 1000 K), Costina [11] (1100 K), and Podgursky et al. [12] (1100 K). The results found in these works are similar but not identical to that found by Bardi et al., who observed a LEED pattern with a twelvefold ring structure similar to the one of Fig. 5.9. The oxidation of the system $Ni_3Al/Ni(100)$ at 1100 K was tried in this work, but was not successful, because of the decomposition of the Ni_3Al layer, and the diffusion of Al into the bulk of the substrate proceeded faster than the oxidation process. Thus the oxidation of $Ni_3Al/Ni(100)$ at a lower temperature, 800 K, was investigated.

Fig. 5.11 shows the peak-to-peak ratios of O_{503}/Al_{1396} and O_{503}/Ni_{1396} for the oxidation of $Ni_3Al(100)/Ni(100)$ at 800 K as a function of oxygen exposure up to a total amount of 3500 L of oxygen. Saturation is reached at an exposure of 2500 L, which is substantially higher than that for the room temperature oxidation (Fig. 5.5). The thickness of the film after the oxidation is ~ 5 Å. The saturation value of ~ 4.5 for O/Al is lower than the one expected for bulk Al_2O_3 (which is 6.2 according to [33]). This can be understood, because the film thickness is less than the mean free path of the electrons of the KLL transition of Al at 1378eV. Accordingly, neutral Al atoms from the Ni_3Al alloy underneath the Al_2O_3 film contribute to the Al signal, which leads to a reduction of the ratio O/Al. A model of this situation is shown on the left side of Fig. 5.12. According to Cabrera and Mott [106] a logarithmic growth law for the thickness of the oxide film during the oxidation of metals is expected for low temperatures. For high temperatures a parabolic growth law is expected. In Fig. 5.11 the dashed line represents a fit with a logarithmic growth law and the dotted line represents a fit

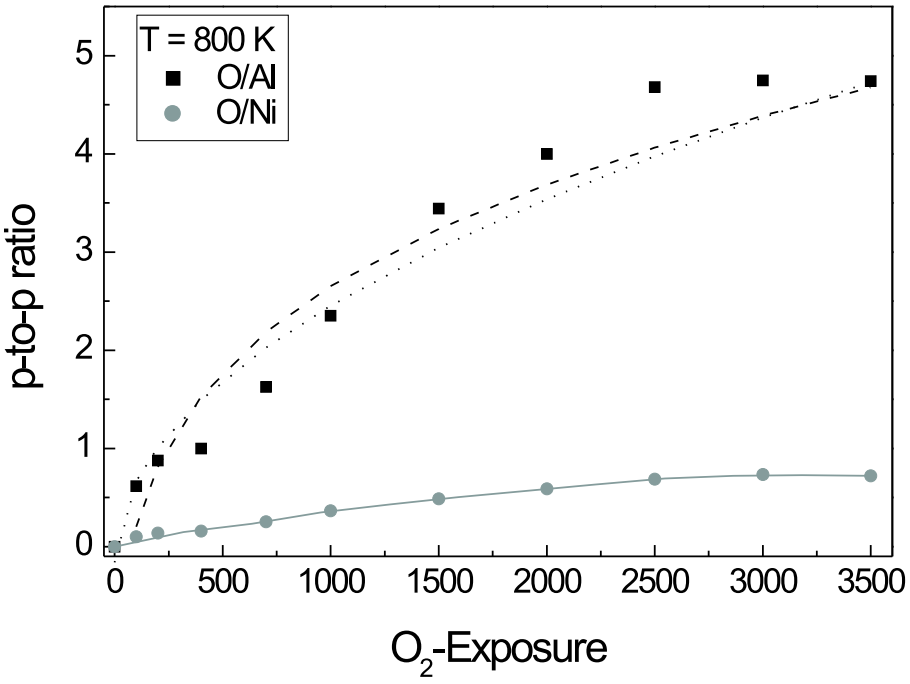

Figure 5.11: *Peak-to-peak ratios of O_{503}/Ni_{848} and O_{503}/Al_{1396} during oxidation at 800 K. Both ratios reach a saturation at 2500 L, and the saturation value is lower than the one of bulk Al_2O_3. The O/Al ratio was fitted with a logarithmic growth law (dashed line) and a parabolic growth law (dotted line).*

with a parabolic growth law. The logarithmic growth law seems to be in better agreement with the data. This was also found by Rose [111] who studied the oxidation of CoAl(100) at 800 K.

Upon annealing of the film, the ratio O/Al increases for temperatures between 800 and 1100 K, as can be seen in Fig. 5.12. In the temperature range 1250–1350 K a saturation level is reached. Since the ratio O/Ni is constant between 800 and 1200 K, the increase of the O/Al ratio between 800 and 1100 K is due to a decrease of the Al signal. This decrease results from the diffusion of some of the unoxidized Al, which is present in the Ni_3Al interface layer, into the substrate. The final value of ~ 9 of the O/Al ratio is higher than the one of bulk Al_2O_3, because the mean free paths of electrons contributing to the Al signal (1378 eV) and the electrons contributing to the O signal (503 eV) are different: 24 Å for the Al transition and 13 Å for the O transition. Thus the volume that contributes to the Al signal in bulk Al_2O_3 is larger, which means that the Al signal is stronger diminished than the O signal when the film thickness is comparable to the mean free path. Hence, the ratio O/Al is enlarged. The thickness of the oxide film after annealing is only about 4 Å, which corresponds to the lattice constant of

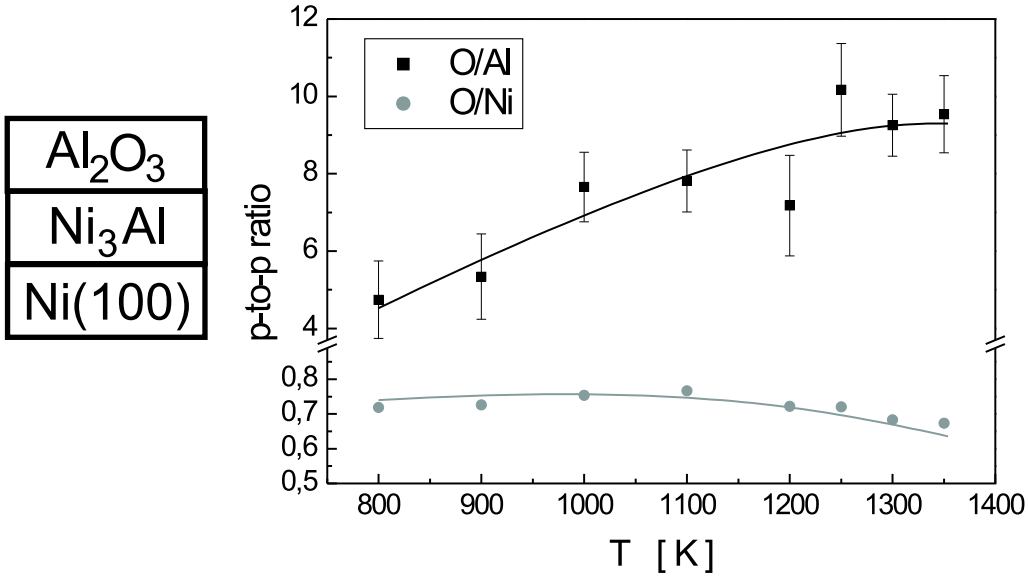

Figure 5.12: *Peak-to-peak ratios of O_{503}/Ni_{848} and O_{503}/Al_{1396} during annealing. The ratio O/Al increases and at 1250 K clearly exceeds the value of bulk Al_2O_3 of 6.2. The ratio O/Ni is constant up to 1100 K and above 1200 K decreases.*

bulk γ'-Al_2O_3 of 3.95 Å (see table 4.3).

The structural properties of the film are similar to those of the film which was prepared by room temperature oxidation and subsequent annealing. The EEL spectrum in Fig. 5.13 taken after annealing to 1200 K also shows three losses at 420, 650, and 880 cm^{-1}. For the room temperature oxidation of the $Ni_3Al(100)$ system and annealing to 1200 K, shown in Fig. 5.8, the losses are at 420, 620, and 880 cm^{-1}. Whereas the intensity of the loss at 640 cm^{-1} is higher than the intensity of the loss at 420 cm^{-1} in Fig. 5.8, the losses in Fig. 5.13 at 650 and 420 cm^{-1} show the same intensity. In addition, in Fig. 5.13 the energy gains at - 855, - 630, and - 410 cm^{-1} as well as the multiple and combination losses at 1280 ($\approx$ 420 + 880), 1520 ($\approx$ 650 + 880), and 1770 ($\approx$ 880 + 880) cm^{-1} are shown. The intensities of gains and losses are related by the Boltzmann statistics via $I_g = I_l \cdot \exp(\frac{-\hbar\omega}{kT})$, where the index g means gain and the index l means loss. This allows the determination of the sample temperature. If the loss at 880 cm^{-1} is analyzed, the sample temperature is determined to be 278 ± 15 K, which is in reasonable agreement with the thermocouple controlled sample temperature of 300 K during the measurement.

After oxidation of the $Ni_3Al(100)/Ni(100)$ surface at 800 K and after annealing

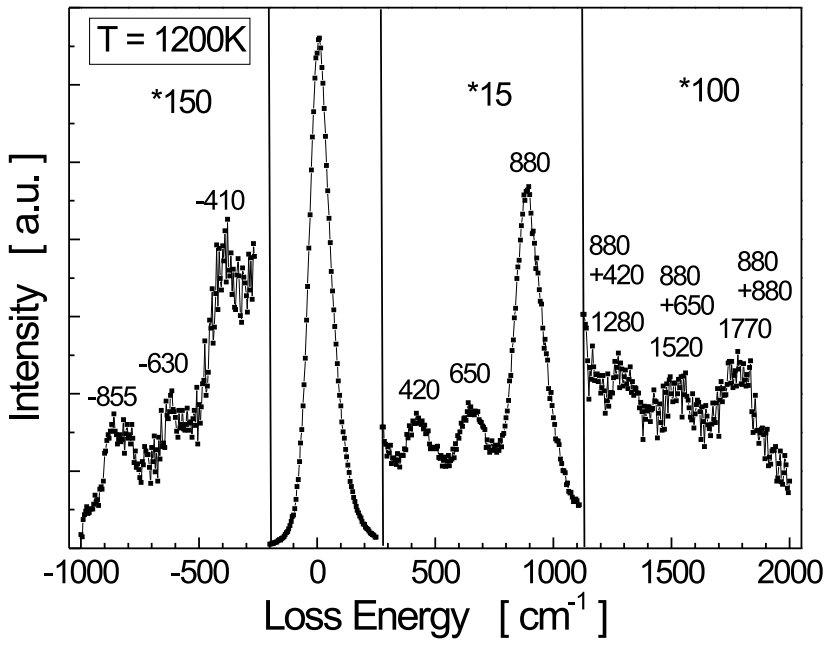

Figure 5.13: *EEL spectrum of the Al_2O_3 film after annealing to 1200 K showing energy gains (-855, -630, and -410 cm^{-1}), energy losses (420, 650, and 880 cm^{-1}), and double losses (1280, 1580, and 1780 cm^{-1}). The spectrum was measured at room temperature.*

to 1350 K LEED images were recorded. In part (a) of Fig. 5.14 the LEED pattern of the Ni(100) substrate is shown for better comparison. At 800 K the LEED pattern consists of a weak diffuse ring structure (b). This suggests that the film grows in hexagonal domains which are randomly oriented with respect to the Ni(100) substrate. The lattice constant of the hexagonal unit cell amounts to 2.9 ± 0.3Å.

During annealing of the film to higher temperatures the LEED pattern gradually transforms to the one shown in Fig. 5.14(c). This pattern consists of 36 sharp spots that are arranged on a ring. It is again indicative of domains with a hexagonal unit mesh with a lattice constant of 2.89 ± 0.2 Å. The pattern can be interpreted in terms of 6 domains with a hexagonal surface structure that are rotated by an angle of 15°.

The main results of the interpretation of the LEED pattern taken from the room temperature oxidation apply: Due to the 3 losses in the EEL spectrum an Al_2O_3 phase is formed, which is different from the α- or the amorphous phase. Since the two-dimensional structure is hexagonal, with a lattice constant of ~ 2.9 Å, we conclude that the cubic γ'-Al_2O_3 is formed, which grows with the

(111) plane parallel to the substrate surface. The domain size is again estimated from the half width of the spots to be 35 Å.

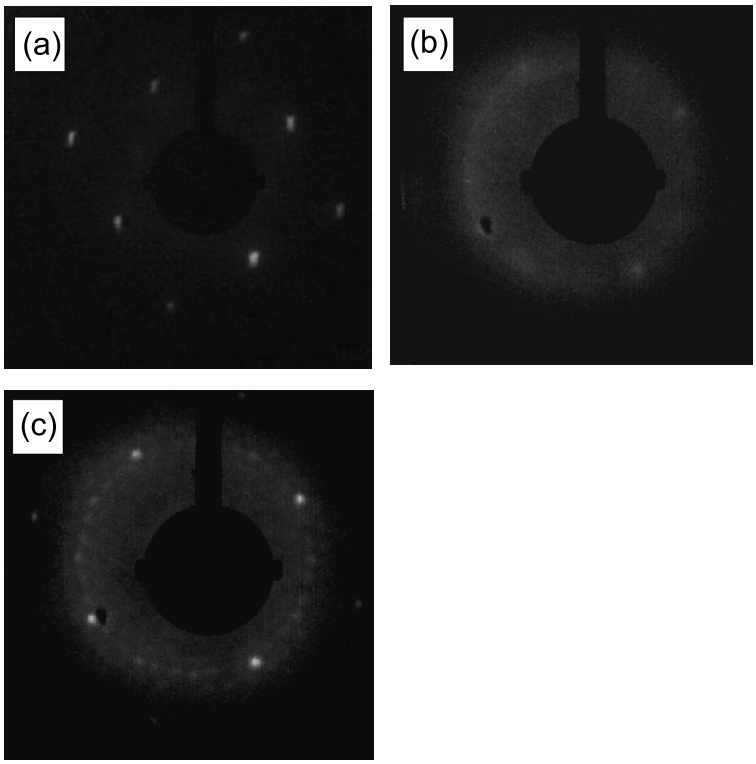

Figure 5.14: *LEED images of (a) the clean Ni(100) surface, (b) after oxidation of the $Ni_3Al/Ni(100)$ system at 800 K, and (c) after annealing to 1350 K. The primary energy was 122 eV for all of the images.*

For the oxidation of bulk $Ni_3Al(100)$ at 800 K Bardi et al. [13] found a LEED pattern displaying a twelvefold ring structure. This pattern was explained in terms of "a hexagonal overlayer mesh". This pattern is similar to the one of Fig. 5.9. The LEED pattern of Fig. 5.14 observed in this work differs from these only by the number of domains which are formed.

Resuming, the results of this section are similar to the results of the preceding section. Upon oxidation of the $Ni_3Al/Ni(100)$ system at 800 K and subsequent annealing, a film of γ'–Al_2O_3 is formed. The film grows with the (111) plane parallel to the (100) plane of the substrate, and the thickness of the film after annealing to 1200 K is about 4 Å, which corresponds to the lattice constant of bulk γ'-Al_2O_3 (3.95 Å). The film grows in 6 domains rotated by 15° with respect to each other.

5.4 Deposition and Oxidation of Al on Ni(100)

In the preceding two sections the oxidation of the Ni_3Al/Ni(100) system was investigated and ordering of the Al_2O_3 layer was achieved by annealing. For technological reasons it would be desirable to establish a method to grow ordered oxide films on the Ni(100) surface without forming an alloy before oxidation. In this section the deposition and oxidation of Al on Ni(100) is analyzed.

A 12 Å thick layer of Al was deposited on the Ni(100) surface and subsequently oxidized with oxygen at room temperature until the ratio O/Al showed a saturation level.

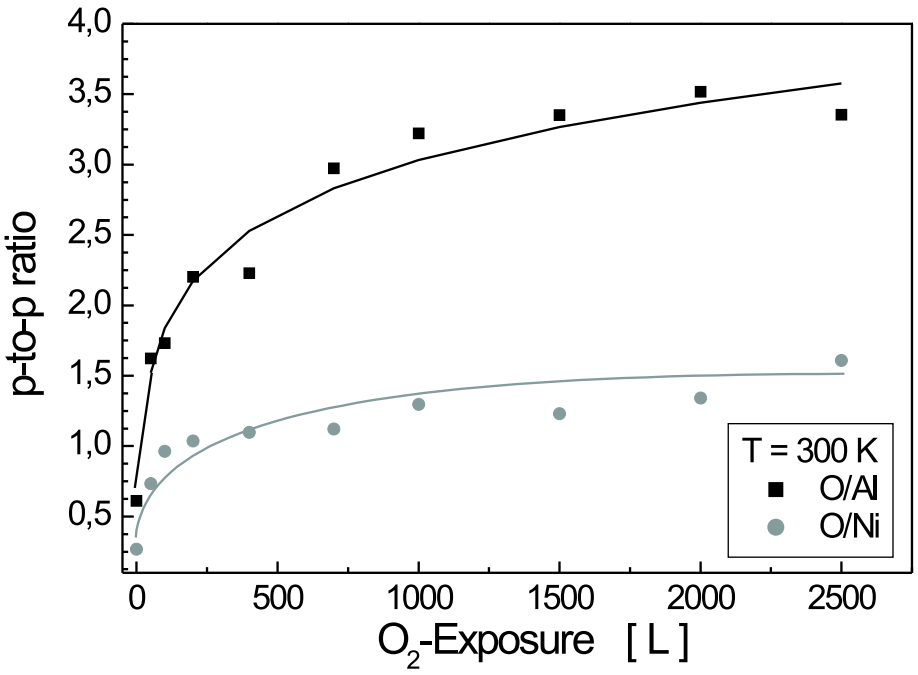

Figure 5.15: *Peak-to-peak ratios of O_{503}/Ni_{848} and O_{503}/Al_{1396} for the oxidation of Al/Ni(100). The saturation value of O/Al is about 3.5.*

The peak-to-peak ratios of O_{503}/Al_{1396} and O_{503}/Ni_{848} during oxidation of the Al/Ni(100) system at room temperature are shown in Fig. 5.15. The O/Al ratio was fit by a logarithmic growth law of the type of equation (5.1), which is typical for the oxidation of metals at low temperatures [106]. The saturation is reached at a total exposure of about 1500 L. The saturation value of ∼3.5 for O/Al is lower than the one expected for bulk Al_2O_3. A possible explanation for this is

that the Al film is not completely oxidized, and unoxidized Al contributes to the Al signal. Unfortunately, the signals of the AES LMM transition for Al at 1396 eV and for Al^{3+} at 1378 eV were not resolved separately. However, further evidence for the existence of unoxidized Al can be gained from the low energy range of the AES spectra, and is given in the context of Fig. 5.17. This means that after the oxidation there is a coexistence of unoxidized Al and Al_2O_3 as indicated by the schematic in the left side of Fig. 5.16.

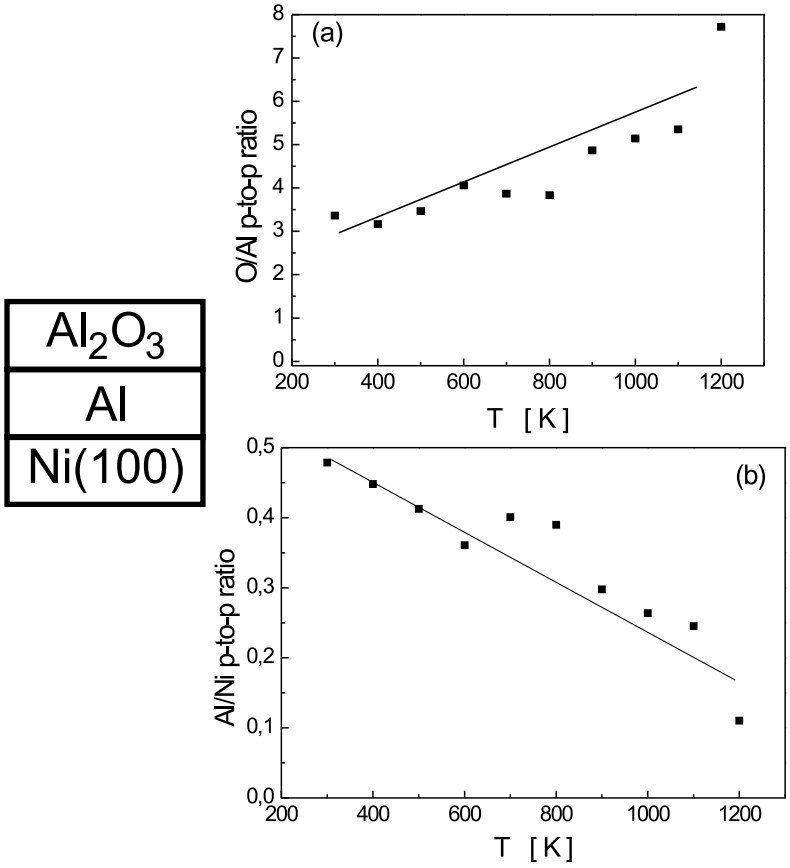

Figure 5.16: *Peak to peak ratio of O_{503}/Al_{1396} (a) and Al_{1396}/Ni_{848} (b) during annealing of the oxidized system Al/Ni(100). The lines are a guide to the eye.*

The film is then annealed up to 1200 K in steps of 100 K. Each annealing step lasted for 2 minutes and the sample was cooled to room temperature before the measurements were performed. The peak-to-peak ratios of O/Al and Al/Ni are shown in Fig. 5.16 (a) and (b), respectively. Between 500 and 1100 K the ratio O/Al increases due to the diffusion of Al into the bulk. This diffusion process is

proved by the formation of an alloy of Al and Ni which was discussed in section 5.1. The decrease of the Al/Ni ratio can also be explained by the diffusion of metallic Al into the substrate. The ratio O/Ni (not shown) is constant for annealing temperatures up to 1100 K indicating that only metallic Al is involved in the diffusion processes. Only after annealing to 1200 K decomposition and desorption of the oxide film takes place, which is discussed below in the context of the thickness of the film.

The Auger spectra of Fig. 5.17 give further evidence of the composition of the film. Spectrum (a) is taken from the clean Ni(100) surface, and it thus exhibits only the two MNN transitions of Ni at 61 and 102 eV [33]. Spectrum (b) is taken after the deposition of the 12 Å thick Al film and, accordingly, only the LMM transition of metallic Al at 68 eV is observed. The transitions of Ni are not observed, because the thickness of the Al film is large compared to the mean free path of electrons with energies of 61 and 102 eV ($\lambda \leq 5$ Å) that correspond to the MNN transitions of Ni. The crucial spectrum in this figure is (c), taken after oxidation, where three transitions at 35, 55, and 65 eV are observed. The transition at 35 eV is clearly due to Al^{3+}. The transitions at 55 and 65 eV are most likely due to the transition of Al^{3+} at 51 eV and the transition of Al^0 at 68 eV, respectively, and are shifted towards each other due to overlapping. Spectrum (d) is taken after annealing to 1200 K, and only the transitions of Al^{3+} at 35, 43, and 51 eV are observed, because the metallic Al atoms diffused into the bulk of the Ni(100) substrate.

The thickness of the film can be determined from the AES data. The Al film that is initially deposited on the Ni(100) substrate has a thickness of 12 Å, which is proved by the calibration of the evaporator and is verified by the AES data. After oxidation the estimation of the thickness of the film cannot be performed in a straightforward manner, because the Al film is not completely oxidized and the mean free paths of electrons in unoxidized Al and Al_3O_3 are different. If the mean free path of electrons in Al_2O_3 is used in equation (3.4), the thickness of the film after oxidation at 300 K amounts to 15.4 ± 2 Å. After annealing to 1100 K there is most likely no unoxidized Al in the surface region, and thus the use of the mean free path of electrons in Al_3O_3 is correct. The thickness is then 11.1 ± 2 Å. Upon annealing to 1200 K partial desorption of the oxide film sets in and the residual thickness is only 8 ± 2 Å.

EEL spectra of the film after oxidation are shown in Fig. 5.18. At room temperature only one very broad loss feature is observed at about 880 cm^{-1}. At this stage the Al_2O_3 is probably amorphous and the loss at $\sim 635\,cm^{-1}$, that is also characteristic for amorphous Al_2O_3 [81] is not resolved. After annealing to 800 K three losses emerge, and are still present after annealing to 1200 K. These three losses are characteristic Fuchs-Kliewer-Phonons of those phases of

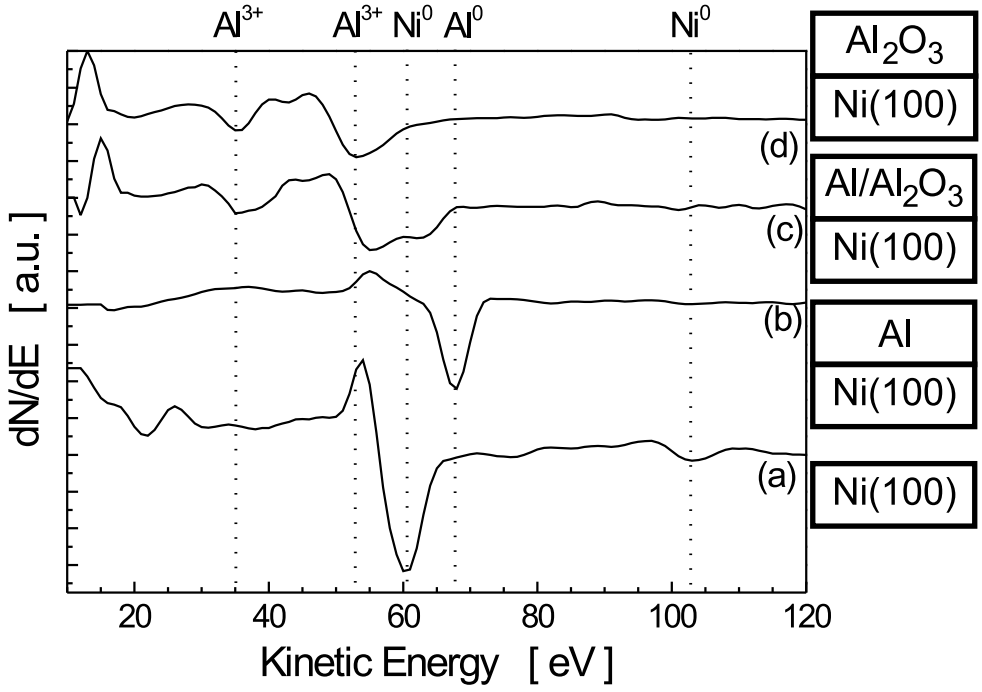

Figure 5.17: *AES spectra taken of the clean Ni(100) surface (a), after deposition of 12 Å Al (b), after oxidation to saturation (c), and after annealing to 1200 K (d).*

alumina, where octahedral and tetrahedral sites are occupied by the Al^{3+}-ions. The decrease of the magnification factor in Fig. 5.18 indicates an increase of the intensity of the spectra for higher annealing temperatures and, accordingly, an increase of the order of the oxide. However, since no LEED pattern is observed, a phase of Al_2O_3 with long range order cannot be identified. A hint of the lack of ordering can also be obtained from the rather broad elastic peak of the EEL spectrum after annealing to 1200 K which is shown in Fig. 5.18 (FWHM = 105 cm^{-1}).

As mentioned before, annealing at 1200 K results in desorption of the oxide film. It has thus been tried to anneal the film at 1100 K for longer times to achieve a better ordering, but also this method did not result in LEED patterns. Therefore, it has to be concluded that by deposition and oxidation of Al on Ni(100) and subsequent annealing of the oxidized film no ordered Al_2O_3 film can be grown.

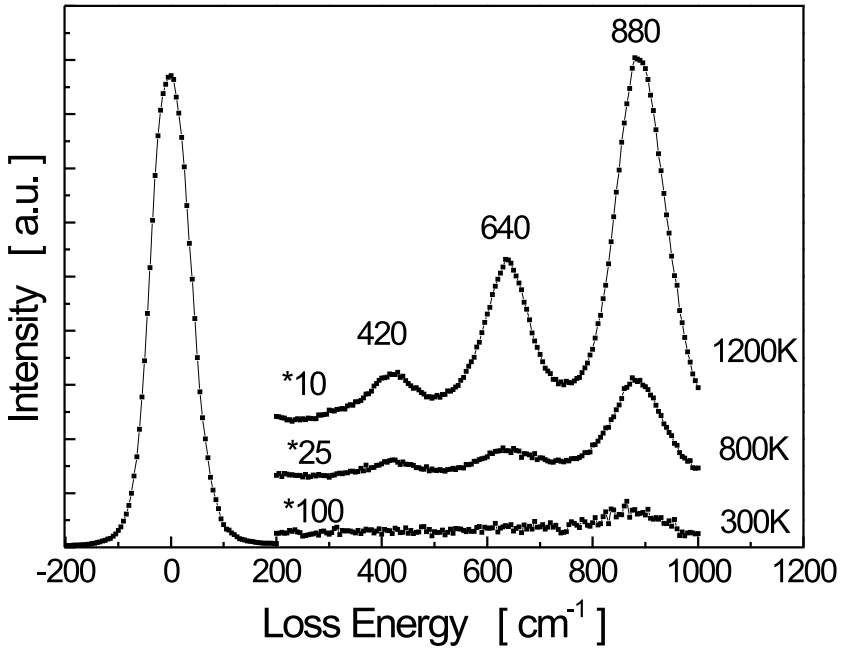

Figure 5.18: *EEL spectra after annealing to different temperatures with characteristic losses at 420, 640, and 880 cm^{-1}. The spectra were recorded at room temperature.*

5.5 Deposition of Al on Ni(100) in Oxygen Atmosphere

It turned out in the previous section that the oxidation of the 12 Å Al/Ni(100) system at 300 K did not result in a completely oxidized Al film, although during oxidation the peak-to-peak ratios of O/Ni and O/Al showed a saturation level. In principle, it is possible to deposit a very thin layer of Al which may be completely oxidized. Thicker layers of Al_2O_3 are then achieved by multiple repetitions of deposition and oxidation. However, a more convenient method to grow an Al_2O_3 film has been tried: The deposition of Al in an oxygen atmosphere. Here, the adjustment of the partial pressure of oxygen is crucial. On the one hand, the pressure must be high enough to form stoichiometric Al_2O_3 for a given deposition rate. On the other hand, the pressure should not be too high, because at high pressures the mean free path of the deposited particles is diminished. First, there is no reason, that an Al_2O_3 film prepared in this a way gets a better ordering,

but it turns out, that the film can be annealed to higher temperatures resulting in ordering.

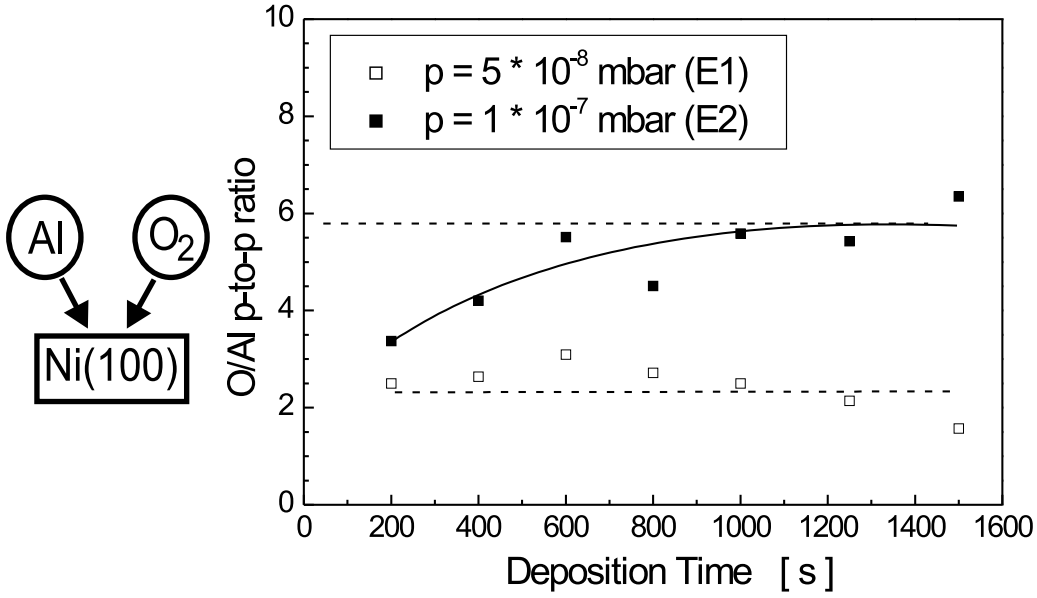

Figure 5.19: *O_{503}/Al_{1396} peak-to-peak ratio during deposition in $p_{O_2}= 5\cdot10^{-8}$ mbar (E1) and $p_{O_2}= 1\cdot10^{-7}$ mbar (E2).*

Two different experiments are discussed in this section. In the first one, the deposition has been performed at a partial pressure of oxygen (p_{O_2}) of $5\cdot10^{-8}$ mbar with a deposition rate of 0.48 Å/min. For simplicity this experiment will be denoted as E1. In the second experiment the deposition rate was not changed, but p_{O_2} was $1\cdot10^{-7}$ mbar and it will be denoted as E2. In both experiments the film was then further oxidized up to a total exposure of 2500 L of oxygen und subsequently annealed in steps of 100 K from room temperature to 1400 K. In the case of the lower partial pressure during deposition (E1) the film was completely desorbed after annealing to 1300 K, but in the case of the higher partial pressure (E2) the film could be annealed to 1400 K without being desorbed.

Fig. 5.19 shows the O_{503}/Al_{1396} peak-to-peak ratio (O: KLL-transition at 503 eV, Al: KLL-transition at 1396 eV) of the AES spectra taken during deposition. For E2 ($p_{O_2}= 5\cdot10^{-8}$ mbar) the ratio is constant within the experimental error and the average value is 2.5 and thus lower than the one expected for bulk Al_2O_3 [33]. Therefore it is likely that the Al is not completely oxidized.

For E2 ($p_{O_2}= 1\cdot10^{-7}$ mbar) the experimental error is quite large, however, the

average value of O/Al ratio (5.8) corresponds closely to the value of bulk Al_2O_3. In principle it is possible to form stoichiometric Al_2O_3 with the deposition rate of 0.48 Å/min and a partial pressure of $1 \cdot 10^{-7}$ mbar, as follows from the kinetic gas theory. The atomic radius of Al is 1.43 Å and hence the diameter of an Al atom is 2.86 Å, which means that the thickness of 2.86 Å roughly corresponds to one monolayer of fcc Al. From the deposition rate of 0.48 Å/min then follows, that one monolayer of fcc Al is deposited in 358 s. In the following the growth of a fcc Al layer is assumed, that grows with the (100) plane parallel to the (100) plane of the substrate. From the lattice constant of 4.05 Å for fcc Al it follows that the Al layer contains $1.22 \cdot 10^{15}$ atoms/cm^2. Thus, during the deposition of 1 ML of aluminum $1.22 \cdot 10^{15}$ atoms must be oxidized, if stoichiometric Al_2O_3 is formed.

The number of particles that hit a surface per square centimeter and second for a given temperature and pressure is given by [112]

$$\dot{n}_s \left[\frac{1}{\mathrm{cm^2 s}}\right] = 2.63 \cdot 10^{22} \cdot \frac{p[\mathrm{mbar}]}{\sqrt{T[\mathrm{K}] \cdot M_r}}. \tag{5.2}$$

The number of oxygen atoms that hit the surface during deposition of one monolayer is therefore given by $n = 358\,\mathrm{s} \cdot 2 \cdot \dot{n}_s$, where the factor of two enters due to the dissociation of the O_2-molecules. Here, the assumption is made that the sticking coefficient is one. The results for the different pressures are (T = 300 K, $M_r = 32$ for oxygen):

- $\mathrm{p_{O_2}} = 5 \cdot 10^{-8}$ mbar $\quad \Rightarrow \quad n = 5.18 \cdot 10^{16}$
- $\mathrm{p_{O_2}} = 1 \cdot 10^{-7}$ mbar $\quad \Rightarrow \quad n = 1.03 \cdot 10^{17}$

Thus, under these assumptions, for both of the partial pressures the number of oxygen atoms incident on the surface in 358 s exceeds the number of Al atoms incident on the surface in the same time by more than a factor of 1.5. Thus, both of the partial pressures are sufficient to form stoichiometric Al_2O_3. However, the assumption of a sticking coefficient of one may not be valid. Also it is neglected that some Al atoms react with oxygen before reaching the substrate surface. The probability for an Al atom to hit an oxygen molecule in a partial pressure of $\mathrm{p_{O_2}} = 1 \cdot 10^{-7}$ mbar and for a distance of evaporator and substrate of 0.1 m is about 1%. Hence, the reaction of Al with oxygen in the gas phase can be neglected.

For the film prepared by deposition in an oxygen atmosphere of $\mathrm{p_{O_2}} = 5 \cdot 10^{-8}$ mbar, further oxidation results in a clear increase of the O/Al ratio, as can be seen in Fig. 5.20(a). The saturation is reached at an exposure of about 1000 L, which is lower than the exposure of 1500 L needed in the preceding section for the oxidation of a pure Al film. During deposition the film is exposed to a nominal exposure of oxygen of 57 L. However the real amount is larger, because at the

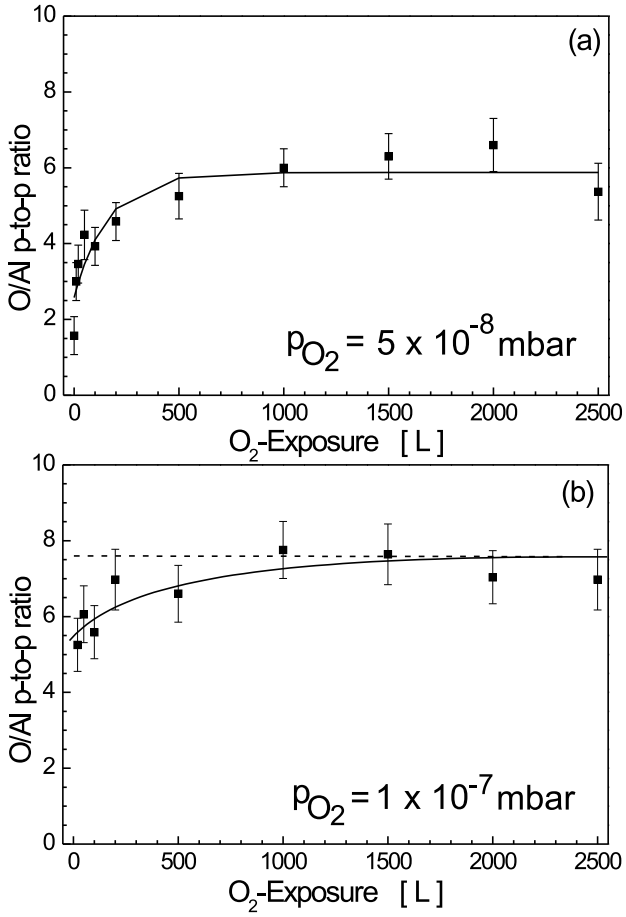

Figure 5.20: *Peak-to-peak ratio of O_{503}/Al_{1396} for E1 (p_{O_2}= $5 \cdot 10^{-8}$ mbar) (a) and E2 (p_{O_2}= $1 \cdot 10^{-7}$ mbar) (b).*

end of the deposition time the shutter of the evaporator was closed first and then the gas inlet was disconnected from the chamber. The saturation value of about 6.2 corresponds to the value for bulk Al_2O_3, but it has been argued before, that for thicknesses of alumina films smaller than the mean free path of the electrons of the Al KLL transition at 1396 eV, which is 24 Å, the ratio O/Al is expected to be larger than for bulk Al_2O_3. Thus it is still possible, that the film is not completely oxidized.

For E2 (deposition in p_{O_2}= $1 \cdot 10^{-7}$ mbar) the ratio O/Al is shown in Fig. 5.20(b). The experimental error is again quite large and there is only a slight increase. The value after oxidation is about 7.6, which is larger than 6.2 for bulk Al_2O_3. An explanation for the ratio of a thin film of alumina being larger

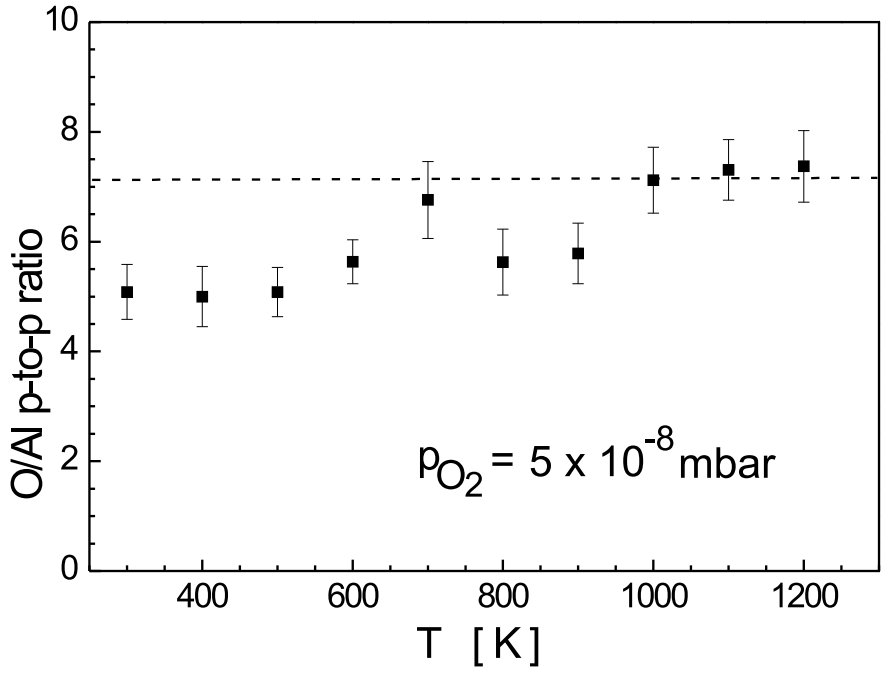

Figure 5.21: *Peak-to-peak ratio of O_{503}/Al_{1396} as a function of the annealing temperature for E1 (deposition in $p_{O_2} = 5 \cdot 10^{-8}$ mbar).*

than the one for bulk alumina is based on the different mean free path λ, i.e. the different escape depths, of electrons of the AES transition of Al at 1396 eV and O at 503 eV. Since $\lambda(1396)\,\mathrm{eV} < \lambda(503)\,\mathrm{eV}$, the AES signal of Al is stronger diminished than the AES signal of O for a thin film of Al_2O_3 with respect to bulk Al_2O_3. This leads to an increase of the O/Al ratio for thin alumina films compared to bulk alumina films.

As in the preceding section the ratio of O/Al has also been analyzed during the annealing of the oxidized film, which is shown in Fig. 5.21 for E1 (deposition in $p_{O_2} = 5 \cdot 10^{-8}$ mbar). The annealing proceeded in steps of 100 K, and the temperature is maintained for two minutes for each step. For annealing temperatures above 900 K the ratio is clearly increased in comparison to temperatures below 600 K. This is most likely a consequence of the diffusion of unoxidized Al atoms just as for the annealing of the oxidized pure Al film in the preceding section (Fig. 5.16). The value of the O/Al ratio at annealing temperatures of 1000 K and above is about 7.

For E2 (deposition in $p_{O_2} = 1 \cdot 10^{-7}$ mbar) the ratio O/Al during annealing is

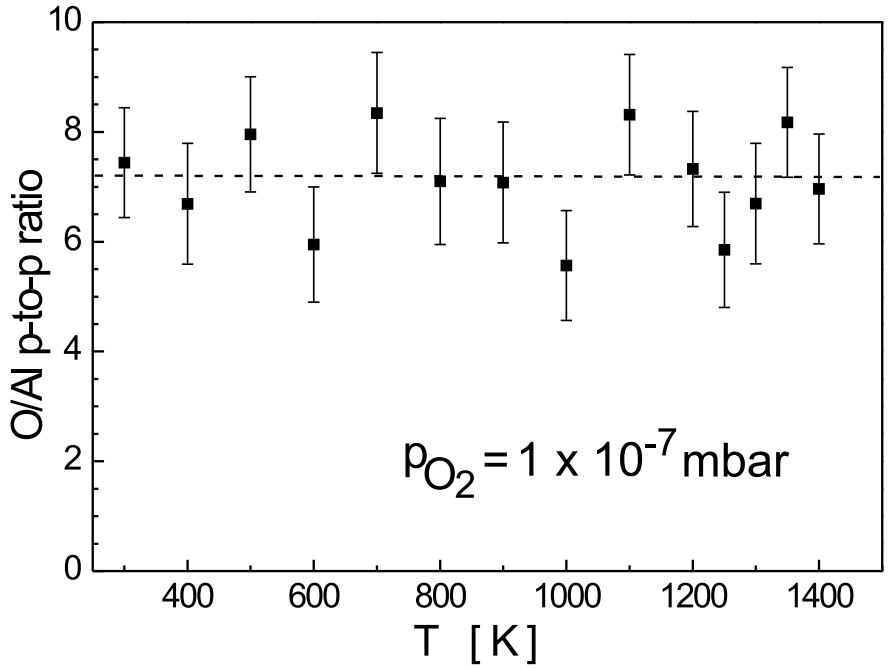

Figure 5.22: *O_{503}/Al_{1396} peak-to-peak ratio as a function of the annealing temperature for E2 (deposition in $p_{O_2} = 1 \cdot 10^{-7}$ mbar).*

shown in Fig. 5.22. Within the experimental error the ratio is constant and the average value is about 7.2. It is most likely that in this case the Al is completely oxidized after the oxidation process. Thus, no metallic Al is present in the film and, accordingly, no diffusion takes place.

Fig. 5.23 shows Auger spectra taken during the E2 process (deposition in $p_{O_2} = 1 \cdot 10^{-7}$ mbar). Spectrum (a) is taken from the clean Ni(100) surface and thus the two characteristic transitions of Ni at 61 and 102 eV are observed. Spectrum (b) is taken after the deposition of Al in an oxygen atmosphere with a partial pressure of oxygen of $p_{O_2} = 1 \cdot 10^{-7}$ mbar and only the transitions of Al^{3+} at 35 and 51 eV are observed. It is thus likely that the film is completely oxidized. (In principle, AES is not sensitive enough to rule out the existence of Al^0, because the detection limit of AES is about 1% of a monolayer [31].) After further oxidation of the system up to 2500 L at room temperature the spectrum (c) does not change significantly and only exhibits the characteristic transitions of Al^{3+}. The spectrum of Fig. 5.23(d) is taken after annealing to 1400 K, and the characteristic transitions of Al^{3+} are still observed. In addition, the transition of Ni at 61 eV reemerges, which is due

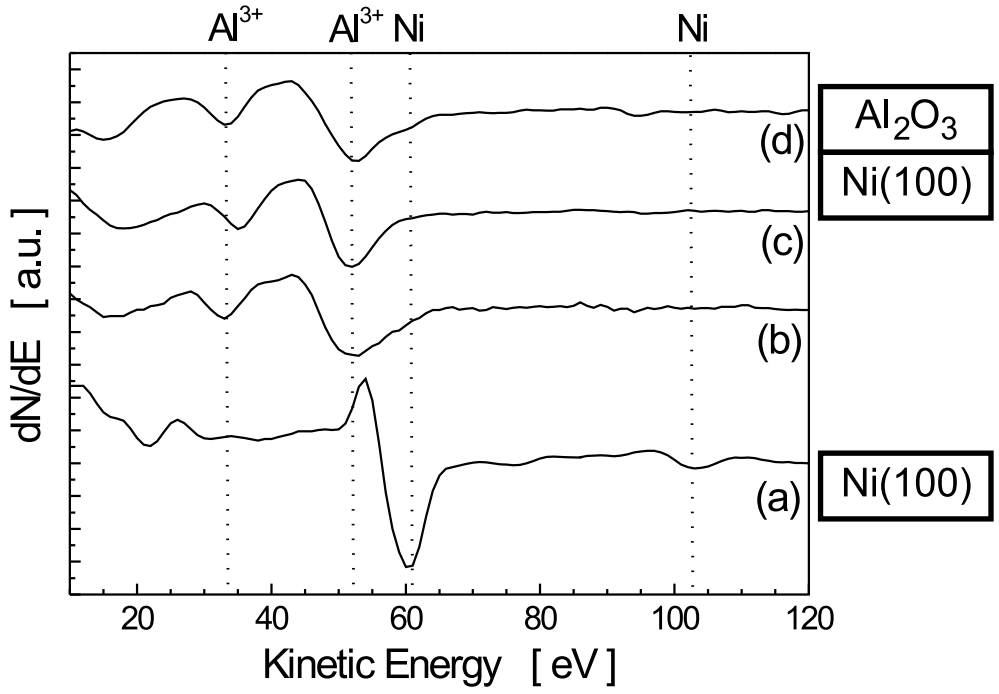

Figure 5.23: *AES spectra in the energy range 10 – 120 eV for E2. (a) clean Ni(100) surface, (b) after deposition of Al in* $p_{O_2} = 1 \cdot 10^{-7}$ *mbar, (c) after further oxidation to 2500 L* O_2*, and (d) after annealing the oxide film to 1400 K.*

to desorption of the Al_2O_3 film.

It is interesting to compare the thicknesses of the films that are prepared with different methods. At annealing temperatures as high as 1200 K and above it appears reasonable to assume that there is no metallic Al in the film, and that there is a sharp interface between the Ni(100) substrate and the Al_2O_3 film. Under this assumption the thickness of the films can be estimated by use of equation (3.4). The results are:

- Oxidation of a pure Al film at 300 K followed by annealing to 1200 K: $d_1 = 8 \pm 2$ Å
- E1 ($p_{O_2} = 5 \cdot 10^{-8}$ mbar) after annealing to 1200 K: $d_2 = 11.5 \pm 2$ Å
- E2 ($p_{O_2} = 1 \cdot 10^{-7}$ mbar) after annealing to 1200 K: $d_3 = 25.1 \pm 2$ Å
- E2 after annealing to 1300 K: $d_4 = 23.9 \pm 2$ Å

- E2 after annealing to 1400 K: $d_5 = 17.2 \pm 2$ Å

The error is again estimated from the background of the AES signals and the inaccuracy of the mean free path. The volume of an Al film is known to double upon oxidation [107]. Thus, the thickness d_3 appears to be reasonable in comparison to the thickness of the nominally deposited Al layer of 12 Å, in this case the whole deposited Al was oxidized. The decrease after annealing to 1400 K (d_5) is due to desorption and diffusion. In comparison to each other the thicknesses appear also reasonable ($d_1 < d_2 < d_3$), because for the oxidation of a pure Al layer under condition E1 (deposition of Al in $p_{O_2} = 5 \cdot 10^{-8}$ mbar) the Al is not completely oxidized, and some Al is lost due to diffusion into the bulk.

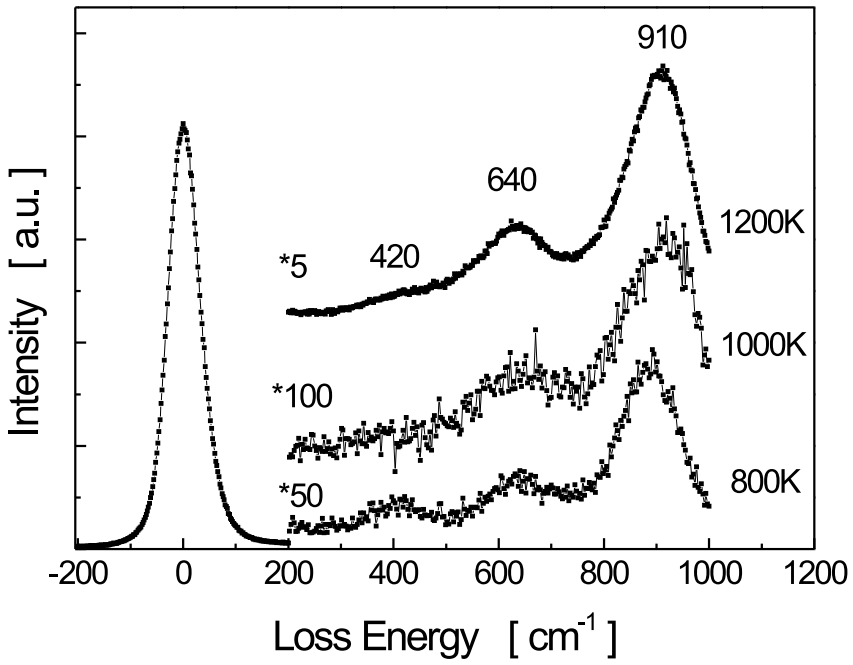

Figure 5.24: *EEL spectra (deposition in $p_{O_2} = 5 \cdot 10^{-8}$ mbar) at different annealing temperatures. The spectra were recorded at room temperature.*

In the following the ordering of the oxide is discussed on the basis of EELS and LEED data. Fig. 5.24 shows EEL spectra during annealing of the oxide in E1 (deposition in $p_{O_2} = 5 \cdot 10^{-8}$ mbar). The spectra at room temperature (not shown) and at 800 K resemble closely those of Fig. 5.18 for the oxidation of a pure Al film. The three losses are characteristic for phases of Al_2O_3, where the Al^{3+}-ions occupy octahedral and tetrahedral positions in an oxygen sublattice.

Upon annealing to temperatures above 800 K the intensity of the loss at 420 cm^{-1} decreases, but is still observed after annealing to 1200 K. The loss at 880 cm^{-1}, after annealing to 800 K, shifts to 910 cm^{-1} after further annealing to 1200 K. The intensity of the spectrum after annealing to 1000 K is lower than the intensity of the spectrum after annealing to 800 K. This is due to structural changes of the Al_2O_3 film. After annealing to 1200 K the intensity of the losses and of the elastic peak is drastically increased in comparison to all spectra taken after annealing to lower temperatures. The three dipole active modes at 420, 640, and 910 cm^{-1} are, as in the previous section, characteristic for Al_2O_3, where the Al^{3+}-ions occupy tetrahedral and octahedral sites in a sublattice of O^{2-}-ions. Annealing for longer than 2 minutes at 1200 K or annealing at higher temperatures results in the desorption of the oxide, and no LEED pattern is formed. Thus in this experiment an ordered phase of Al_2O_3 is not formed, but after annealing to 1200 K the Al^{3+}-ions occupy tetrahedral and octahedral sites.

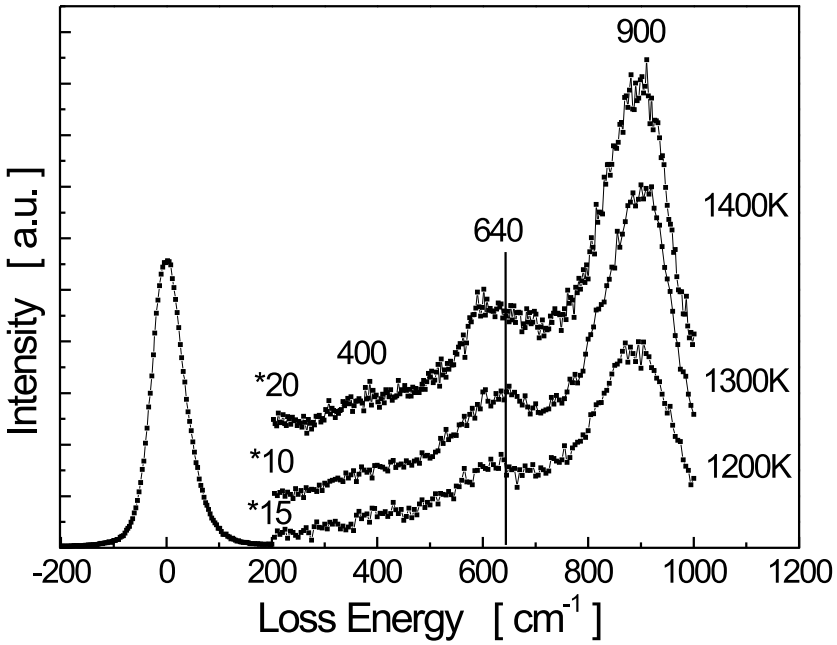

Figure 5.25: *EEL spectra from E2 (deposition in $p_{O_2} = 1 \cdot 10^{-7}$ mbar) at annealing temperatures of 1200, 1300, and 1400 K. After annealing to 1400 K three loss features are observed at 400, 640, and 900 cm^{-1}. The spectra were recorded at room temperature.*

Fig. 5.25 shows EEL spectra during annealing of the oxide film in E2 (depo-

sition in $p_{O_2} = 1 \cdot 10^{-7}$ mbar). Between room temperature and 1000 K only one very broad loss feature at about 880 cm^{-1} is observed (not shown). The spectra resemble the room temperature spectrum of Fig. 5.18 and the Al_2O_3 is probably amorphous. No significant change of the spectra is observed until annealing to 1100 K. After annealing to 1200 K three loss features are observed at 400, 640, and 890 cm^{-1}. As for annealing temperatures above 900 K in Fig. 5.24 (E1, deposition in $p_{O_2} = 5 \cdot 10^{-8}$ mbar) the intensity of the loss feature at 400 cm^{-1} is very low. After annealing to 1300 K the intensity of the losses is increased as indicated by the decrease of the magnification factor, and the positions of the losses remain the same. The loss at 890 cm^{-1} is shifted to 900 cm^{-1} upon annealing to 1400 K, and the intensity of the all loss features is decreased in comparison to the intensity of the spectrum recorded after annealing to 1300 K. This is most likely due to desorption and maybe decomposition of the Al_2O_3 film. The decrease of the thickness of the film after annealing to 1400 K has been discussed above.

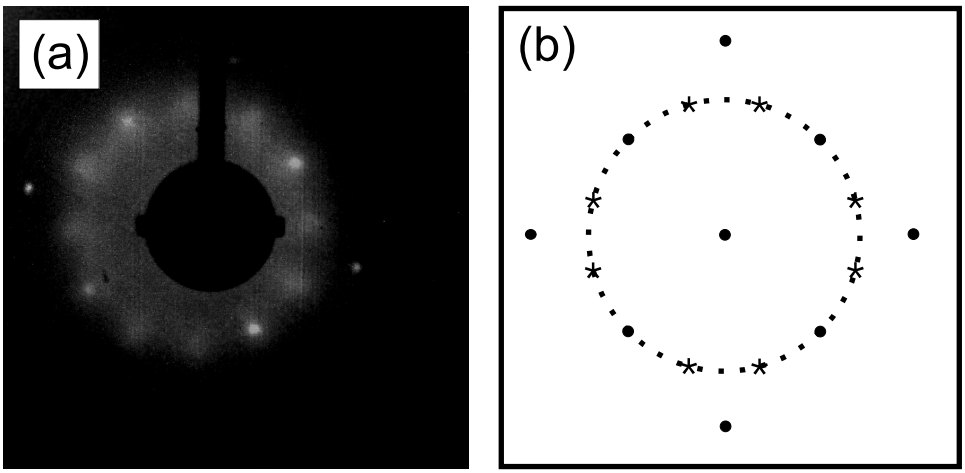

Figure 5.26: *LEED image of the oxide film after annealing to 1400 K (a). The primary energy was 122 eV. (b) schematic representation of the pattern in (a). Spots of the substrate are indicated by solid circles, spots of the oxide are indicated by asterisks.*

Fig. 5.26 shows a LEED image of the oxide film after annealing to 1400 K (a) and a schematic representation of the image (b). The primary energy was 122 eV and thus the pattern can be compared to the one of the clean Ni(100) surface in Fig. 5.4(a). The pattern is already observed after annealing to 1300 K, but the background intensity is reduced after annealing to 1400 K. The twelvefold ring structure is similar to the one obtained by room temperature oxidation and annealing of the Ni_3Al/Ni(100) system, and suggests that the oxide grows in two domains with hexagonal surface structure. These are rotated by an angle of 90°

with respect to each other, because of the square lattice (C_4 symmetry) of the substrate. The lattice constant of the hexagonal unit cell amounts to 2.9 ± 0.2 Å, which corresponds to the distance of the O^{2-}-ions in a close packed oxygen lattice [110].

There are, in principle, two possibilities for the origin of the hexagonal structure of the oxide. It is possible that the oxygen ions form a cubic (fcc) lattice, of which the (111) plane is parallel to the (100) plane of the Ni substrate. This was observed for Al_2O_3 films obtained by oxidation of Ni_3Al [13, 113]. It is also possible that the oxygen ions form a hcp sublattice as for α-Al_2O_3 , and the (0001) plane is parallel to the (100) plane of the Ni(100) substrate. However, α-Al_2O_3 is known to exhibit only two dipole active modes in EELS and IR (see [67] and Tab. 4.4 in chapter 4). Since in the EEL spectrum after annealing to 1400 K in Fig. 5.25, which corresponds to the LEED pattern in Fig. 5.26, three dipole active modes are observed, the existence of α-Al_2O_3 has to be ruled out. As for the oxidation of the Ni_3Al/Ni(100) system in sections 5.2 and 5.3 the existence of the γ'-Al_2O_3 phase is concluded.

In this chapter different methods to grow thin alumina films on Ni(100) were discussed. It was shown, that by oxidation and annealing of the system Ni_3Al/Ni(100) a well ordered film of γ'-Al_2O_3 can be grown. However, during annealing of the initially deposited Al layer to form the Ni_3Al layer some Al is lost, that diffuses into the bulk of the Ni(100) substrate. A second way to grow a well ordered alumina film on Ni(100) is to deposit Al in an oxygen atmosphere. The partial pressure of oxygen has to be adjusted according to the deposition rate of Al. Here the thickness of the alumina layer is approximately double of that of the nominally deposited Al layer, and thus a desired film thickness can be realized. Annealing of the oxide leads to the formation of γ'-Al_2O_3, which is stable for annealing temperatures up to ~ 1350 K.

In the next chapter the growth of cobalt on Al_2O_3 is investigated. The growth of metals on oxides is also important for various fields and especially for the fabrication of MTJs.

Chapter 6

Growth of Cobalt on Al_2O_3/Ni(100)

In aiming at single crystalline TMR junctions, not only the growth of well ordered oxide films on ferromagnetic metals is important, but also the growth of ferromagnetic metals on well ordered oxides has to be studied. For MgO as a barrier epitaxial magnetic tunnel junctions were recently prepared by Bowen et al. [114] and by Wulfhekel et al. [115].

The growth of metal particles on oxides is also interesting for other fields of research, such as heterogeneous catalysis. Here, usually oxides like alumina or silica serve as substrates and a catalytically active material, e.g., a transition metal, is deposited on it.

The structure, morphology, electronic structure, and adsorption behavior of metal deposits on well ordered oxide (Al_2O_3) films have been reviewed by Bäumer and Freund [47], covering rhodium, palladium, cobalt, platinum, and vanadium deposits. More recent studies deal with cobalt on γ'-Al_2O_3 [116], rhodium on γ-Al_2O_3 and on α-Al_2O_3 [117], silver on well ordered alumina [118], copper and vanadium on Al_2O_3/Ni_3Al(111) [119], and copper and palladium on α-Al_2O_3 [120]. Cobalt is known to grow crystalline on well ordered Ga_2O_3 films at room temperature. In this way Jeliazova [22] prepared a crystalline TMR junction consisting of Co/Ga_2O_3/Ni(100). This system is thermally stable up to 1000 K.

The study in this section is similar to that of Costina [11] and Podgursky et al. [116]. In these studies a bulk Ni_3Al(100) single crystal was oxidized at 1100 K and Co was deposited at room temperature on the grown alumina film. It was observed that Co grows in clusters, and after deposition of a nominal thickness of 30 Å the diameter distribution of the clusters has a maximum at $\sim$85 Å, and the clusters show a roughness of $\sim$10 Å.

In this work the Al_2O_3 film was grown via the Ni_3Al(100)/Ni(100) system. This system was prepared by depositing a 12 Å thick aluminum layer on the

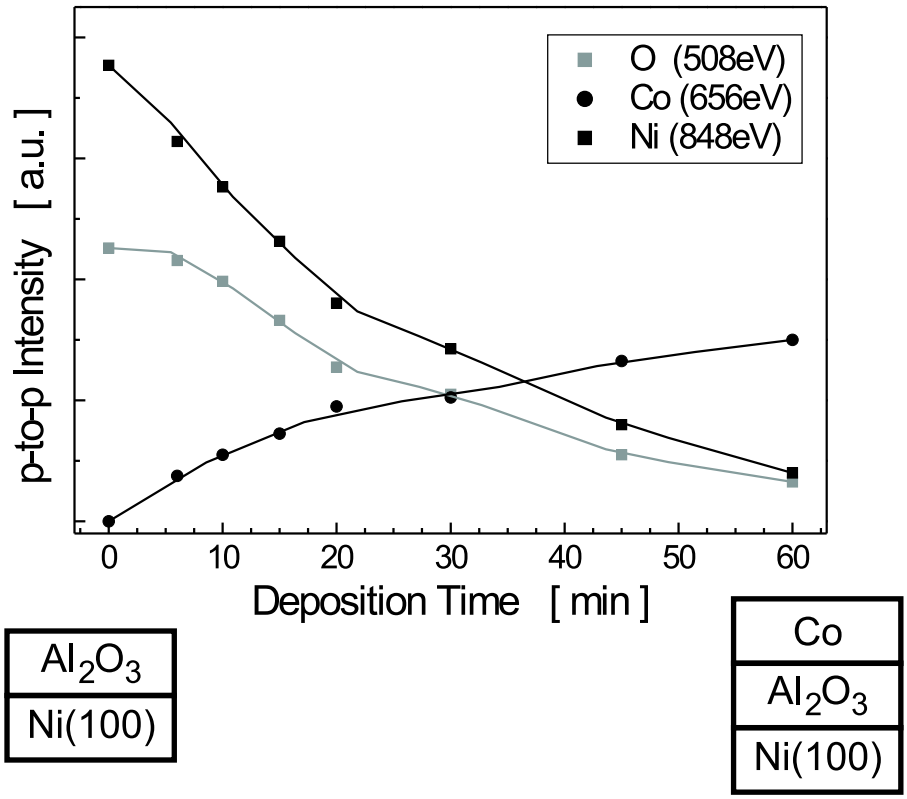

Figure 6.1: *AES peak-to-peak intensities of the oxygen transition at 503 eV, the cobalt transition at 656 eV, and the nickel transition at 848 eV.*

Ni(100) substrate and annealing to 900 K for four minutes. The film was then oxidized at 800 K to saturation and afterwards annealed to 1300 K. In such a way a γ'-Al_2O_3 film was prepared on Ni(100).

On this Al_2O_3 film cobalt was deposited by thermal evaporation from a cobalt rod with a deposition rate of 0.24 Å/min. The peak-to-peak intensities of the oxygen KLL transition at 503 eV, the cobalt LMM transition at 656 eV, and the nickel LMM transition at 848 eV are shown in Fig. 6.1 as a function of the deposition time. Since the cobalt LMM transition at 716 eV overlaps with the Ni LMM transition at 716 eV, and the cobalt LMM transition at 775 eV overlaps with the Ni LMM transition at 783 eV, the non overlapping transitions shown in Fig. 6.1 are analyzed. The cobalt signal increases and after 60 minutes a saturation is not reached, because the thickness of the layer (14.4 Å) is comparable to the mean free path of the electrons ($\sim$14 Å). The thickness of 14.4 Å results from the deposition rate of 0.24 Å/min and the deposition time of 60 min, and is thus the nominal thickness. The effective thickness, which is determined from the attenuation of

the AES signal of oxygen at 503 eV, amounts to ~ 14.1 Å. Although for this Co coverage the agreement is good, for lower coverages considerable deviations occur: For a deposition time of 6 min the nominal thickness is $d_{\mathrm{nom}}(6\,\mathrm{min}) = 1.44$ Å and the effective thickness is $d_{\mathrm{eff}}(6\,\mathrm{min}) \approx 0.82$ Å. For a deposition time of 15 min one obtains $d_{\mathrm{nom}}(15\,\mathrm{min}) = 3.6$ Å and $d_{\mathrm{eff}}(15\,\mathrm{min}) \approx 2.74$ Å. The differences can be explained by the growth mode of Co on Al_2O_3. Costina [11] found in STM studies that Co grows on Al_2O_3 in three-dimensional clusters (Volmer-Weber growth mode) and not layer by layer. Thus the assumption of a layer by layer growth that is made in the determination of the film thickness from the attenuation of the AES signal is not valid, and the nominal thicknesses are considered in the following.

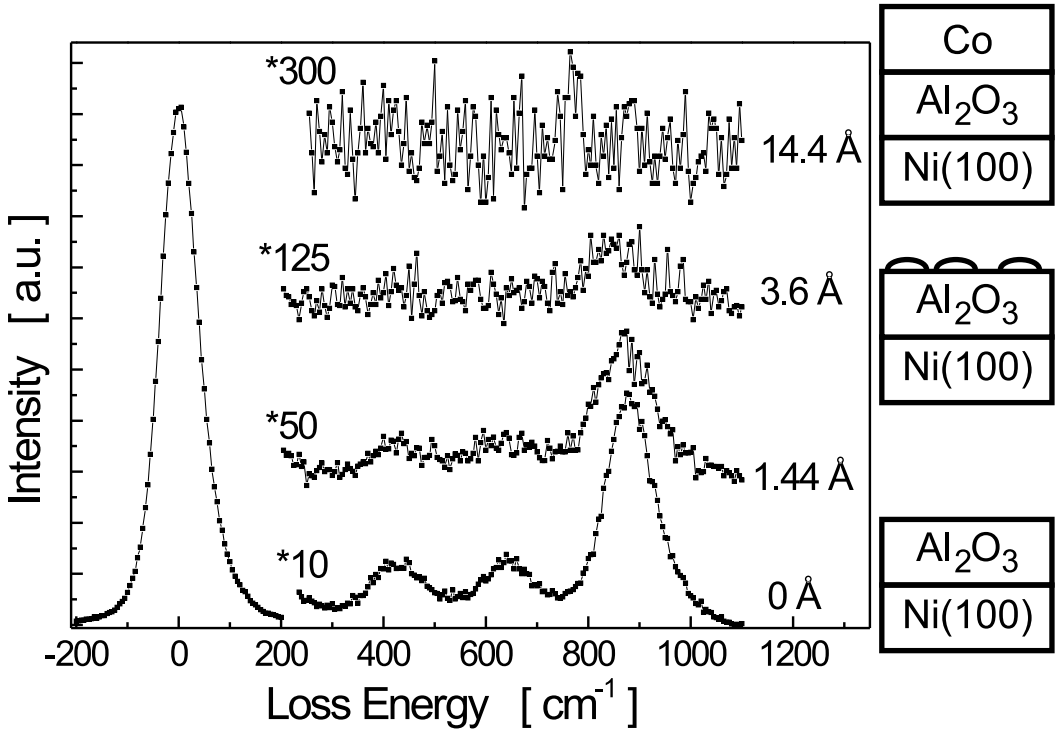

Figure 6.2: *EEL spectra for different nominal thicknesses of the Co layer deposited on alumina.*

The vibrational properties of the oxide film during Co deposition were investigated by EELS. Fig. 6.2 shows EEL spectra of the system $Co/Al_2O_3/Ni(100)$ as a function of the nominal thickness of the cobalt film. The spectrum of the uncovered oxide film is shown in the bottom and closely resembles the one in Fig. 5.13 with losses at 420, 630, and 880 cm^{-1}, which are the characteristic Fuchs-Kliewer

phonons of Al_2O_3. The film was in section 5.3 identified as $\gamma'Al_2O_3$. For a nominal Co coverage of 1.44 Å ($d_{\text{eff}} \approx 0.82$ Å) all three losses are still observed, but with a reduced intensity. At a Co coverage of nominally 3.6 Å ($d_{\text{eff}} \approx 2.74$ Å) two losses are resolved, which means that even at this coverage the dipole moments of the oxide are not completely screened. This is in accordance with the findings of Costina [11], that cobalt undergoes a cluster-like growth on alumina, because for a layer-by-layer growth mode the coverage of 3.6 Å corresponds to more than one monolayer of fcc Co. At a coverage of 14.4 Å ($d_{\text{eff}} \approx 14.1$ Å) no losses are observed, which means that the dipole moments of the oxide are completely screened due to the metallic behavior of the cobalt film.

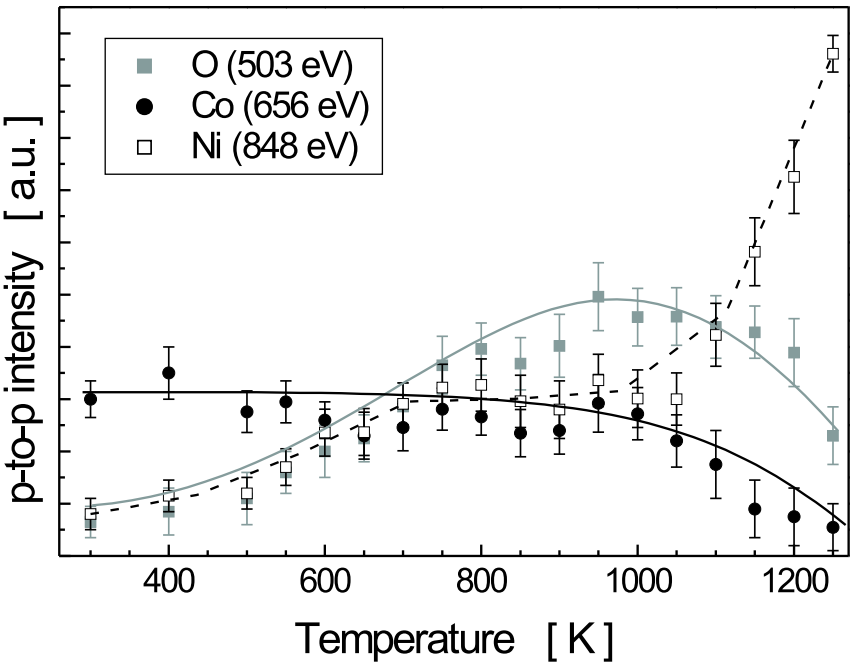

Figure 6.3: *AES peak-to-peak intensities of the corresponding transitions to Fig. 6.1 as a function of the annealing temperature.*

The AES peak-to-peak intensities of the oxygen KLL transition at 503 eV, the Co LMM transition at 656 eV, and the LMM transition of Ni at 848 eV are shown in Fig. 6.3 as a function of the annealing temperature. The cobalt signal is approximately constant up to 1000 K. At temperatures above 1000 K the Co signal decreases, which is due to diffusion of Co through the oxide into the substrate. A migration of metals into oxides in the temperature range 500 –

900 K was reported by Heemeier et al. [121]. Costina [11] observed that Co grows on alumina in three-dimensional clusters at room temperature. Upon annealing to 700 K a coalescence of the clusters is observed, and the diffusion of Co through the oxide into the substrate sets in.

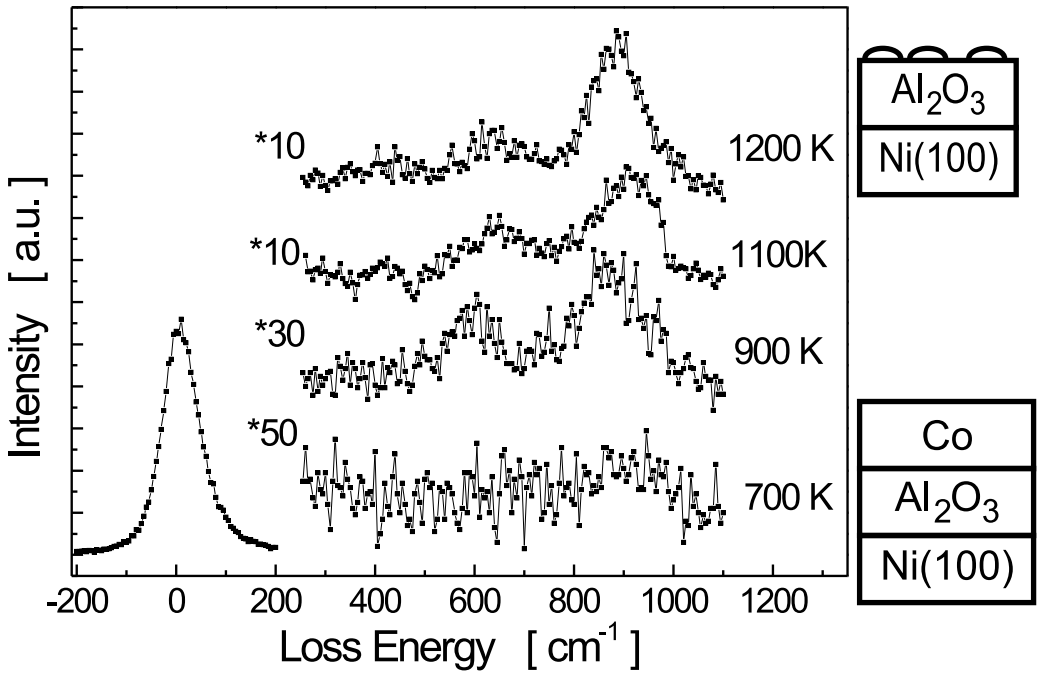

Figure 6.4: *EEL spectra for different annealing temperatures of the system $Co/Al_2O_3/Ni(100)$. After annealing to 1200 K three loss features at 420, 630, and 880 cm^{-1} are observed. The spectra were recorded at room temperature.*

In Fig. 6.4 EEL spectra taken during annealing of the system $Co/Al_2O_3/Ni(100)$ are shown. After annealing to 700 K a very broad loss at 900 cm^{-1} is observed. This means that at this temperature the dipole moments of the oxide are not completely screened by the cobalt film anymore. At 900 K the losses at 630 and 880 cm^{-1} are clearly resolved. This suggests that areas free of Co are present at the surface. This is in agreement with the increase of the AES signal of oxygen between 300 and 900 K in Fig. 6.3. Since the Co signal does not change significantly in the temperature range 300 – 1000 K, it appears likely that the areas free of Co on the surface are a consequence of a coalescence of Co clusters. Only for the temperature range 1000 – 1250 K the Co signal decreases, due to diffusion of Co through the oxide into the substrate.

This is also evidenced by the increase of the Ni signal in the temperature range 1000 – 1250 K.

After annealing at 1100 K all three losses in the EEL spectrum in Fig. 6.4 reappeared, however, with slightly different relative intensities compared to the spectra before the cobalt deposition. After deposition and annealing of the Co the intensity of the elastic beam is reduced compared to that of the oxide film before the cobalt deposition. Maybe the oxide film is not so well-ordered and smooth as before, and therefore the intensity of the elastic beam is reduced. The FWHM, however, is not changed significantly: 77.7 cm^{-1} before deposition and 75.8 cm^{-1} after annealing of the $Co/Al_2O_3/Ni(100)$ system to 1200 K.

In the previous chapter the oxide film was shown in the previous chapter to be stable up to 1200 K. Above 1200 K the oxygen signal is strongly diminished, which is due to decomposition and desorption of the oxide film from the Ni(100) substrate. In the case of $Co/Al_2O_3/Ni(100)$ it seems that the oxide decomposes at a somewhat lower temperature.

A LEED pattern of the cobalt film is not observed at any annealing temperature and, hence, no crystalline film of cobalt is grown on the alumina film. This is at variance to $Ga_2O_3/Ni(100)$, where crystalline TMR junctions of $Co/Ga_2O_3/Ni(100)$ were achieved by Jeliazova [22].

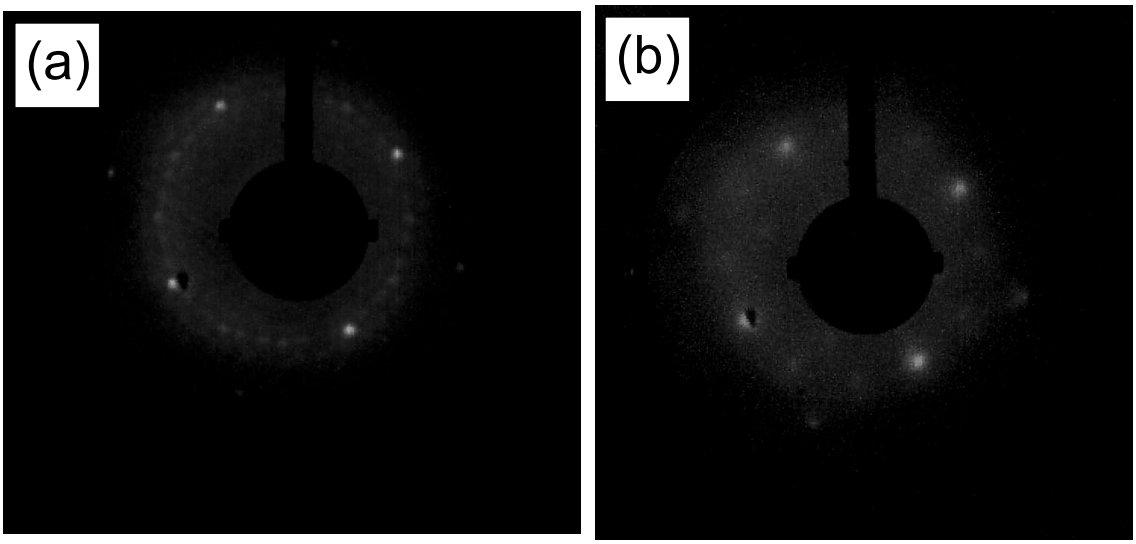

Figure 6.5: *LEED images of the Al_2O_3 film after annealing to 1300 K (a), and of the system $Co/Al_2O_3/Ni(100)$ after annealing 1000 K (b). The primary energy was 122 eV for both of the images.*

After annealing to 1300 K the alumina film prepared by oxidation of the

$Ni_3Al/Ni(100)$ system at 800 K produces the LEED pattern which is shown in Fig. 6.5(a). This LEED pattern was discussed in section 5.3 and interpreted in terms of a γ'–Al_2O_3 film, which grows in 6 domains with hexagonal surface structure. After deposition of 14.4 Å Co and annealing the system to 1000 K the LEED pattern shown in Fig. 6.5(b) is observed. This pattern consists of a twelve-fold ring structure with very weak intensity as observed previously in sections 5.2 and 5.5. It is evidenced from EELS data that areas free of Co are present at the surface. Thus it is likely that the LEED pattern stems from Co free areas, this means oxide surfaces, a result which was suggested by the EELS measurements. Since, except with respect to the number of domains, the LEED pattern has not changed, and also the loss features in the EEL spectra are only changed in intensity with respect to the oxide film before deposition of Co, the Al_2O_3 film is still in the γ'-phase.

Chapter 7

The Growth of Al_2O_3 on Co(0001)

In the preceding chapter the growth of cobalt on a thin alumina film was investigated. In contrast to the growth of Co on well ordered Ga_2O_3 [22] the growth of Co on Al_2O_3 did not exhibit a crystalline structure. The growth of Al_2O_3 on a crystalline cobalt substrate is also interesting, because cobalt is often used as electrode in TMR devices [122, 123, 124]. Other areas of interest for thin metal oxide films are, e.g., catalysis [75, 76] and microelectronics [77, 78].

Whereas the phase diagram of the Ni–Al alloys is very well known for a long time (see chapter 4), the phase diagram of the Co–Al alloys is still subject to research [125]. No study of the alloying of Al deposited on a Co single crystal seems to be available. About intermixing of Al deposited on a cobalt film was reported by Egelhoff et al. [126]. Shivaparan et al. [127] found intermixing of Co and Al during the deposition of Co on Al(001) and Al(110) at room temperature. The formation of CoAl and Co_2Al_5 by mechanical alloying and leaching was investigated by Golubkova et al. [128].

For intermetallic alloys containing nickel and aluminum numerous studies of the oxidation at room temperature as well as at elevated temperatures exist and were cited in chapter 5. For alloys containing cobalt and aluminum only the room temperature oxidation of the CoAl(100) surface was studied [87]. Upon oxidation of the CoAl(100) surface at room temperature, oxygen is chemisorbed for oxygen exposures $\leq 0.2\,\mathrm{L}$. At higher exposures a thin film of amorphous Al_2O_3 is formed.

In this chapter the growth of thin films of Al_2O_3 on the Co(0001) surface is discussed. Cobalt crystallizes in the hexagonally close packed structure with lattice constants of a = 2.51 Å and b = 4.07 Å. Although no examples of ordered alumina films grown on Co–Al alloys exist, alloying of Al and Co was investigated by deposition and annealing of an Al film on the Co(0001) substrate. This experiment is presented and discussed in section 7.1. The alloy that forms

has a hexagonal surface structure and does not correspond to one of the known bulk alloys of CoAl. It will thus be referred to as Co_xAl_y. The oxidation of the Co_xAl_y/Co(0001) system at room temperature is presented in section 7.2. In section 7.3 the deposition and subsequent oxidation of an aluminum film on Co(0001) is discussed. The result is an ordered alumina film. Section 7.4 deals with the deposition of Al on Co(0001) in oxygen atmosphere at room temperature. By annealing the oxide is ordered and no evidence for intermixing of Al and Co is found.

7.1 Alloying of Al on Co(0001)

In this study a nominal amount of 6 Å Al is deposited on a Co(0001) surface. However, the effective thickness of the Al layer determined from the attenuation of the Co AES signal after deposition is $d_{eff} = 7.8$ Å. The deposition proceeds by evaporation of Al from a pestled crystal of NiAl as described in chapter 2. The film is then annealed to 1000 K in steps of 100 K. Each annealing step lasted for two minutes and the sample is cooled to room temperature before measurements are performed. AES spectra in the energy range 20 – 120 eV are shown in Fig. 7.1. Spectrum (a) is for the clean Co(0001) surface and accordingly the MNN transitions of Co at 53 and 95 eV are observed [33]. After deposition of 7.8 Å of aluminum spectrum (b) shows only the LMM transition of aluminum at 68 eV. No hints of cobalt are present in this spectrum, because of the small mean free path of electrons in the aluminum film in this energy range ($\lambda_{Al}(50\,eV) = 3.2$ Å and $\lambda_{Al}(100\,eV) = 4.2$ Å [34]). The Al film on Co(0001) was then annealed and spectrum (c) is taken after annealing to 800 K. The intensity of the Al LMM transition at 68 eV is slightly diminished and at 53 eV the Co MNN transition reemerged.

The AES transitions in the energy range 20 – 120 eV of Fig. 7.1 are only sensitive to the topmost layers of the film. To gain information about the interdiffusion of cobalt and aluminum transitions of higher energy must be regarded. In Fig. 7.2 the ratio of the peak-to-peak intensities of the Al KLL transition at 1396 eV and the Co LMM transition at 656 eV is shown. Within the experimental error the ratio decreases over the complete temperature range. This is due to intermixing of Al and Co. Since a LEED pattern is observed after annealing to 400 K (Fig. 7.3(b)) intermixing of Al and Co takes place at temperatures slightly above room temperature and maybe at room temperature as found by Shivaparan et al. [127]. At annealing temperatures above 1000 K the Al signal is close to zero due to complete diffusion of the Al into the bulk of the substrate.

For the CoAl alloy that has formed a determination of its thickness from the attenuation of the AES signal of the Co(0001) substrate is not possible, because

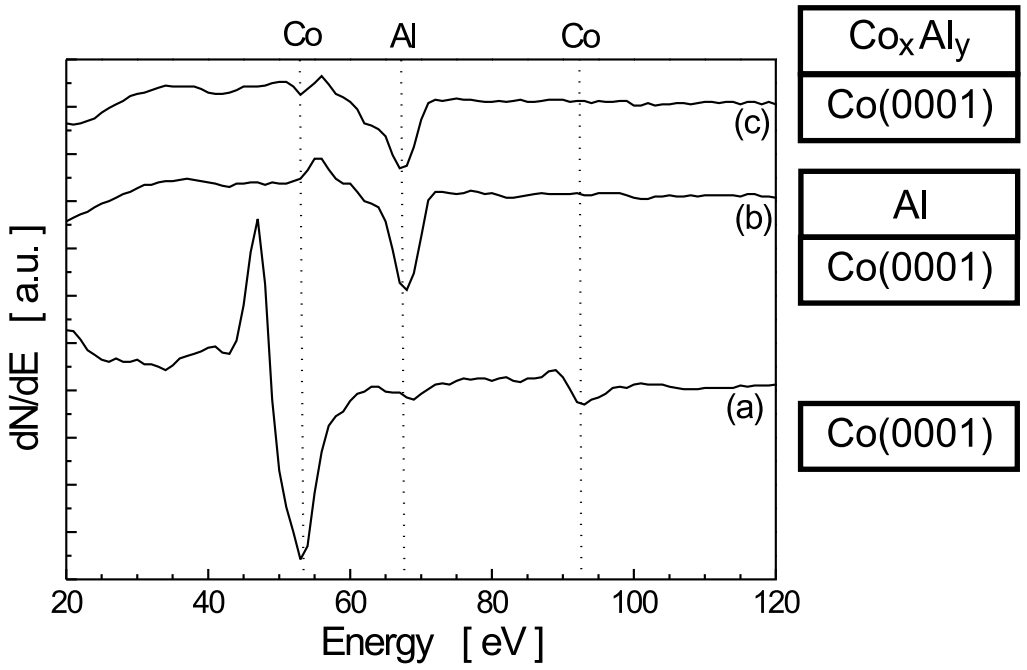

Figure 7.1: *AES spectra of the clean Co(0001) surface (a), after deposition of 6 Å Al (b), and after annealing the system Al/Co(0001) to 800 K.*

the Co AES signal of the Co_xAl_y film contributes to the Co AES signal of the Co substrate.

After annealing to 800 K the ratio of the peak-to-peak intensities of the AES signals is $Al_{1396}/Co_{656} \approx 0.6$. Using the relative AES sensitivity factors of Al and of Co ($s_{Al} = 0.085$, $s_{Co} = 0.25$ [30]) results in a ratio of Al/Co = 1.76. However, this determination is inaccurate, because the AES signal of the Co substrate contributes to the Co AES signal of the alloy.

To investigate the structural properties of the film LEED studies were performed. Fig. 7.3 (a) shows a LEED image of the clean Co(0001) surface displaying a hexagonal structure. After deposition of the 7.8 Å thick Al film at room temperature, the LEED image is diffuse. After annealing the film to 400 K for 2 minutes, however, a LEED pattern with low intensity is observed, which is shown in Fig. 7.3 (b). This suggests that interdiffusion and alloying takes place already at this temperature, which supports the conclusion drawn from the AES data of Fig. 7.2. The structure itself has a hexagonal unit cell with a two-dimensional lattice constant of 5.02 ± 0.15 Å. The hexagonal LEED pattern with a lattice constant of 5.02 Å can be explained by a p(2x2) structure with respect to the

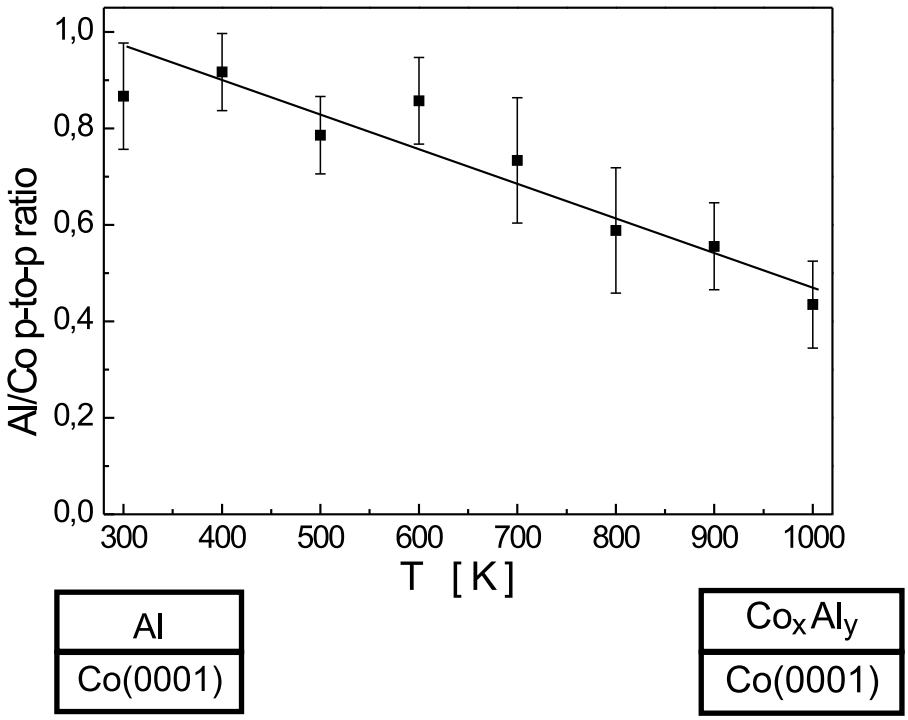

Figure 7.2: *AES peak-to-peak ratio of Al_{1396}/Co_{656} during annealing of the system Al/Co(0001). The schematic on the left and on the right show the film before and after annealing, respectively.*

Co(0001) surface.

Two explanations are possible for the hexagonal surface structure. The surface structure could be the (0001) plane of an alloy that displays a hexagonal close packing. The only alloy of CoAl that displays hexagonal close packing in its bulk phase is Co_2Al_5. However, the lattice constants of Co_2Al_5 are a = 7.67 Å and b = 7.61 Å. The difference to the two-dimensional lattice constant of $a = 5.02 \pm 0.15$ Å determined from the LEED pattern is large and hence the formation of Co_2Al_5 must be ruled out.

The hexagonal surface structure could also be explained in terms of the (111) plane of a cubic Co–Al alloy. The only cubic alloy is CoAl with a lattice constant of 2.86 Å. The lattice constant of the (111) plane of CoAl thus amounts to 4.04 Å which also does not match the two-dimensional lattice constant of 5.02 ± 0.15 Å of the alloy that has formed. Thus, none of the bulk Co–Al alloys that are listed in Table 4.2 is formed. The alloy that is formed is therefore referred to as Co_xAl_y.

After annealing to 800 K the LEED image in Fig. 7.3(c) shows additional spots of the p(2x2) structure. Also, the intensity of the spots is increased in comparison

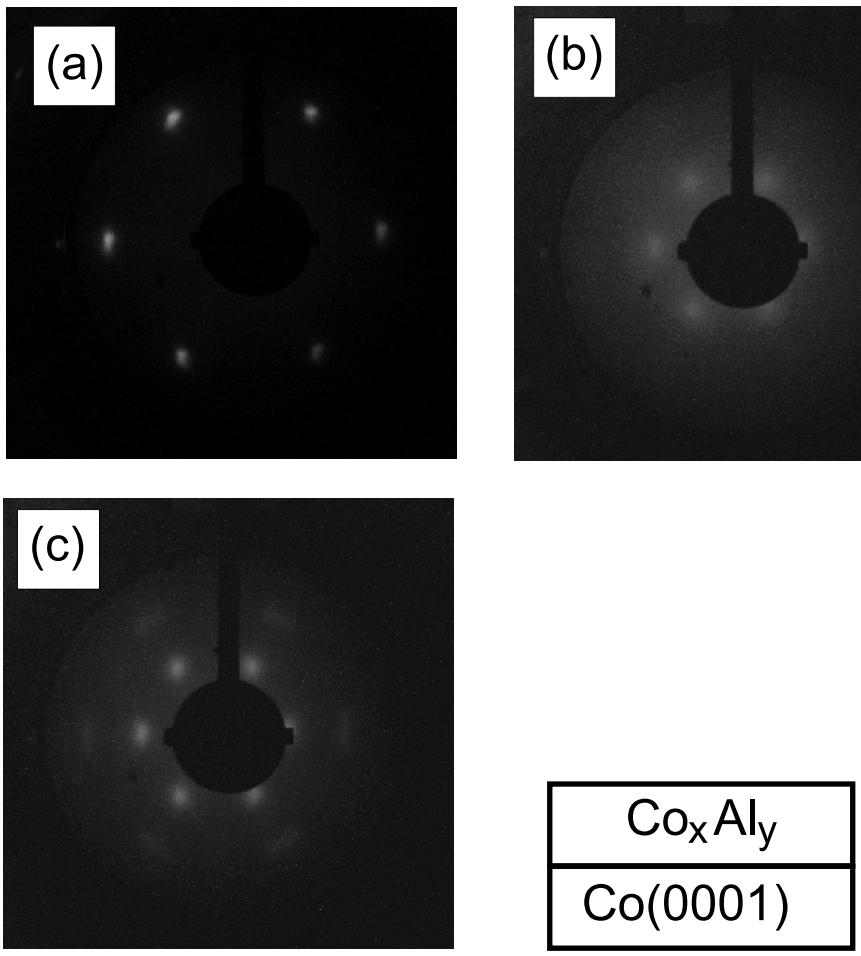

Figure 7.3: *LEED images of (a) the clean Co(0001) surface, (b) the system Al/Co(0001) annealed to 400 K, and (c) the system Al/Co(0001) annealed to 800 K. The primary energy was 96 eV for all images.*

to those of Fig. 7.3(b).

The EEL spectrum of the clean CoAl(100) surface exhibits a loss at $\sim 230\,\mathrm{cm}^{-1}$, which can be assigned to a quasi-transverse optical mode arising from the vibration of Al atoms perpendicular to the surface. This observation was made by Rose et al. [87] and interpreted as a hint for Al atoms in the topmost layer. No such loss was observed in the EEL spectrum of the Co_xAl_y alloy, but since no further data upon the composition of the topmost layer are available, the presence of Al in that layer remains unclear.

Summarizing, upon deposition and annealing of a 7.8 Å thick Al film on Co(0001), the alloy Co_xAl_y is formed. Alloying starts at 400 K and, after annealing to 800 K a coexistence of areas covered by the Co_xAl_y alloy and areas of

clean Co is observed. After annealing to 1100 K the alloy is decomposed, and the Al is diffused into the substrate or desorbed from the surface.

7.2 Oxidation of the Co_xAl_y/Co(0001) system

In aiming at a thin ordered aluminum oxide film on the Co(0001) surface, the system Co_xAl_y/Co(0001) system was oxidized with O_2^{16} at room temperature. The Co_xAl_y/Co(0001) system was prepared by deposition and annealing of 7.8 Å Al on Co(0001) as described in the previous section.

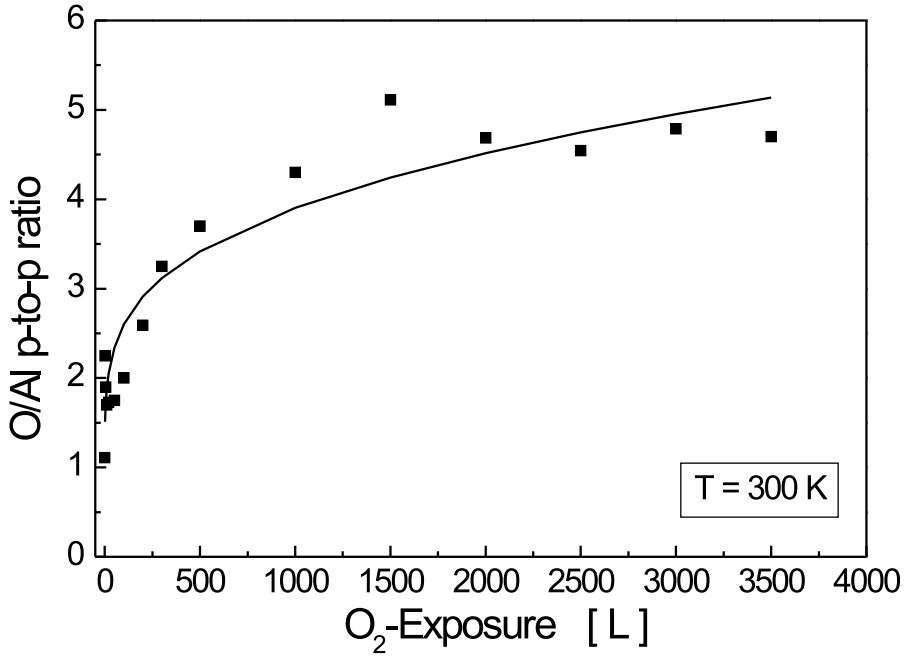

Figure 7.4: *Peak-to-peak ratio of O_{503}/Al_{1396} during room temperature oxidation of the Co_xAl_y / Co(0001) system.*

Fig. 7.4 shows the peak-to-peak ratio of O_{503}/Al_{1396} during the oxidation process. The ratio increases up to an exposure of 1500 L, and above 2500 L a saturation level is reached. The saturation value of the O/Al ratio is ~ 4.8, and is thus lower than the value of 6.2 expected for bulk Al_2O_3 [33]. The ratio was fitted with the logarithmic growth law of equation (5.1). This growth law is characteristic for the low temperature oxidation of metals [106].

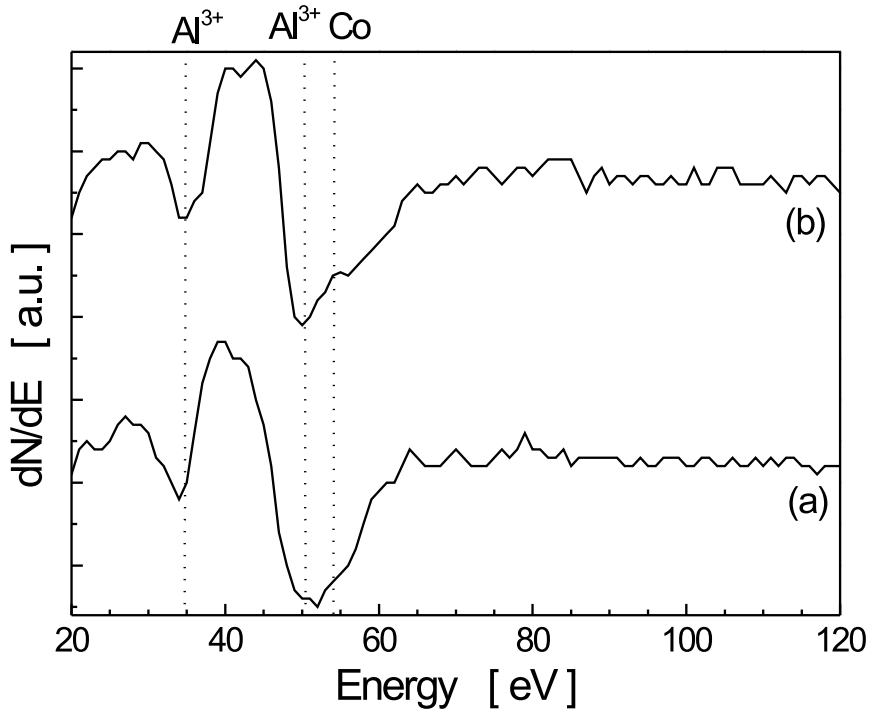

Figure 7.5: *AES spectra after oxidation of the $Co_x Al_y$/Co(0001) system to 3500 L at room temperature (a) and after annealing of the oxidized system to 1100 K (b).*

An AES spectrum of the oxidized film is shown in Fig. 7.5(a). In this spectrum transitions at 35 and 51 eV are observed, which are the LMM transitions of Al^{3+}. Accordingly, upon oxidation of the Co_xAl_y/Co(0001) system the Al atoms react with oxygen to form Al_2O_3. Whereas for the oxidation of NiAl [9], Ni_3Al [13], and FeAl [88] UPS investigations show that only Al atoms are involved in the oxidation process, no such data are available for the oxidation of alloys of CoAl. If there is less than 1% of a monolayer of CoO or Co_3O_4 it cannot be detected by AES [31]. However, the heat of formation favors the oxidation of Al atoms over the oxidation of Co atoms: The heats of formation are ΔH_f=-1676 kJ/mol for Al_2O_3, ΔH_f=-238 kJ/mol for CoO, and ΔH_f=-891 kJ/mol for Co_3O_4 [129]. Spectrum (b) of Fig. 7.5 was recorded after annealing the film to 1100 K. The LMM transitions of Al^{3+} at 35, 43, and 51 eV are observed. The transition of Al^{3+} at 51 eV overlaps with the MNN transition of Co at 53 eV. Hence, it is likely that Co is present in the topmost layers of the film.

Under the assumption that a pure Al_2O_3 film is grown on the Co(0001) surface

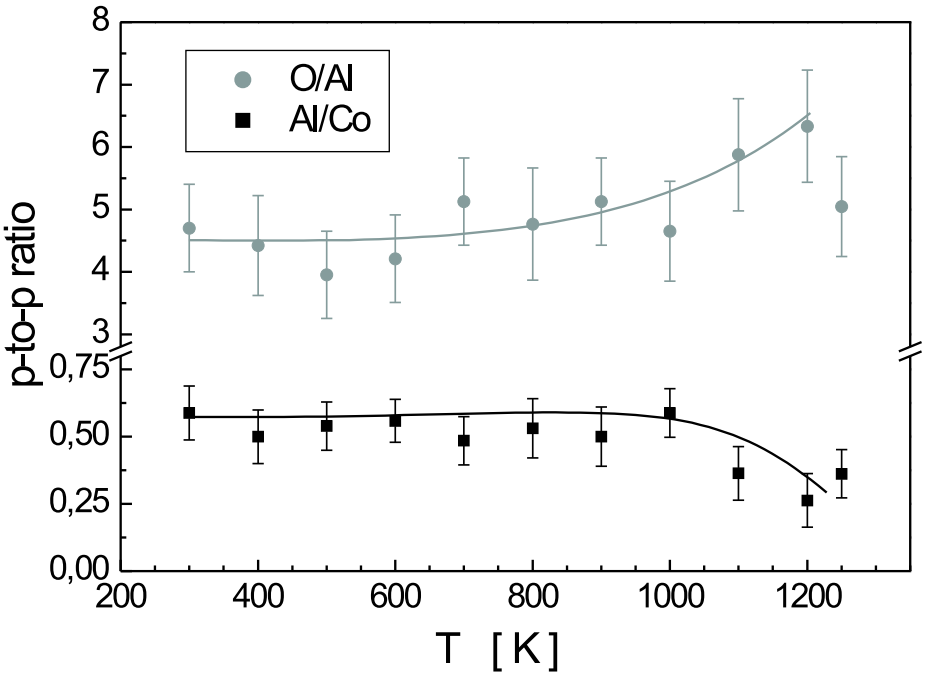

Figure 7.6: *Peak-to-peak ratios of O_{503}/Al_{1396} and Al_{1396}/Co_{656} as a function of the annealing temperature for the oxidized Co_xAl_y/Co(0001) system.*

without an interface layer, the thickness of the layer can be estimated from the attenuation of the AES signal of the cobalt substrate by equation (3.4). This results in a thickness after oxidation of (11.5 ± 2) Å. The thickness is much larger than that found by Rose et al. [87] for the room temperature oxidation of the CoAl(100) surface (7.1 Å). For the case of the oxidation of Ni_3Al/Ni(100) it was also found that the room temperature oxidation of this system generates a thicker oxide layer (11 ± 2 Å) than the oxidation of the bulk Ni_3Al(100) surface (Costina [11] found a thickness of about 5 Å). From the available data no reason for this behavior can be given. Upon oxidation of a pure Al film the thickness of the film is known to double [107]. Thus it seems that some of the deposited Al (7.8 Å) is not oxidized. Maybe some Al is lost due to diffusion into the substrate or desorption from the surface.

The oxidation of exclusively aluminum proceeds by the process of preferential segregation oxidation: adsorption of oxygen induces the segregation of Al atoms to the surface, where by the reaction of the Al atoms with the adsorbed oxygen an aluminum oxide film is formed [81]. If there was a diffusion of oxygen into

the film, a mixed oxide $CoAlO_x$ would be formed. It can be speculated that the mobility of the Al atoms is larger in the surface alloys than in bulk alloys and therefore thicker oxide films can be grown for the surface alloys, but no reliable evidence for this claim can be extracted from the presented data.

The oxidized system Co_xAl_y/Co(0001) is then annealed to 1200 K in steps of 100 K and afterwards to 1250 K. Again, each annealing step lasted two minutes and the sample was cooled to room temperature before performing measurements. The peak-to-peak ratio of Al_{1396}/Co_{656} is shown in Fig. 7.6 and is constant upon annealing to 1000 K. Only for annealing temperatures above 1000 K the ratio decreases. This is the temperature region where the Co_xAl_y alloy is decomposed. Thus a diffusion of Al into the cobalt substrate is likely at temperatures of 1100 K and above. The ratio O_{503}/Al_{1396} shown in Fig. 7.6 is, within the experimental error, also constant up to 1000 K, and only for 1100 and 1200 K the ratio is increased. Under the assumption that a pure alumina layer is formed on Co(0001) the thicknesses of the layer are:

- between 300 and 1000 K: $d_{300\,K} = (11.5 \pm 2)$ Å
- after annealing to 1100 K: $d_{1100\,K} = (9.6 \pm 2)$ Å
- after annealing to 1200 K: $d_{1200\,K} = (6.6 \pm 2)$ Å
- after annealing to 1250 K: $d_{1250\,K} = (4.6 \pm 2)$ Å

Between room temperature (300 K) and 1000 K the film thickness does not change. At annealing temperatures above 1000 K the thickness is strongly diminished. This is due to decomposition and desorption of the oxide layer.

The structural properties of the alumina film were investigated by EELS and LEED. EEL spectra of the oxide film for different annealing temperatures are shown in Fig. 7.7. After the room temperature oxidation the spectrum shows broad losses around 600 and 830 cm^{-1}. Since the LEED image is diffuse it is likely that at this stage the oxide is amorphous. The formation of an amorphous alumina layer upon room temperature oxidation is a common feature of many alloys of NiAl [81] and CoAl(100) [87]. After annealing to 500 K three losses at 430, 620, and 850 cm^{-1} are observed which are characteristic for phases of Al_2O_3 where the Al^{3+}-ions occupy octahedral and tetrahedral positions. For CoO grown on Co(0001) a loss at $\sim$565 cm^{-1} is characteristic [130], which is not observed in the spectra of Fig. 7.7. Upon annealing to temperatures above 500 K the intensity of the losses increases, which is reflected in the decrease of the magnification factor for the spectrum after annealing to 800 K. Also, the frequency of the losses is slightly shifted: The loss at 430 cm^{-1} shifts to 420 cm^{-1} and the loss at 850 cm^{-1} shifts to 890 cm^{-1}. However, these shifts have no significance concerning the

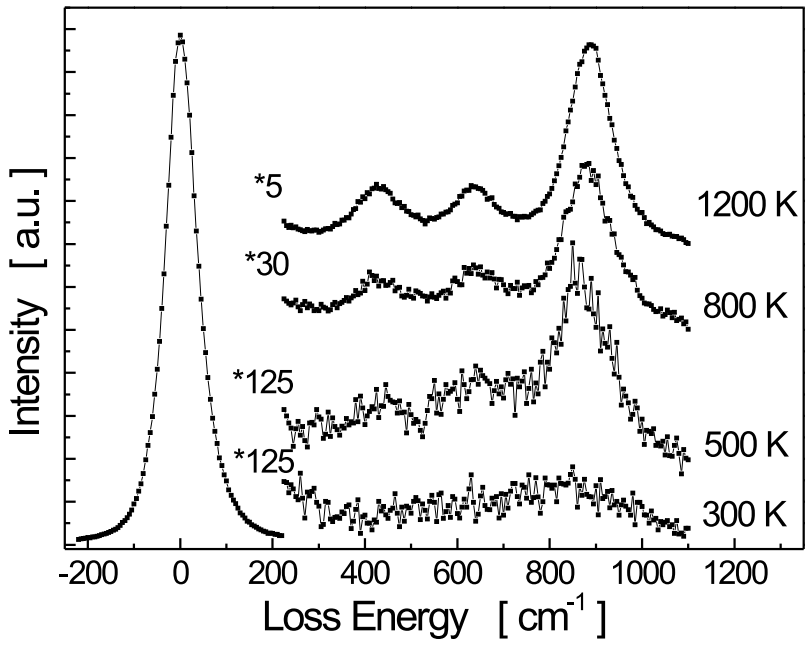

Figure 7.7: *EEL spectra of the oxidized Co_xAl_y/Co(0001) system for different annealing temperatures. The spectra were recorded at room temperature.*

phase of the Al_2O_3 that has formed. For the determination of the phase that has formed, LEED data have to be considered.

Fig. 7.8 shows a LEED image of the clean sample (a) in comparison to a LEED image of the oxide film after annealing to 1200 K (b). In Fig. 7.8(c) a schematic representation of the pattern in (b) is shown. The spots that are also observed for the clean Co(0001) surface are represented by dots, spots that arise from the alloy ontop of the cobalt substrate are indicated by crosses. These spots are also observed for the Co_xAl_y alloy in Fig. 7.3. The asterisks mark those spots that are due to the oxide. A hexagonal surface structure is observed and the unit mesh is indicated in the schematic representation in Fig. 7.8. The lattice constant is 5.02 ± 0.15 Å and is thus the same as that of the Co_xAl_y alloy. The existence of the α-Al_2O_3 phase, which has a hcp sublattice of oxygen ions and a lattice constant of a = 4.76 Å, can be ruled out, because it is known to exhibit two losses in EELS and not three. It is thus likely that the Co_xAl_y is oxidized and that upon annealing the Al_2O_3 film is ordered and adopts the surface structure of the Co_xAl_y alloy. It cannot be determined, whether there is an interface layer between the Al_2O_3 film and the Co(0001) substrate or areas of unoxidized Co_xAl_y.

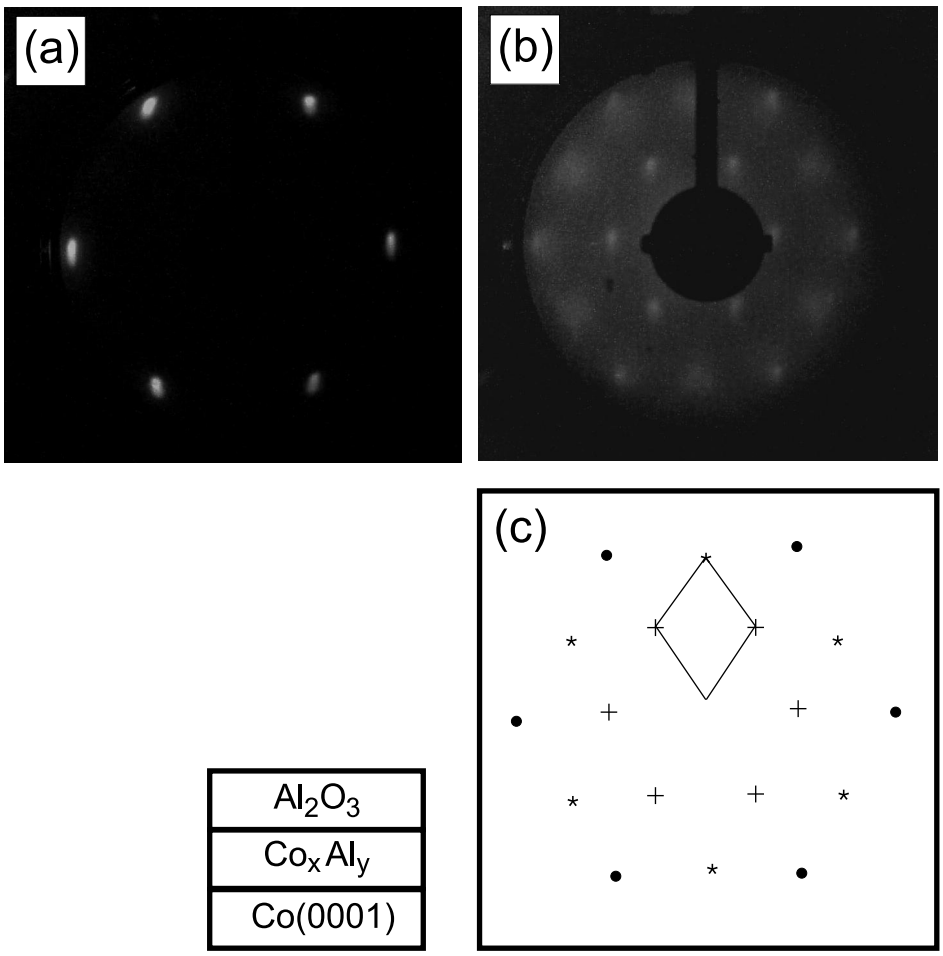

Figure 7.8: *LEED images (a) of the clean Co(0001) surface and (b) the oxidized Co_xAl_y/Co(0001) system annealed to 1200 K. The primary energy was 70 eV. A schematic representation of the image in (b) is shown in (c).*

7.3 Deposition and Oxidation of Al on Co(0001)

As for the Ni(100) substrate the deposition and oxidation of an aluminum film on the Co(0001) substrate at room temperature was studied. It is particularly interesting to study the structural properties of the oxide film, because of the structural differences of the Ni(100)and the Co(0001) substrate.

An Al film with an effective thickness of 14.6 Å determined from the attenuation of the AES signal of Co was deposited on the Co(0001) substrate at room temperature. AES spectra of the clean Co(0001) surface and the Al/Co(0001) system are shown in Fig. 7.9 (a) and (b), respectively. In spectrum (a) transitions at 53 and 95 eV are observed, which are the MNN transitions of cobalt [33]. After

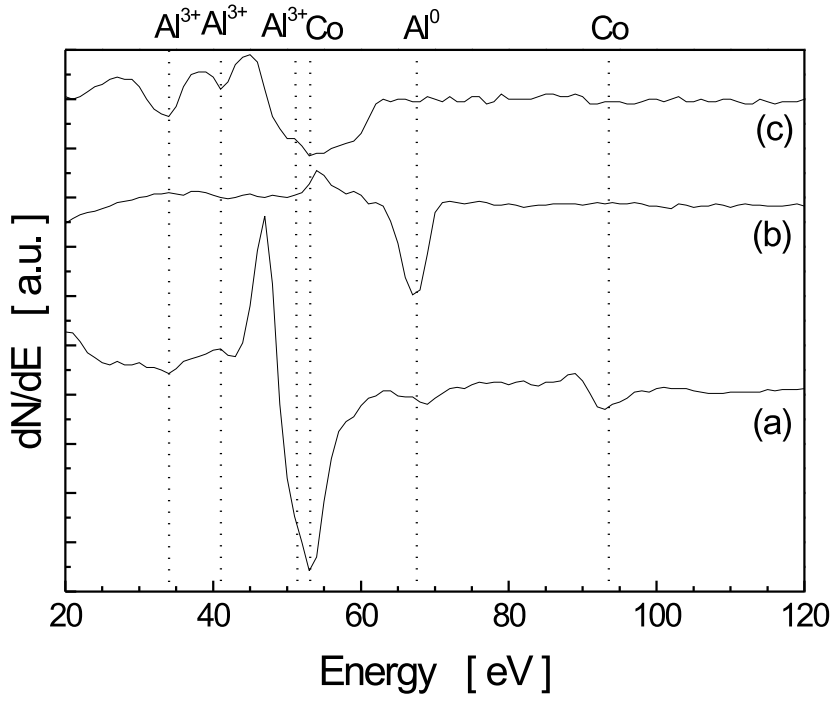

Figure 7.9: *AES spectra in the energy range between 20 and 120 eV of the clean Co(0001) surface (a), after deposition of 14.6 Å Al (b), and after oxidation of the Al film to saturation at 300 K (c).*

deposition of 14.6 Å of Al only the LMM transition of Al at 68 eV is observed [33]. After the Al deposition on Co(0001) the LEED image is diffuse.

The system Al/Co(0001) is then oxidized at room temperature up to a total exposure of 3000 L. In spectrum (c) of Fig. 7.9, taken after the oxidation, only the LMM transitions of Al^{3+} at 35, 43, and 51 eV are observed. The peak-to-peak ratio of the AES signal of oxygen at 503 eV (KLL transition) and of aluminum at 1396 eV (KLL transition) is shown in Fig. 7.10. After a steep increase of the O_{503}/Al_{1396} ratio for exposures below 200 L saturation is reached for exposures above 500 L. This is in contrast to the oxidation of the 12 Å Al/Ni(100) system at room temperature, where only for exposures above 1500 L a saturation was reached. Possible reasons for this difference are the different Al film thicknesses and maybe a structural difference of the Al film, but no conclusions can be drawn from the available data, because the LEED image of the Al film is diffuse and no STM data exist. Also for the oxidation of the Co_xAl_y/Co(0001) system a

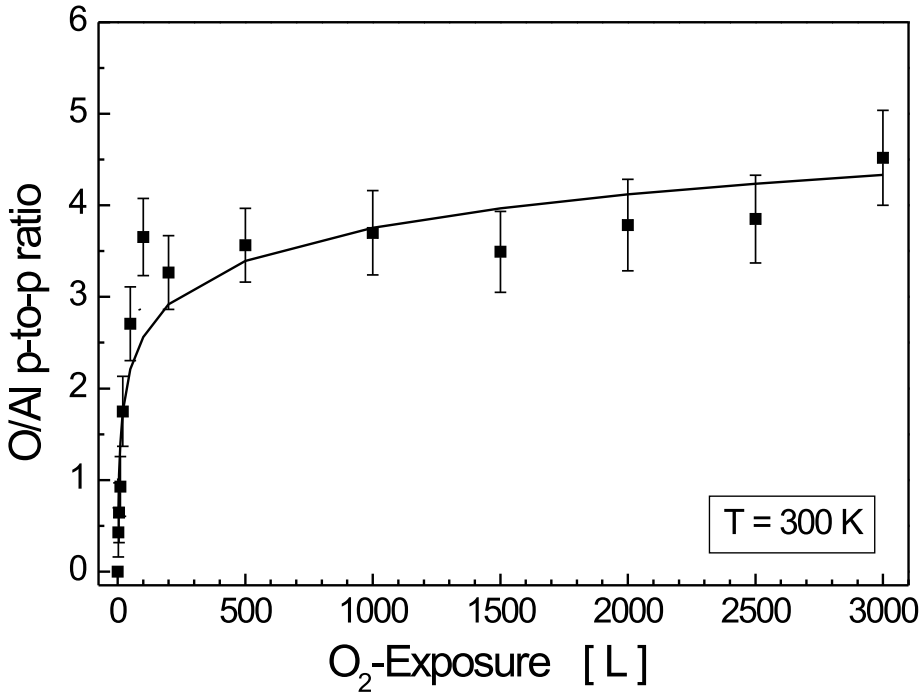

Figure 7.10: *O_{503}/Al_{1396} peak-to-peak ratio during oxidation of the 14.6 Å thick Al film on Co(0001) at room temperature.*

larger oxygen exposure (2500 L) was needed to reach the saturation level. The saturation value of the O_{503}/Al_{1396} ratio is ~ 3.8 and thus in fair agreement with the value of 3.5 obtained for the oxidation of the Al/Ni(100) system at 300 K. The divergence of this value from the value of bulk Al_2O_3 (6.2 from ref. [33]) can again be explained in terms of a coexistence of oxidized and unoxidized Al, which both contribute to the Al signal. The O/Al ratio in Fig. 7.10 was fitted by a logarithmic growth law after Cabrera and Mott [106], which is in good agreement with the data. This shows that the low temperature limit that is assumed for this growth law is fulfilled. The transition of Al^0 at 1396 eV and the transition of Al^{3+} were not separately, but a broadening of the transition during oxidation is observed. An EEL spectrum recorded after oxidation of the Al/Co(0001) system to saturation at 300 K is shown in Fig. 7.12. Two broad losses at about 640 and 880 cm^{-1} are observed. The observation of two losses in EELS is characteristic for amorphous Al_2O_3 or for α-Al_2O_3. Since the LEED image is diffuse, it is likely that the Al_2O_3 layer is amorphous.

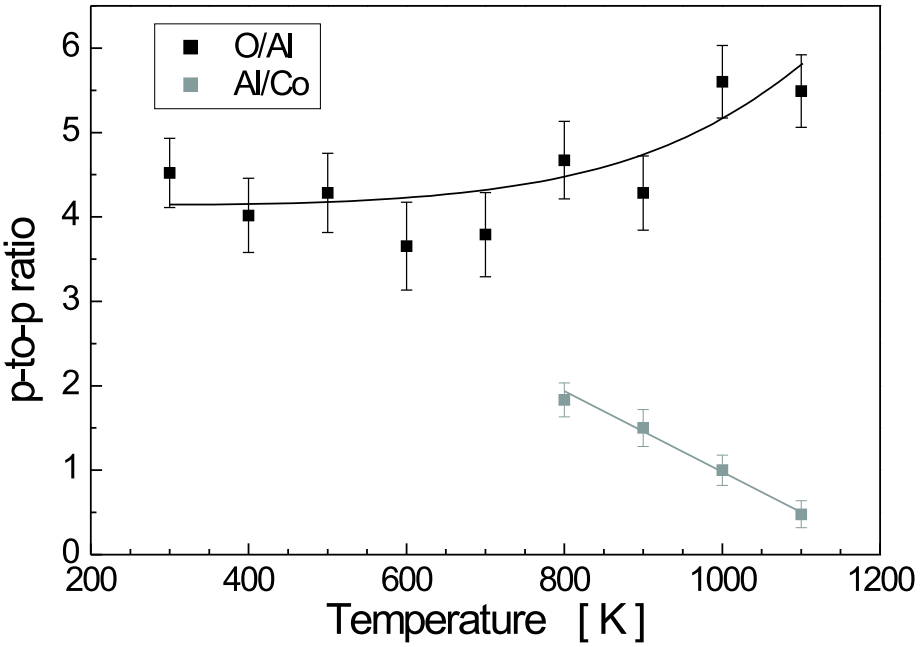

Figure 7.11: *Peak-to-peak ratio of O_{503}/Al_{1396} and Al_{1396}/Co_{656} for the oxidized Al/Co(0001) system as a function of the annealing temperature. The lines are a guide to the eye.*

The oxygen saturated Al/Co(0001) system is then annealed in steps of 100 K from room temperature to up 1100 K. In each annealing step the temperature was retained for two minutes and the sample was cooled to room temperature before performing measurements. Annealing to 1200 K results in complete desorption of the film. In Fig. 7.11 the ratios O_{503}/Al_{1396} and Al_{1396}/Co_{656} are shown as a function of the annealing temperature. After oxidation the Co AES signal at 656 eV is below the background level and reemerges after annealing to 800 K. The ratio O_{503}/Al_{1396} is constant at ~ 4 until annealing to 700 K and for higher temperatures it is slightly increased to ~ 5.5. The ratio Al_{1396}/Co_{656} decreases for temperatures above 800 K due to an increasing of the Co signal. This indicates interdiffusion of unoxidized Al and Co.

EEL spectra of the oxide film for different annealing temperatures are shown in Fig. 7.12(a). The spectrum taken after oxidation at 300 K exhibits two losses at about 640 and 880 cm^{-1}, which are characteristic for amorphous and α-Al_2O_3. After oxidation the LEED image is amorphous and the oxide film is probably amorphous. After annealing to 600 K three losses are observed at 400, 650 and 880 cm^{-1}. These losses are characteristic for Al_2O_3 phases, where the Al^{3+} ions occupy octahedral and tetrahedral positions in the oxygen sublattice. After an-

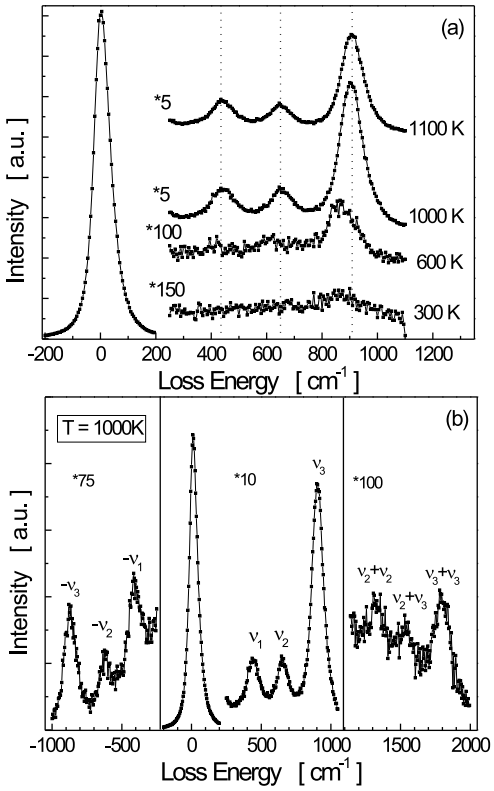

Figure 7.12: *EEL spectra of the oxidized Al/Co(0001) system for different annealing temperatures (a) and the spectrum after annealing to 1000 K showing also energy gains and multiple and combination losses(b). The positions of the energy losses are* $\nu_1 = 430\,cm^{-1}$, $\nu_2 = 640\,cm^{-1}$, *and* $\nu_3 = 905\,cm^{-1}$. *The spectra were recorded at room temperature.*

nealing to 1000 K the intensity of the losses is increased, which is reflected in the decrease of the magnification factor. The frequency of the losses is shifted: $400 \rightarrow 420$, $640 \rightarrow 650$ and $880 \rightarrow 905\,\mathrm{cm}^{-1}$. The spectrum after annealing to 1000 K is repeated in Fig. 7.12(b) in the middle section, and additionally energy gains as well as multiple and combination losses are shown. The spectrum taken after annealing to 1100 K, which is shown in Fig. 7.12(a), shows three losses at 420, 650 and $905\,\mathrm{cm}^{-1}$, with a reduced intensity compared to the spectrum taken after annealing to 1000 K. This is due to partial decomposition and desorption of the oxide film.

Bragg reflections forming a LEED pattern are observed the first time observed after annealing to 1000 K, for lower temperatures the LEED image is diffuse. A

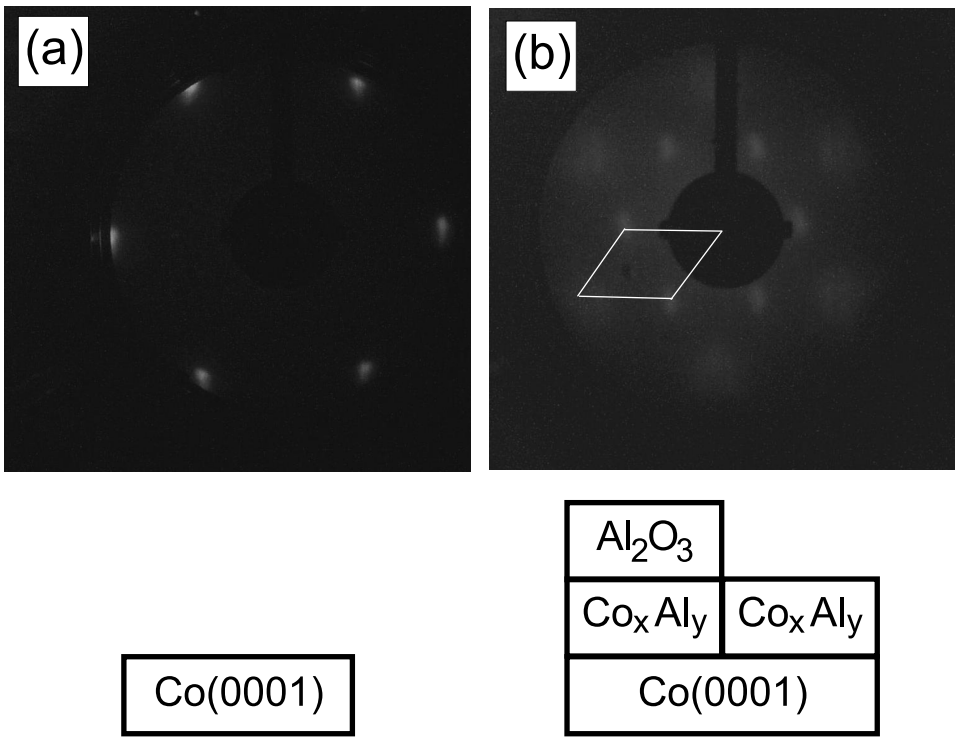

Figure 7.13: *LEED images of (a) the clean Co(0001) surface and (b) the oxidized Al/Co(0001) system after annealing to 1100 K, both at a primary energy of 60 eV.*

LEED image of the film after annealing to 1100 K is shown in Fig. 7.13(b), and Fig. 7.13(a) shows a LEED pattern of the clean Co(0001) surface for comparison. The pattern of the Co(0001) substrate is not observed in Fig. 7.13(b) and thus it is likely that no areas of clean Co are present on the surface. The observed pattern corresponds to a hexagonal surface structure with a two-dimensional lattice constant of 5.02 ± 0.15 Å. The existence of the α-Al_2O_3 , which exhibits hexagonal close packing of the oxygen sublattice and has a lattice constant of 4.76 Å, is ruled out, because two losses in the EEL spectra are expected, but three losses are observed in Fig. 7.12(a). The surface structure is the same that was found for the oxidation of the Co_xAl_y/Co(0001) system which was presented in Fig. 7.8. It is therefore likely that the film is not completely oxidized and that intermixing of Al and Co takes place. This is in accordance with the decrease of the Al/Co ratio and the increase of the O/Al ratio in Fig. 7.11. Thereby the alloy Co_xAl_y is formed, and it is likely that the Al_2O_3 film adopts the structure of the Co_xAl_y alloy. After annealing to 1100 K there are probably oxide covered areas at the surface and also areas of the Co_xAl_y alloy that are free of oxide. This situation is indicated by the schematic in Fig. 7.8.

Finally the thickness of the film is addressed. By applying equation (3.4), where a mean free path of 14 Å for the electrons of the Co LMM transition at 656 eV in Al_2O_3 [35] is used, the thicknesses of the oxide films for different annealing temperatures are

- $d_{900\,K} \approx 18.1$ Å
- $d_{1000\,K} \approx 16.7$ Å
- $d_{1100\,K} \approx 6.8$ Å.

The determination of these thicknesses is based on the assumption that an Al_2O_3 film is formed on the cobalt substrate without an interface layer. A more accurate determination of the thickness is not possible with the available data. As in section 7.2 a substantial decrease of the thickness for annealing temperatures above 1000 K is observed.

Summarizing, deposition of 14.6 Å Al on Co(0001) and subsequent oxidation to saturation at room temperature leads to an incomplete oxidation of the Al film. The Al_2O_3 layer is amorphous. Upon annealing to 1000 K interdiffusion of Al and Co takes place resulting in the formation of the Co_xAl_y alloy, which exhibits a hexagonal surface structure with a two-dimensional lattice constant of 5.02 ± 0.15 Å. The Al_2O_3 film adopts the structure of the Co_xAl_y alloy. For annealing temperatures above 1100 K the oxide film is decomposed and desorbed from the surface and also the Co_xAl_y alloy is decomposed.

7.4 Deposition of Al on Co(0001) in Oxygen Atmosphere

In the foregoing sections of this chapter the room temperature oxidation of the systems Co_xAl_y/Co(0001) and Al/Co(0001) were studied. Upon annealing, the oxide films adopted the structure of the Co_xAl_y alloy, which was shown in section 7.1 to exhibit a hexagonal surface structure with a two-dimensional lattice constant of 5.02 ± 0.15 Å.

From the experiments on the Ni(100) substrate it is known that, if aluminum is deposited with a rate of 0.48 Å/min in an oxygen atmosphere of $p_{O_2} = 1 \cdot 10^{-7}$ mbar, an Al_2O_3 film develops which contains no unoxidized aluminum. In this section the corresponding experiment on the Co(0001) substrate is described.

The peak-to-peak amplitudes of the oxygen KLL transition at 503 eV, the cobalt LMM transition at 656 eV, and the Al KLL transition at 1396 eV are shown in Fig. 7.14(a) for the deposition of Al with a deposition rate of r = 0.48 Å/min in an oxygen atmosphere of $p_{O_2} = 1 \cdot 10^{-7}$ mbar at room temperature. For the

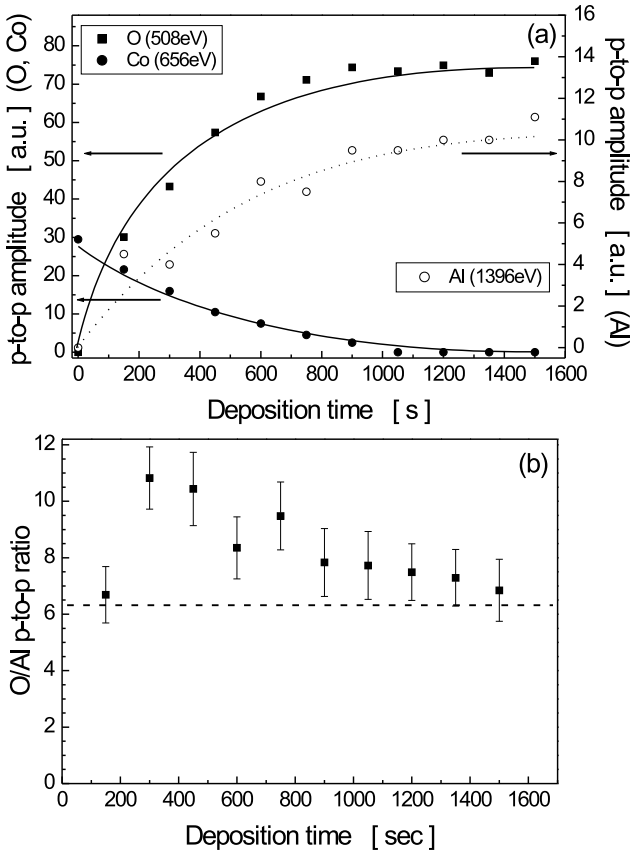

Figure 7.14: *Peak-to-peak amplitudes of the AES signals O at 503 eV, Co at 656 eV, and Al at 1396 eV (a), and the ratio O_{503}/Al_{1396} as a function of the deposition time (b). The schematic indicates the different escape depths of the electrons contributing to the Al_{1396} and O_{503} signals.*

discussion of Fig. 7.14(a) the different mean free paths of electrons in Al_2O_3 are important: $\lambda_O = 13$ Å, $\lambda_{Co} = 14$ Å, and $\lambda_{Al} = 28$ Å [35]. The thickness of the aluminum oxide layer can be determined from the AES signal of the Co LMM transition at 656 eV by using equation (3.4). The thickness amounts to 10.6 ± 2 Å after a deposition time of 450 s and 25.5 ± 2 Å after 900 s. After a deposition time of 1050 s the Co AES signal is below the background level and a determination of the film thickness is not possible. The oxygen signal has reached a saturation at about the same deposition time, because the mean free paths of electrons are similar for oxygen and cobalt. The aluminum signal, for which the electrons have a much larger mean free path (28 Å), i.e., a larger escape depth, does not reach a saturation level.

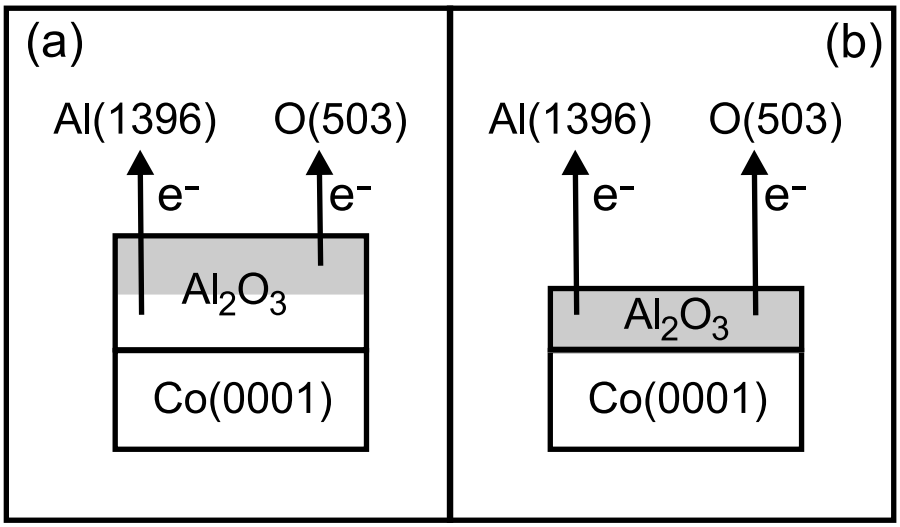

Figure 7.15: *Schematic of Al_2O_3 films of different thickness. Due to the large mean free path electrons of the Al AES transition at 1396 eV escape from the whole volume of the Al_2O_3 films, whereas electron of the O AES transition at 503 eV escape only from the gray shaded volume.*

It is also interesting to regard the ratio O_{503}/Al_{1396} in Fig. 7.14(b). Except for the first point at 150 s the ratio decreases as a function of the deposition time and, finally, approximates the value of bulk Al_2O_3 [33], which is indicated by the dashed line. The reason for the decrease is the different mean free path of electrons of the O signal at 503 eV compared to electrons of the Al signal at 1396 eV. This leads to a smaller volume of the film contributing to the O signal. This is indicated in the schematics of Fig. 7.15: In Fig. 7.15(a) the thickness of the Al_2O_3 film is comparable to the mean free path of the electrons of the Al AES transition at 1396 eV, which is 28 Å. Thus the complete volume of the Al_2O_3 film contributes to the Al AES transition. However, electrons of the O AES transition at 503 eV have a mean free path of only 13 Å and can thus escape only from the gray shaded part of the Al_2O_3 film. In this case the ratio of O/Al corresponds to the value of bulk Al_2O_3. In Fig. 7.15(b) again the gray shaded part of the Al_2O_3 film contributes to the O AES signal. However, the film is thinner than the escape depth of the electrons of the Al AES transition, thus the Al AES signal is diminished in comparison to the film in Fig. 7.15(a). Since the O AES signal is the same for both of the films, the ratio O/Al is enhanced. This explains the decrease of the O/Al ratio with increasing film thickness in Fig. 7.14(b).

In Fig. 7.16 AES spectra in the energy region between 20 and 120 eV are shown of the clean Co(0001) substrate, after deposition in $p_{O_2} = 1 \cdot 10^{-7}$ mbar at room temperature (b), and after oxidation of the film with 1500 L O_2 at room

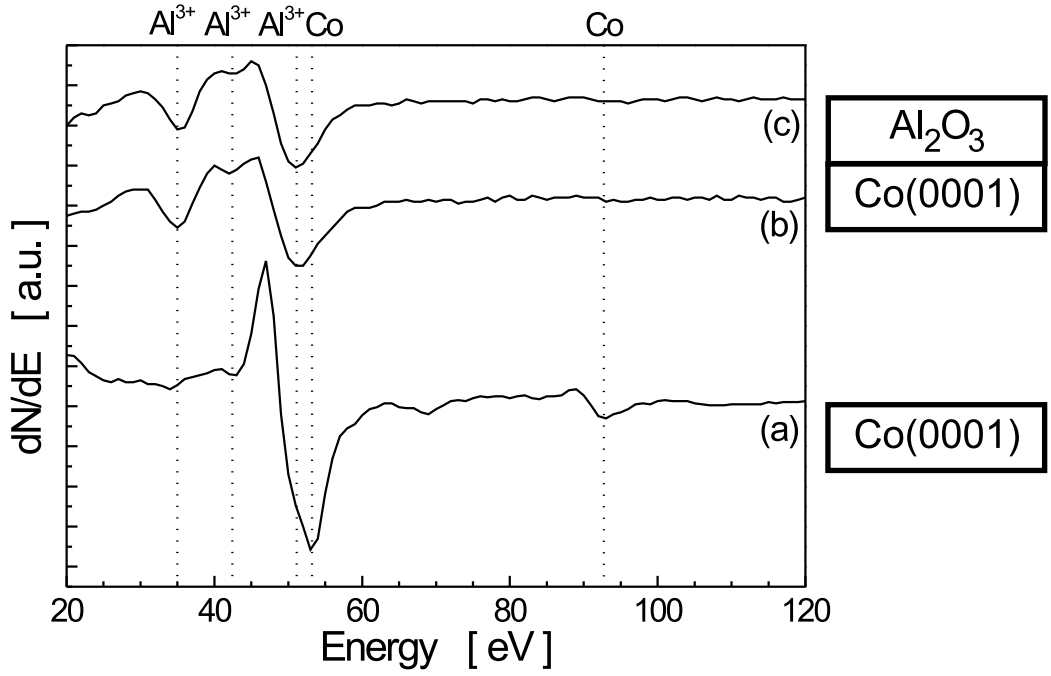

Figure 7.16: *AES spectra of the clean Co(0001) surface (a), after the deposition of nominally 12 Å Al in* $p_{O_2} = 1 \cdot 10^{-7}$ *mbar (b), and after further oxidation at 300 K with 1500 L of oxygen (c).*

temperature (c). Spectrum (a) shows the Co MNN transitions at 53 and 95 eV [33]. After the deposition of nominally 12 Å Al in O_2 atmosphere the AES spectrum (b) exhibits only the LMM transitions of Al^{3+} at 35, 43, and 51 eV. The thickness of the Al_2O_3 film cannot be determined, because the AES signal of the Co(0001) substrate is below the background level after deposition. After further oxidation of the film with 1500 L O_2 neither the position nor the lineshape of the observed transitions is changed. Additionally, in Fig. 7.17 the ratio of the oxygen transition at 503 eV and the aluminum transition at 1396 eV is shown. Within the experimental error the ratio does not change, indicating that the amount of oxygen does not change upon oxidation of the film. It is thus very likely that deposition of Al with a deposition rate of 0.48 Å/min in an oxygen atmosphere of $p_{O_2} = 1 \cdot 10^{-7}$ mbar generates a completely oxidized Al_2O_3 film.

The Al_2O_3/Co(0001) system is then annealed in steps of 100 K until 1300 K and then to 1350 K. Each step of annealing lasted for two minutes. In the preceding section, where Al was deposited on Co(0001) and then oxidized, the ratio

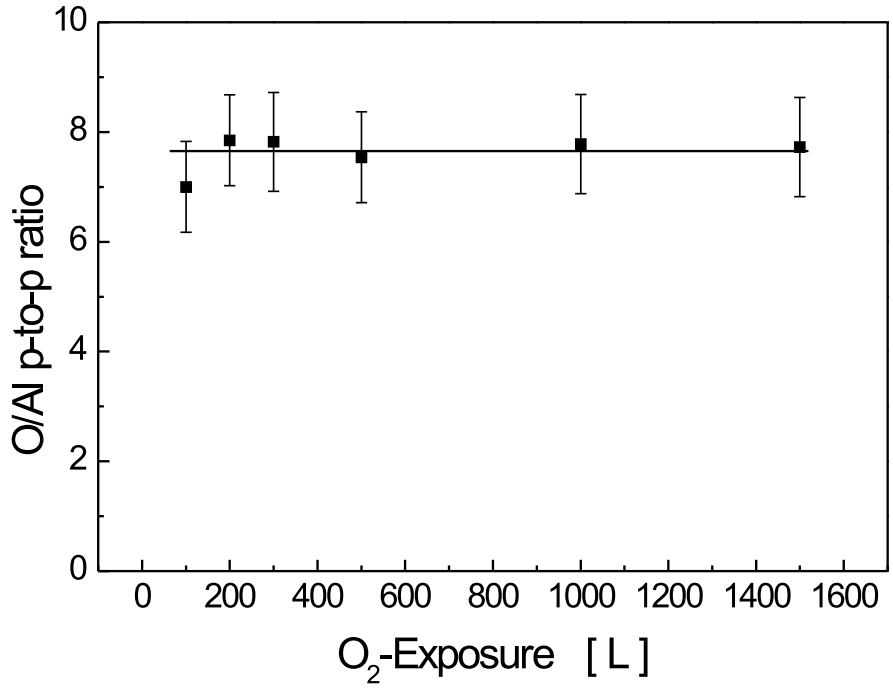

Figure 7.17: *Peak-to-peak ratio of O_{503}/Al_{1396} as a function of the oxygen exposure.*

O/Al increased upon annealing. The reason for this increase was the diffusion of unoxidized Al into the bulk of the substrate. For the deposition of Al in O_2 atmosphere the ratio O_{503}/Al_{1396} during annealing is shown in Fig. 7.18 (left axis). Up to 1300 K the ratio is constant, and thus the existence of unoxidized Al is very unlikely. A discussion based on the kinetic gas theory was given in the preceding chapter for the corresponding experiment on the Ni(100) substrate. It applies here as well, because both the deposition rate and the oxygen partial pressure are the same. The result of this discussion was, that there is in principle sufficient oxygen to form stoichiometric Al_2O_3. The average value of the O/Al ratio is ~ 7.5, which is slightly higher than the value of bulk Al_2O_3 (~ 6.2 [33]). This originates from the film thickness, which is most probably comparable to the mean free path of Al (28 Å [35]). A determination of the film thickness using equation (3.4) is only possible after annealing to 1200 K and higher temperatures, because the AES signal of Co is above the background level due to the partial desorption of the Al_2O_3 film. The thicknesses resulting from 14 Å for the mean free path of electrons of the Co transition at 656 eV are:

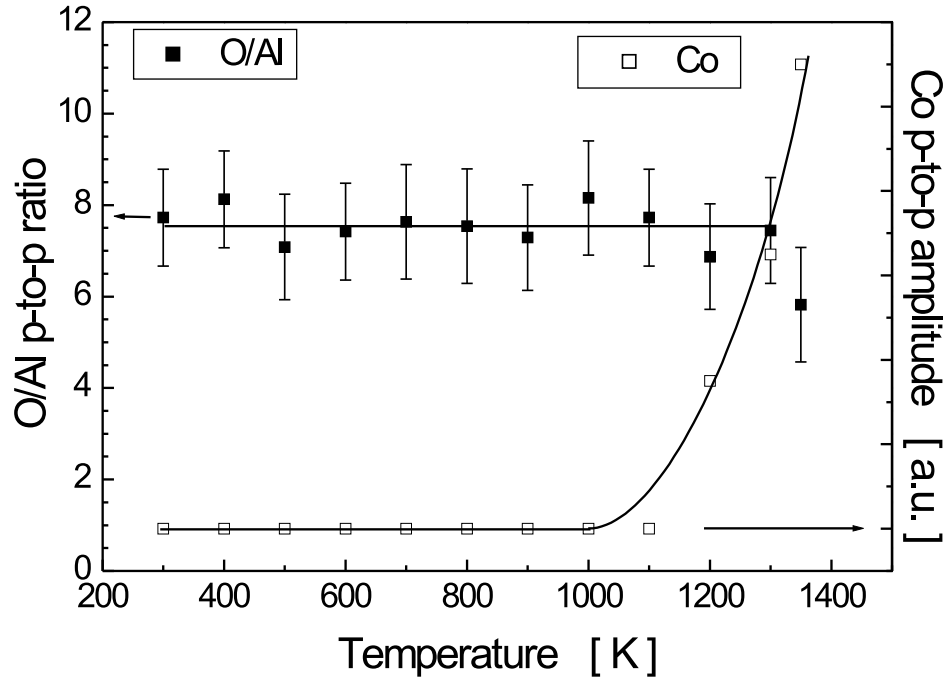

Figure 7.18: *Peak-to-peak ratio of O_{503}/Al_{1396} (left axis) and peak-to-peak amplitude of the Co transition at 656 Å (right axis) as a function of the annealing temperature.*

- $d_{1200\,K} = (24.4 \pm 2)$ Å
- $d_{1300\,K} = (17.3 \pm 2)$ Å
- $d_{1350\,K} = (11.2 \pm 2)$ Å

The thickness of the film after annealing to 1200 K appears quite large in view of the nominally deposited 12 Å of aluminum. Although desorption of the alumina film sets in at 1200 K the oxide seems to be stable at higher annealing temperatures than the alumina films prepared by oxidizing the Al/Co(0001) and Co_xAl_y/Co(0001) systems. This also supports the conclusion that there is no interface layer between the alumina film and the substrate, that tends to destabilize the alumina film.

The structural properties of the Al_2O_3 film are revealed by the EELS data in combination with the LEED data. After oxidation at room temperature the EEL spectrum shows only very broad losses around 540 and 880 cm^{-1} (not shown).

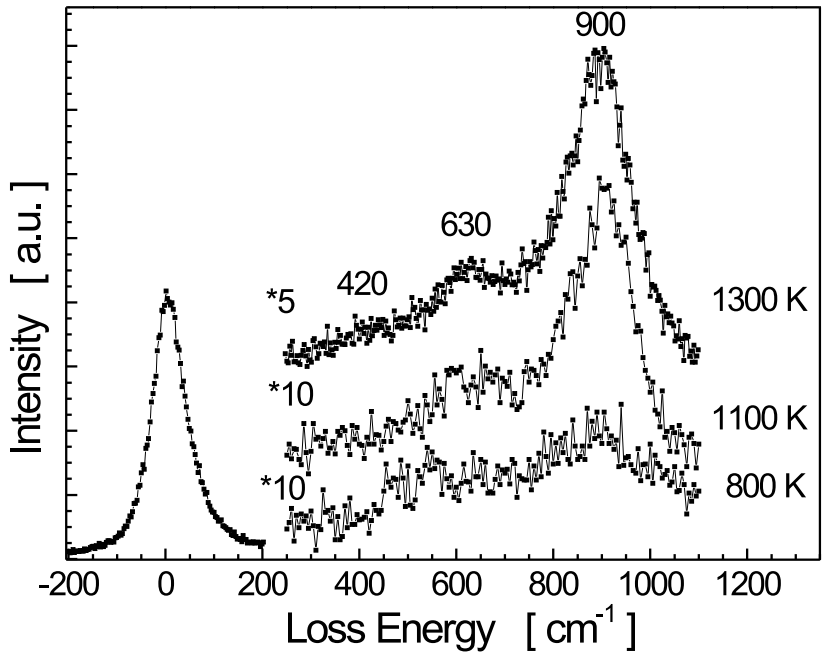

Figure 7.19: *EEL spectra after annealing to different temperatures. After annealing to 1300 K the spectrum exhibits three losses at 420, 630, and 900 cm^{-1}, that are characteristic for γ'-Al_2O_3. The spectra were recorded at room temperature.*

The LEED image after oxidation is diffuse, and thus the Al_2O_3 film is probably amorphous. Between room temperature and 700 K no significant change in the spectra occurs. At 800 K the frequency of the two losses is shifted to 550 and 890 cm^{-1} as can be seen in Fig. 7.19. After annealing to 1100 K three losses are observed at 370, 620 and 910 cm^{-1}. After annealing to 1300 K the frequencies of the losses are shifted to 420, 630, and 900 cm^{-1}. The intensity of the loss at 420 cm^{-1} is decreased in comparison to the losses at 420 cm^{-1} of the Al_2O_3 film prepared by oxidation of the Co_xAl_x/Co(0001) and Al/Co(0001) systems. The three dipole active modes rule out the existence of amorphous- and α-Al_2O_3 [81].

The LEED pattern in Fig. 7.20(b) has a very low intensity. It shows one domain with a hexagonal surface structure and a two-dimensional lattice constant of (2.81 ± 0.2) Å. A scheme of the pattern is shown next to Fig. 7.20. The lattice constant corresponds to the distance of the O^{2-}-ions in a close packed oxygen lattice [110]. Since the existence of α-Al_2O_3 is ruled out from the EELS data, the existence of the γ'-Al_2O_3 phase is concluded, which has a fcc sublattice of oxygen ions. It grows with the (111) plane parallel to the (0001) plane of the substrate.

In contrast to the oxide films discussed in sections 7.2 and 7.3, the oxide film in Fig. 7.20(b) is not rotated with respect to the substrate.

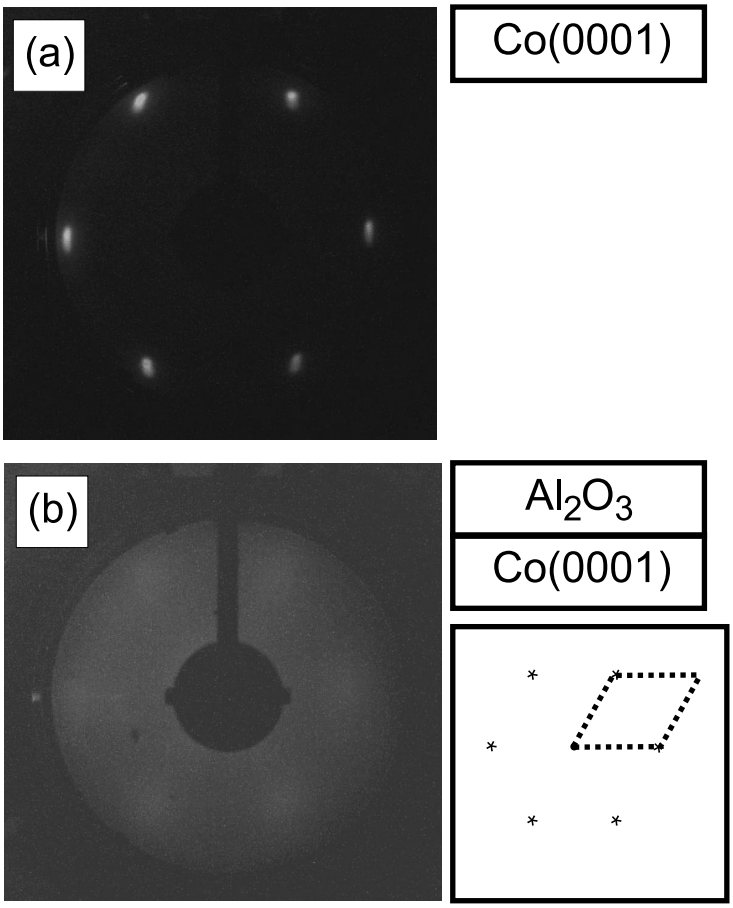

Figure 7.20: *LEED images of (a) the clean Co(0001) surface, and (b) the oxide after annealing to 1200 K, the primary energy was 70 eV in both of the images, and the oxide film has a thickness of (24.4±2) Å. Also shown is a schematic reproduction of the image in (b).*

Further annealing of the film at 1350 K and above results in desorption of the Al_2O_3 film, and the LEED pattern of the Co(0001) surface reemerges (not shown).

In summary, in this section it was shown that a thin film of γ'-Al_2O_3 can be grown on the Co(0001) substrate by deposition of aluminum on Co(0001), with a deposition rate of 0.48 Å/min at room temperature in an atmosphere of molecular oxygen of $1 \cdot 10^{-7}$ mbar and subsequent oxidation and annealing. The γ'-Al_2O_3 film is identified by the three Fuchs-Kliewer phonons in the EEL spectra at 420, 630, and 900 cm^{-1}, and by a hexagonal structure of the LEED pattern,

from which the lattice constant is determined to be (2.81 ± 0.2) Å.

In this chapter the growth of Al_2O_3 films on Co(0001) was studied. Upon deposition and annealing of Al on Co(0001) the ordered alloy Co_xAl_y is formed. Oxidation and annealing of the Co_xAl_y/Co(0001) system leads to the formation of an Al_2O_3 film that adopts the structure of the Co_xAl_y alloy. Deposition of Al on Co(0001) and direct oxidation of the Al film leads to a not completely oxidized film. Upon annealing, alloying of unoxidized Al and Co takes place and the Co_xAl_y alloy is formed. The Al_2O_3 film adopts the structure of the Co_xAl_y alloy. For the deposition of Al in an O_2 atmosphere of $1 \cdot 10^{-7}$ mbar and subsequent oxidation with 1500 L of oxygen at 300 K no unoxidized Al remains. Annealing of the Al_2O_3 film leads to ordering, and a γ'-Al_2O_3 film is grown.

This chapter concludes the structural characterization of Al_2O_3 films on ferromagnetic substrates and of metal deposits on the Al_2O_3 films.

Chapter 8

Electronic Transport Measurements

In chapters 5 and 7 the growth of thin Al_2O_3 films on Ni(100) and Co(0001) were studied, respectively. In these chapters only the structural characterization was performed. However, for use in microelectronics the electronic properties of thin oxide films are also important. Therefore, this chapter will deal with electronic transport measurements.

The electronic transport measurements were performed by scanning tunneling spectroscopy (STS), which was described in section 3.4. It basically consists of ramping the bias voltage of the STM tip and measuring the tunneling current, while the distance between tip and sample is kept constant. In this way I(V)-curves are obtained from well defined points of the surface. The derivative of these I(V)-curves can be normalized, so that it is proportional to the local density of states (LDOS) of the surface [46, 51].

An example of STS measurements of the (2x1) reconstructed Si(111) surface was discussed in section 3.4. The STS measurements performed by Stroscio et al. [54] and by Feenstra et al. [52] on the (2x1) reconstruction of the Si(111) surface are in accordance with work function measurements [131], optical absorption [132], polarization dependence of the absorption [133], angle resolved photoemission [134, 135, 136], and inverse photoemission [137]. Comparison of these experimental data with theoretical predictions [138, 139] confirmed the so-called π-bonded chain model for the (2x1) reconstructed Si(111) surface. This example shows, that there is considerable interplay between structural and electronic properties of a surface.

The Si(111)-(7x7) surface is well known [140, 141, 142, 143, 144, 145]. In the present work measurements on the Si(111)-(7x7) surface were performed in order to verify the functioning of the STS technique. In this work the (7x7) reconstruction of the Si(111) surface was obtained by annealing to 1500 K for

15 – 30 s.

The main purpose of this chapter consists of electronic transport measurements of thin oxide films. As a sample the β-Ga_2O_3/CoGa(100) system was chosen, because the structural properties of the CoGa(100) substrate as well as the structural properties of β-Ga_2O_3 are well established (see section 4.3.2). For use as tunnel barriers one has to be sure, however, that the thin oxide films are isolators. This is the reason for the importance of the electronic characterization of thin oxide films. The electronic transitions of β-Ga_2O_3 have been measured with EELS by Gassmann [23], and the band gapE_g was determined to be 4.5 eV, which is in accordance with the value of bulk Ga_2O_3 . However, metal induced gap states (MIGS) were also found. The value for the band gap was confirmed by Rose for amorphous and well ordered Ga_2O_3 on CoGa(100). For Al_2O_3, however, Costina [98] found a band gap of 3.2 eV for a thin film of amorphous Al_2O_3 and 4.3 eV for a thin film of well ordered Al_2O_3. This differs from the band gap of bulk γ-Al_2O_3 which amounts to 8.7 eV [146] and is an example of the interplay of structural and electronic properties of thin oxide films. Since the phase of Al_2O_3 changes upon annealing, the electronic properties might also change.

The measurement of the DOS of thin oxide films yields also a better understanding of topographic STM images. As discussed in section 3.4, during STM measurements tunneling can proceed between tip and oxide, if the tip voltage exceeds $E_g/2$, otherwise the tunneling proceeds between substrate and tip. If the DOS of substrate and oxide film are known, especially concerning states in the band gap, a better understanding of the topography of STM images is obtained.

This chapter is organized as follows: In section 8.1 STS measurements of the (7x7)-reconstruction of the Si(111) surface are presented and compared to existing data in the literature. This serves basically to establish the STS method. In section 8.2 first the structural properties of the CoGa(100) surface are reviewed. Then the I(V)-curves and normalized I(V)-curves are measured and discussed. In section 8.3 the structural properties of the β-Ga_2O_3/CoGa(100) system are summarized, and the I(V)-curves are presented and discussed. These measurements are compared to those of the clean CoGa(100) surface and examined with respect to the existence of a band gap.

8.1 The Si(111)-(7x7) surface

The (7x7) reconstruction of the Si(111) surface is very well known. It was for the first time studied by STM by Binnig and Rohrer [147]. Cleaving a Si crystal at room temperature yields a (2x1) reconstruction of the Si(111) surface, which has been found to have a π-bonded chain structure [31]. Annealing the (2x1) reconstructed surface to temperatures above 550 K (250°C) transforms the sur-

face irreversibly to the (7x7) reconstruction [148]. At 1100 K (830°C) the (7x7) pattern is reversibly replaced by a (1x1) pattern [31]. In this work the Si(111)-(7x7) surface was prepared by annealing the crystal to 1500 K for 15 – 30 s, while the pressure remained in the 10^{-10} mbar range. The (7x7) reconstruction was explained by Takayanagi et al. [149] in terms of the dimer-adatom-stacking-fault (DAS) model on the basis of transmission electron diffraction. This model gained further support by experiments [150, 151], and it was revealed by ab initio calculations [152, 153] that the (7x7) reconstruction has the lowest energy of all reconstructions that are compatible with the DAS model. The surface unit cell contains 12 Si adatoms, 6 rest atoms, 9 dimers, and one corner hole. An STM image with a scanned area of 400 x 400 Å^2 is shown in Fig. 8.1, and several unit cells are observed.

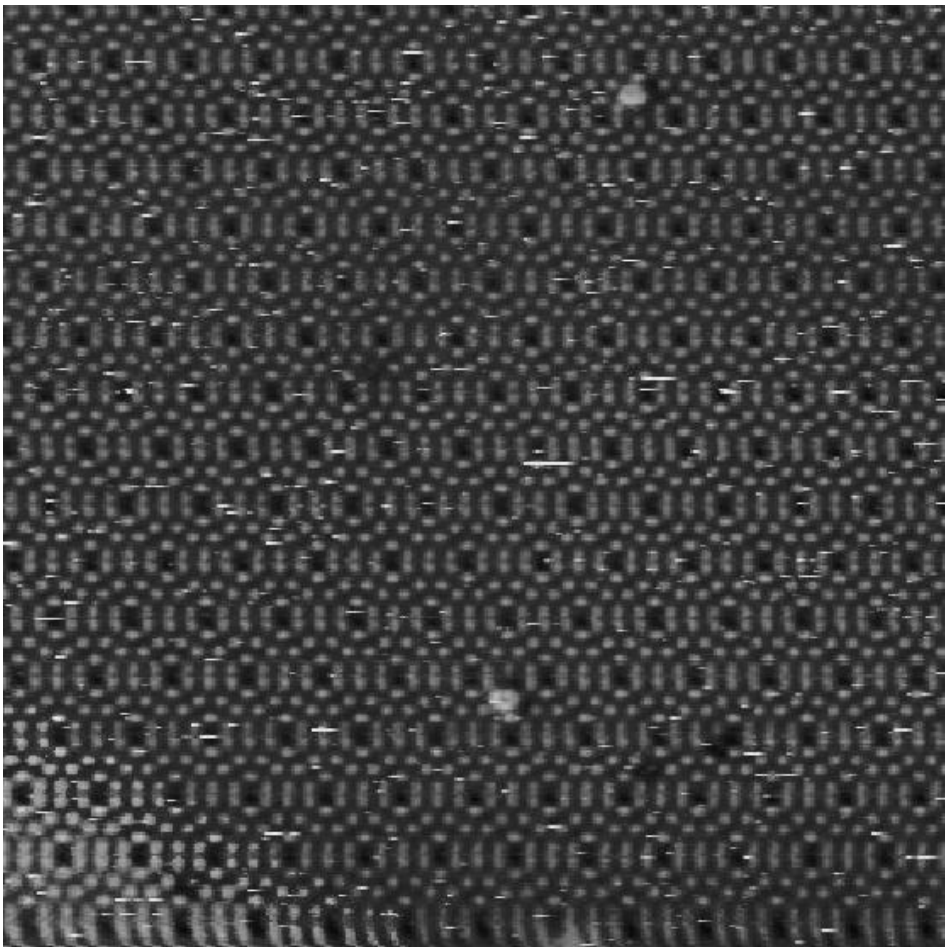

Figure 8.1: *STM image of the (7×7) reconstruction of the Si(111) surface. The area is 400 × 400 Å^2 (U_T = 2 V, I_T = 0.3 nA).*

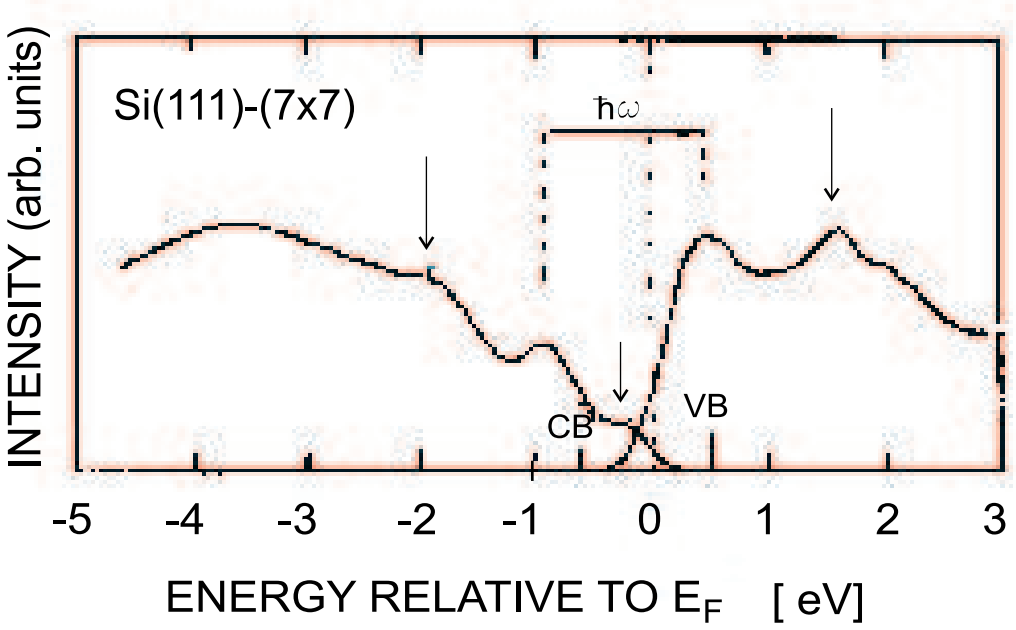

Figure 8.2: *DOS of the (7×7) reconstruction of the Si(111) surface reproduced from Layet et al. [140].*

A schematic distribution of occupied and empty states of the Si(111)-(7x7) surface, based on different experimental techniques, is shown in Fig. 8.2. The figure was first published by Layet et al. [140], and here it is reproduced from the book of Lüth [31]. The curves are based on different experimental data [154, 155, 156, 157, 158]. Maxima are observed at about -2, -1, and -0.45 eV and at 0.5 and 1.6 eV. In Fig. 8.3 a normalized I(V)-curve measured in the present work is shown. The maxima of the normalized I(V)-curve are at -2, -0.8, -0.4, 0.5 and 1.9 V which shows that the positions are approximately the same as in Fig. 8.2. Thus it is clear that the STS measurements yield reliable results. The intensities in Fig. 8.2 and Fig. 8.3 are different. However, it has been discussed in section 3.4 that the ratio $(dI/dV)/(I/V)$ agrees with the DOS only with respect to the position of the peaks and not with respect to the intensity.

8.2 The CoGa(100) Surface

The intermetallic alloy CoGa is known to crystallize in the CsCl (B2) structure. The lattice constant of CoGa is 2.878 Å [159], the melting point is 1207° C (for comparison: T_m(Co) = 1495° C and T_m(Ga) = 30° C).

In view of the crystal structure of bulk CoGa the (100) surface should have a quadratic unit cell displaying a C_4 symmetry. However, it was observed by LEED

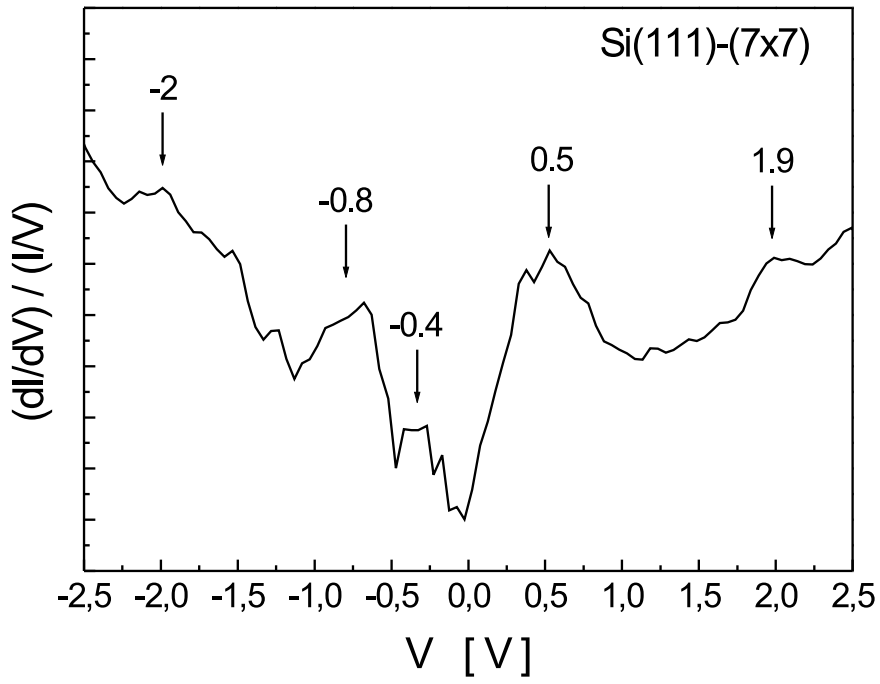

Figure 8.3: *Normalized I(V)-curve of the (7×7) reconstructed Si(111) surface.*

and thermal energy atom scattering (TEAS) [160, 161] and by LEED and STM [23], that the surface is reconstructed. The particular reconstruction depends on the cleaning procedure in the UHV that the CoGa single crystal is subjected to. This was observed by Gassmann [23] and more thoroughly studied by Kovacs [161]. It was found with AES, that for elevated temperatures ($T \geq 850\,K$ [160]) an enrichment of Ga on the surface occurs. Thermal desorption spectroscopy (TDS) revealed, that at 950 K desorption of Ga sets in, and at 1090 K Co begins to desorb. (This is the principle of the solid state evaporator that was discussed in section 2.3). It was also found, that the speed of cooling after thermal treatment is crucial for the reconstruction [161].

The CoGa(100) surface exhibits the c(4x2) and the $(\sqrt{5} \times \sqrt{5})R26.6°$ reconstructions. Which of the reconstructions dominates depends on the cleaning procedure. In the present work the CoGa(100) surface was prepared to exhibit mainly the c(4x2) reconstruction.

The step edges of the (100) surface are formed by (110)- and (111)-microfacets. The fact that the atomic structure of the step edges can be resolved by STM is remarkable, because for metallic surfaces there is usually too much

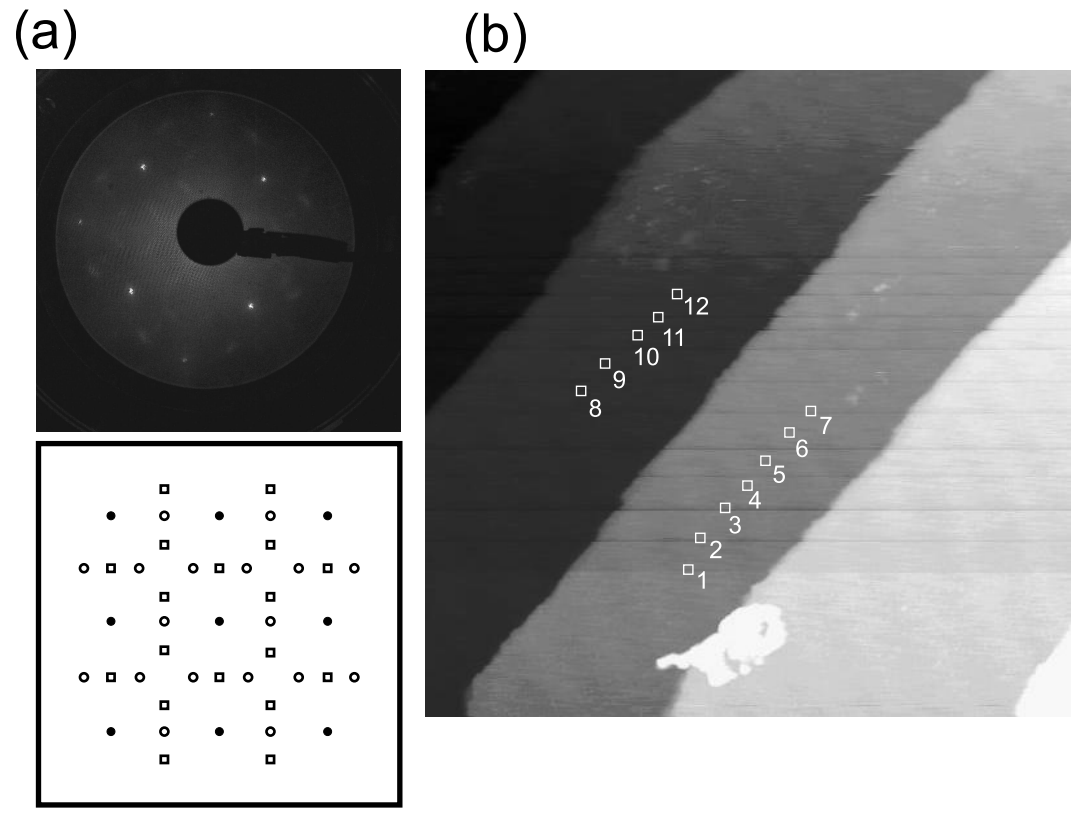

Figure 8.4: *(a) LEED image of the clean CoGa(100)surface with a primary energy of 87 eV and schematic representation of the image. (b)STM image of the CoGa(100) surface with a scanned area of 200 nm × 200 nm (U_t = -1.5 V, I_t = 1 nA). The squares indicate points where the I(V)-curves were measured.*

diffusion at room temperature. An example of fluctuations of the step edges is copper (Cu(110) [162] and vicinal Cu surfaces [163]). In contrast to Cu the step edges of the CoGa(100) surface are immobile at room temperature.

A LEED image of the CoGa(100) surface displaying a pattern of two domains with a c(4x2) reconstruction is shown in Fig. 8.4(a). In the schematic representation the (1x1) structure is indicated by solid circles, and the additional spots of the c(4x2) reconstruction are represented by open squares for one domain and by open circles for the other domain. The domains are oriented perpendicular to each other. The primary energy was 87 eV. A STM image of the surface with a scanned area of 200 nm × 200 nm is shown in Fig. 8.4(b). Four different terraces are observed, and I(V)-curves were measured on two terraces at the indicated locations.

I(V)-curves of the CoGa(100) surface are shown in Fig. 8.5. Fig. 8.5(a) shows an average of seven I(V)-curves that were measured in different locations of the

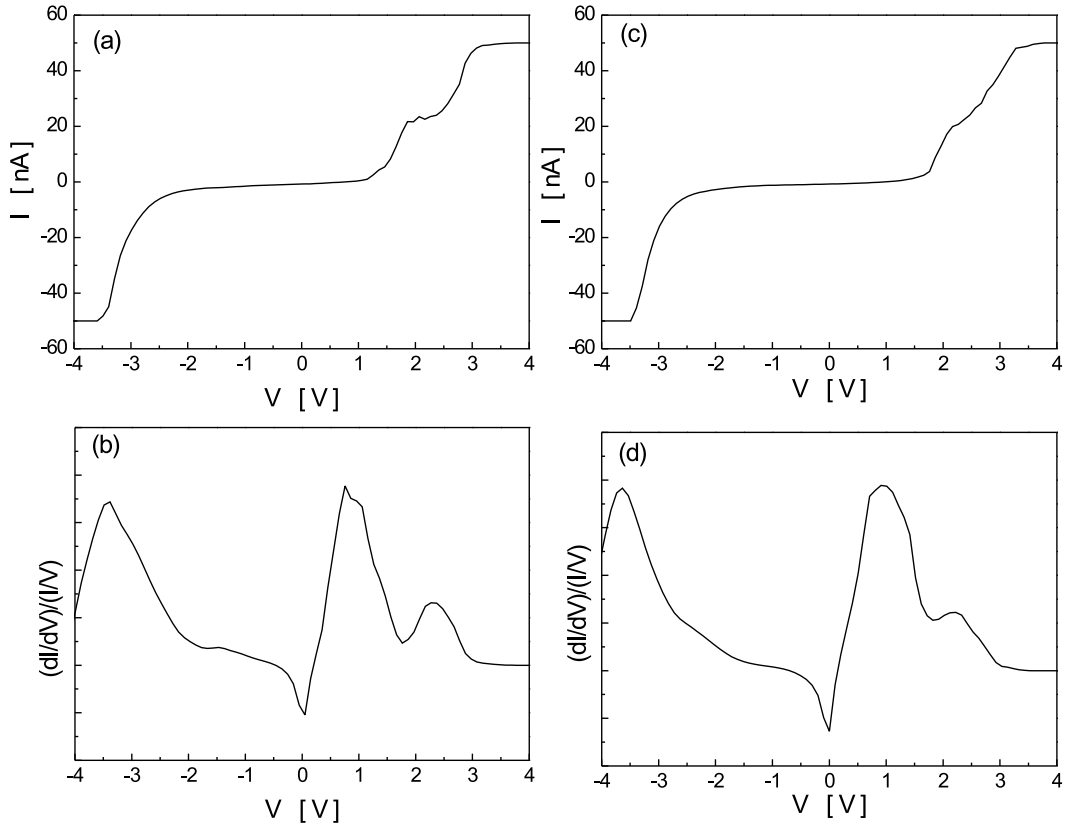

Figure 8.5: *I(V)-curves (a, c) and corresponding normalized I(V)-curves (b, d) of the clean (4×2) reconstructed CoGa(100) surface.*

same terrace as displayed in Fig. 8.4(b). The locations of the measurements are marked with squares numbered 1 to 7. The corresponding normalized I(V)-curve that reflects the density of states [50, 53] is shown in Fig. 8.5(b). Fig. 8.5(c) shows an average of five single I(V)-curves measured on a different terrace. The locations of the measurements of these curves are marked by squares numbered 8 to 12. The corresponding normalized I(V)-curve is shown in Fig. 8.5(d). The normalized I(V) curves (b) and (d) both display maxima at about -3.5, +1.0 and +2.2 V. The increase for small voltages (-0.2 ... 0.2 V) clearly indicates a conducting behavior of the CoGa(100) surface.

8.3 The β-Ga_2O_3/CoGa(100) system

The CoGa(100) surface that was discussed in the previous section is a suitable candidate for a substrate to grow β-Ga_2O_3 films. β-Ga_2O_3 is monoclinic with the lattice constants $a = 3.04\,\text{Å}$, $b = 5.80\,\text{Å}$, $c = 12.23\,\text{Å}$, and $\beta = 103.7°$ [72, 164], while for thin films of β-Ga_2O_3 on CoGa(100) the two-dimensional lattice constants amount to $a = 2.9\,\text{Å}$ and $b = 5.80\,\text{Å}$ [23, 26]. The lattice mismatch of the β-Ga_2O_3 oxide with respect to the CoGa(100) surface is thus 0.7% in one direction ($a_{\text{CoGa}} = 2.88\,\text{Å}$, $a_{\beta\text{-}Ga_2O_3} = 2.9\,\text{Å}$) and 0.7% in the other direction ($b_{\beta\text{-}Ga_2O_3} = 5.80\,\text{Å}$ and $2a_{\text{CoGa}} = 5.76\,\text{Å}$).

The heat of formation of Ga_2O_3 is -1080 kJ/mol [129] and is thus larger than the heat of formation of Co_3O_4 (-845 kJ/mol [129]). Hence, upon oxidation of the CoGa(100) surface Ga_2O_3 is formed. If the oxidation proceeds at room temperature, an amorphous Ga_2O_3 is formed as evidenced from two characteristic loss features in the EEL spectra (400 and 690 cm^{-1}) and a diffuse LEED image [23, 73]. After annealing the Ga_2O_3 film to 700 K the well ordered β-Ga_2O_3 is formed, which is identified by a (2x1) LEED pattern with respect to the CoGa(100) surface, and exhibits four losses in the EEL spectra (305, 455, 645, and 785 cm^{-1}). β-Ga_2O_3 is isomorphic to θ-Al_2O_3 , and the frequencies of the losses in EELS are shifted: 305 $\rightarrow$ 420, 455 $\rightarrow$ 605, 645 $\rightarrow$ 720, and 785 $\rightarrow$ 900 cm^{-1}. These shifts are due to the different masses of Ga and Al atoms [23]

STM images of the β-Ga_2O_3 surface (partially oxidized) [23, 25, 24, 26] reveal that the oxide forms rectangular islands. The step edges are oriented along the [100]- and [010]-directions of the substrate. β-Ga_2O_3 grows epitaxially on CoGa(100), and for this system a structural growth model was proposed by Gassmann [23] and Schmitz et al. [25]. It exhibits the so-called Bain orientation relationship between parallel oriented fcc (sublattice of O^{2-}-ions in Ga_2O_3) and bcc (CoGa) structures:

$$[110]_{\text{fcc lattice}} \quad \| \quad \left\{ \begin{array}{l} [100]_{\text{bcc lattice}} \\ [010]_{\text{bcc lattice}} \end{array} \right.$$

β-Ga_2O_3 can also be prepared by oxidation of the CoGa(100) surface at temperatures between 550 K and 930 K [28, 29]. The oxide desorbs from the surface at temperatures above 1070 K [23].

The bulk band gap of crystalline Ga_2O_3 is 4.4 eV [165]. For thin films of β-Ga_2O_3 Gassmann [23] found a band gap of 4.5 eV and additional states within the band gap centered at 3.3 eV. Rose [111] found a band gap of 4.7 eV for thin amorphous Ga_2O_3 as well as for β-Ga_2O_3.

A LEED image of the β-Ga_2O_3/CoGa(100) system with a primary energy of 87 eV is shown in Fig. 8.6. It displays a (2x1) pattern which is typical for β-Ga_2O_3. A STM image of the β-Ga_2O_3 surface is shown in Fig. 8.6(b) and different

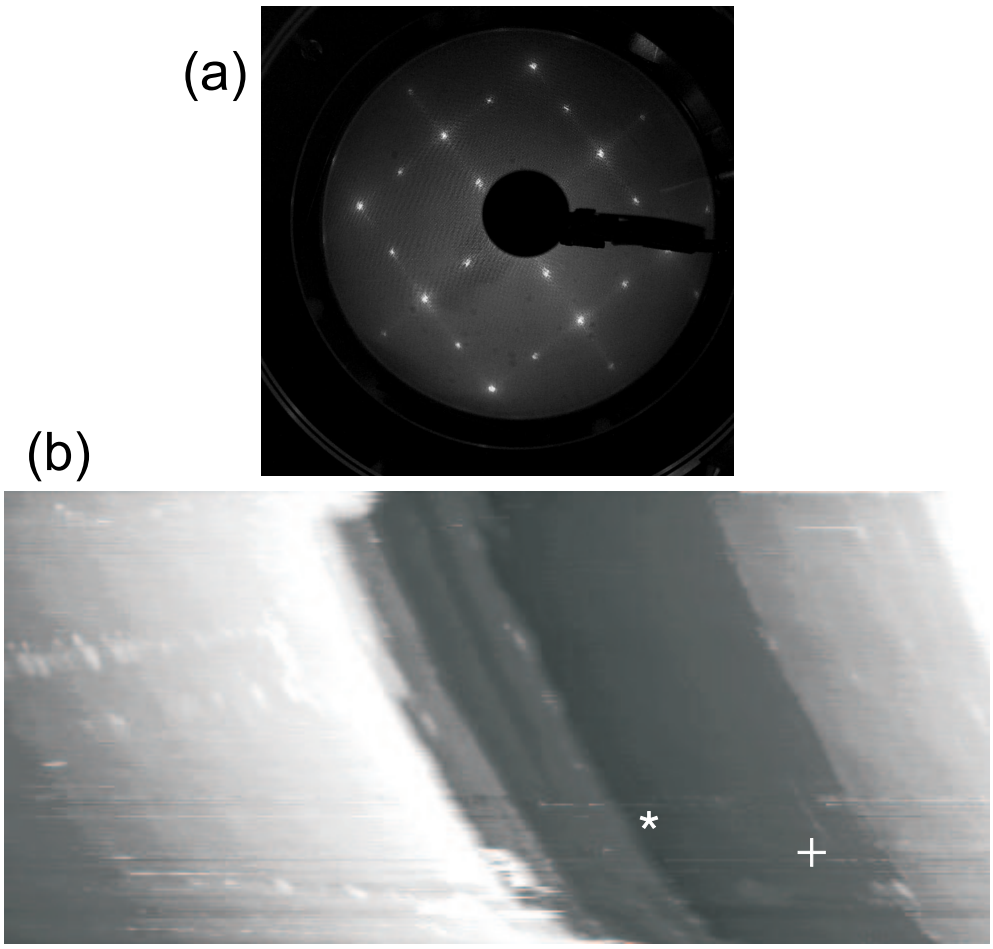

Figure 8.6: *(a) LEED image of the β-Ga_2O_3 /CoGa(100) system with a primary energy of 87 eV, and (b) STM image of the β-Ga_2O_3 surface with a scanned area of 115 nm × 250 nm (U_t = 3 V, I_t = 1 nA).*

terraces are observed. The white cross and the asterisk mark the locations, where the I(V)-curves were measured, that are displayed in Fig. 8.7. The points were chosen on different terraces but not at step edges.

An I(V)-curve of the β-Ga_2O_3 surface is shown in Fig. 8.7(a) and the corresponding normalized I(V)-curve is shown in Fig. 8.7(b). The curve was measured at the location that is marked with a white cross in Fig. 8.6(b). The normalized I(V)-curve and hence the density of states remains zero for voltages smaller than 2 V. This evidences the insulating behavior of the β-Ga_2O_3 film. The normalized I(V)-curve displays maxima at 2.2, 2.7, 3.4, 3.9 and 4.6 eV. The normalized I(V)-curve in Fig. 8.7(c) was measured on a different terrace (This might not be visible in Fig. 8.6(b)). The location is marked with an asterisk in Fig. 8.6(b). The

density of states remains also zero for voltages smaller than 2 V and thus confirms the insulating behavior of the β-Ga_2O_3 film. The maxima of this curve are at 2.5, 3.0, 3.8, 4.3 and 4.8 V. The positions of the maxima differ from those of Fig. 8.7(b) by 0.2 – 0.3 V. However, the insulating properties of the film are not affected by these shifts. Due to the similarity of the two normalized I(V)-curves, that were measured at different terraces, it is likely that the density of states is similar for points on different terraces. Hagendorf et al. [166] prepared ultrathin CoO films on Ag(001) and found a maximum at 2.2 V in the normalized I(V)-curve of the CoO/Ag(001) system.

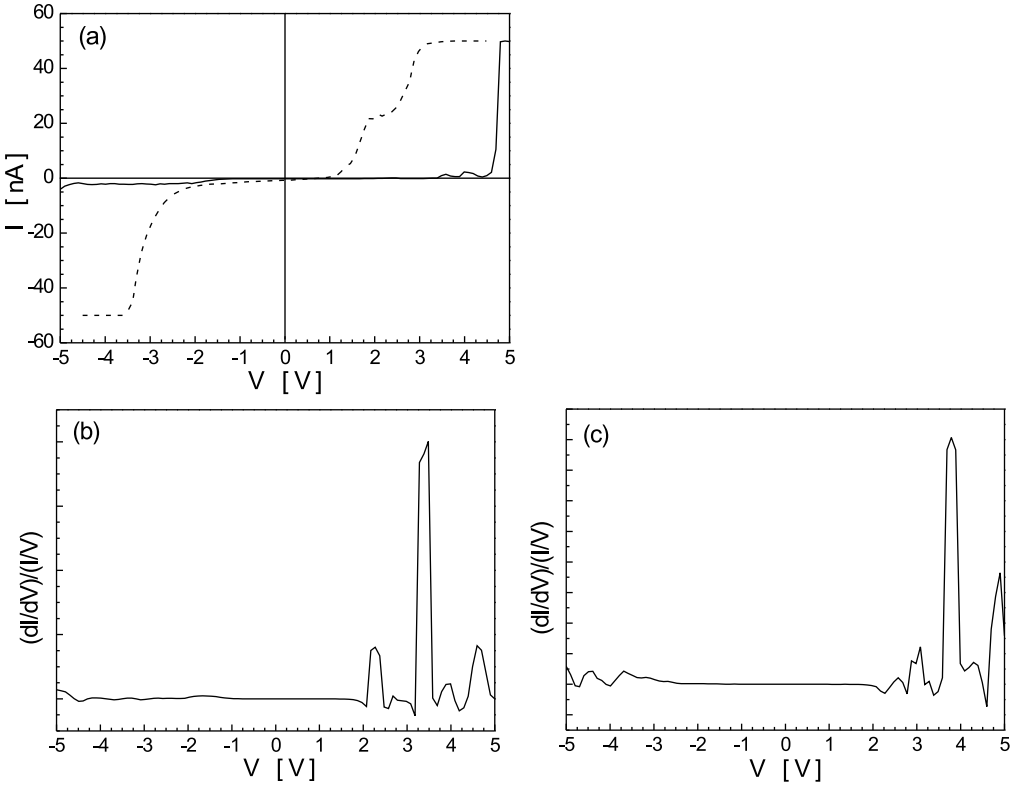

Figure 8.7: *(a) I(V)-curve of β-Ga_2O_3 (solid line) measured at the location marked with a white cross in Fig. 8.6(b) and I(V)-curve of the CoGa(100) surface (dashed line) reproduced from Fig. 8.5. (b) normalized I(V)-curve obtained from normalization of the I(V)-curve of β-Ga_2O_3 in (a). (c) normalized I(V)-curve measured at the location marked with the asterisk in Fig. 8.6(b).*

The fact that the thin β-Ga_2O_3 film has the properties of an insulator confirms the results of Gassmann [23] and Rose [111], who found that thin β-Ga_2O_3 films

have a band gap of 4.5 and 4.7 eV, respectively. The maxima with the highest intensity in Fig. 8.7(b) is located at $\sim$3.4 V and in Fig. 8.7(c) it is located at 3.8 eV. Thus these maxima do not match exactly the band gap found by Rose [111] and Gassmann [23].

Chapter 9

Summary

The aim of this work is the preparation and characterization of thin well-ordered aluminum oxide films on the ferromagnetic substrates Ni(100) and Co(0001), as well as electronic transport measurements of the system β-Ga_2O_3/CoGa(100). The structural characterization was performed by Auger electron spectroscopy (AES), low energy electron diffraction (LEED), electron energy loss spectroscopy (EELS), and scanning tunneling microscopy (STM). The electronic transport measurements were achieved by scanning tunneling spectroscopy (STS).

It is known that oxygen adsorption on $Ni_3Al(100)$ at room temperature (RT) leads to the formation of a thin amorphous aluminum oxide layer. On the other hand it is known that deposition of aluminum on Ni(100) and annealing leads to the formation of a surface alloy of Ni_3Al on Ni(100). These two steps were combined in this work to grow an Al_2O_3 film on Ni(100).

Growth of Al_2O_3 on Ni(100)

A 12 Å thick Al layer was deposited on the Ni(100) surface at room temperature (RT) and subsequently annealed to 1150 K resulting in a thin film of Ni_3Al, which grows with the (100) plane parallel to the (100) plane of the substrate. Oxidation of Ni_3Al/Ni(100) until saturation at RT leads to the growth of an Al_2O_3 layer consisting of different alumina phases. Upon annealing to 1000 K a well-ordered film of γ'-Al_2O_3 is formed, which grows in two domains, that are rotated by 90° with respect to each other. The γ'-Al_2O_3 grows with the (111) plane parallel to the Ni(100) surface. The thickness of the film amounts to 8 ± 2 Å, which corresponds to twice the lattice constant of γ'-Al_2O_3. Oxidation of the system Ni_3Al/Ni(100) at 800 K to saturation and subsequent annealing to 1350 K leads also to the formation of the γ'-Al_2O_3. However, the oxide film grows in 6 domains, which are rotated by an angle of 15° with respect to each other.

Deposition of 12 Å Al on Ni(100) and oxidation of the Al/Ni(100) system to saturation at RT leads to incomplete oxidation of the Al film. During annealing of the oxidized Al/Ni(100) system unoxidized Al diffuses into the bulk of the substrate. A phase of Al_2O_3 with long range order cannot be identified during annealing.

Deposition of Al on Ni(100) with a rate of 0.48 Å/min in an oxygen atmosphere of $1 \cdot 10^{-7}$ mbar at RT leads to the formation of an amorphous Al_2O_3 film. No hints of unoxidized Al are found. Annealing of the Al_2O_3 film up to 1400 K results in the formation of a well ordered γ'-Al_2O_3 film, that grows with the (111) plane parallel to the (100) plane of the substrate. The thickness of the film amounts to 17.2 ± 2 Å.

Growth of Co on Al_2O_3/Ni(100)

14.4 Å of Co were deposited on Al_2O_3/Ni(100) at RT. The observation of Fuchs-Kliewer phonons of Al_2O_3 for Co coverages of more than one monolayer is in agreement with the Volmer-Weber growth mode of Co on Al_2O_3. Annealing of the system Co/Al_2O_3/Ni(100) shows, that the Co film is stable up to about 700 K. Above 700 K Co diffuses into and through the oxide film.

Growth of Al_2O_3 on Co(0001)

A 7.8 Å thick Al film was deposited on Co(0001) at RT. Annealing of the Al/Co(0001) system to 400 K results in alloying of Al and Co. The alloy exhibits a hexagonal surface structure with a two-dimensional lattice constant of 5.02 ± 0.15 Å. None of the known bulk CoAl alloys is formed, and the alloy is referred to as Co_xAl_y. Oxidation of the Co_xAl_y/Co(0001) system to saturation at RT leads to the formation of an amorphous Al_2O_3 layer. Upon annealing of the oxide layer up to 1200 K, the oxide film is well ordered and adopts the structure of the Co_xAl_y alloy.

A 14.6 Å thick Al film was deposited on Co(0001). The system Al/Co(0001) was oxidized until saturation at RT, which results in the formation of an amorphous Al_2O_3 layer. During annealing unoxidized Al diffuses into the Co(0001) substrate and forms the Co_xAl_y alloy. The Al_2O_3 film adopts the structure of this alloy.

Deposition of Al on Co(0001) with a rate of 0.48 Å/min in an oxygen atmosphere of $1 \cdot 10^{-7}$ mbar at RT results in an amorphous Al_2O_3 film. Upon annealing no evidence for diffusion of unoxidized Al is found, and no alloying of Al and Co takes place. Annealing to 1200 K results in ordering of the oxide film, and the

γ'-Al_2O_3 phase is formed, which grows with the (111) plane parallel to the (0001) plane of the substrate. The thickness of the film amounts to 24.4 ± 2 Å.

Electronic Transport measurements

The normalized I(V)-curve (dI/dV)/(I/V) of the Si(111)-(7x7) surface is shown to reflect the density of states of the surface. This confirms the functioning of the STS technique. The normalized I(V)-curve of CoGa(100) increases for small voltages (-0.2 V ... 0.2 V), which reveals a metallic behavior of the surface. For the well ordered β-Ga_2O_3/CoGa(100) system the normalized I(V)-curve is constant in the voltage region -1.5 V ... 1.5 V, and, thus, exhibits an insulating behavior.

Bibliography

[1] M. Henzler and W. Göpel, *Oberflächenphysik des Festkörpers* (Teubner, Stuttgart, 1994).

[2] M. Julliere, Phys. Lett. **54**, 225 (1975).

[3] G. Binasch, P. Grünberg, F. Saurenbach and W. Zinn, Phys. Rev. B **39**, 4828 (1989).

[4] N.N. Baibich, J.M. Broto, A. Fert, F. Hguyen Van Dau, F. Petroff, P. Etienne, G. Creuzet, A. Friedrich and J. Chazelas, Phys. Rev. Lett. **61**, 2472 (1988).

[5] J.S. Moodera, L.R. Kinder, T.M. Wong and R. Meservey, Phys. Rev. Lett. **74**, 3273 (1995).

[6] T. Miyazaki and N. Tezuka, J. Mag. Mag. Mat. **139**, L231 (1995).

[7] P. Rottländer, H. Kohlstedt, H.A.M. de Gronckel, E. Girgis, J. Schelten and P. Grünberg, J. Mag. Mag. Mat. **210**, 251 (2000).

[8] P. Gassmann, R. Franchy and H. Ibach, Surf. Sci. **319**, 95 (1994).

[9] M. Jaeger, K. Kuhlenbeck, H.J. Freund, M. Wuttig, W. Hofmann, R. Franchy and H. Ibach, Surf. Sci. **259**, 235 (1991).

[10] R. Franchy, J. Masuch and P. Gassmann, Appl. Surf. Sci. **93**, 317 (1996).

[11] I. Costina, PhD Thesis, Heinrich-Heine-Universität Düsseldorf, 2002.

[12] V. Podgursky, I. Costina and R. Franchy, Appl. Surf. Sci. **206**, 29 (2003).

[13] U. Bardi, A. Atrei and G. Rovida, Surf. Sci. **268**, 87 (1992).

[14] C. Becker, J. Kandler, H. Raaf, T. Pelster, M. Draeger, M. Tanemura and K. Wandelt, J. Vac. Sci. Technol. A **16**, 1000 (1998).

[15] J.L. Erskine and R.L. Strong, Phys. Rev. B **25**, 5547 (1982).

[16] Y. Wu, H.-S. Tao, E. Garfunkel, Th.E. Madey and N.D. Shinn, Surf. Sci. **336**, 123 (1995).

[17] M.B. Lee, J.H. Lee, B.G. Frederick and N.V. Richardson, Surf. Sci. **448**, L207 (2000).

[18] Y. Wu, E. Garfunkel and Th.E. Madey, Surf. Sci. **365**, 337 (1996).

[19] P.J. Chen, M.L. Colaianni and J.T. Yates Jr, Phys. Rev. B **41**, 8025 (1990).

[20] P.J. Chen and D.W. Goodman, Surf. Sci. **312**, L767 (1994).

[21] Y.S. Dedkov, M. Fonin, U. Rüdiger and G. Güntherodt, Appl. Phys. Lett. **81**, 2584 (2002).

[22] Y. Jeliazova and R. Franchy, Appl. Surf. Sci. **187**, 51 (2002).

[23] P. Gassmann, PhD Thesis, RWTH Aachen, 1996.

[24] M. Eumann, G. Schmitz and R. Franchy, Appl. Phys. Lett. **72**, 3440 (1998).

[25] G. Schmitz, P. Gassmann and R. Franchy, J. Appl. Phys. **83**, 2533 (1998).

[26] R. Franchy, M. Eumann and G. Schmitz, Surf. Sci. **470**, 337 (2001).

[27] F.M. Pan, C. Pflitsch, R. David, L.K. Verheij and R. Franchy, Surf. Sci. **478**, 191 (2001).

[28] F.M. Pan, Pflitsch, R. David, L.K. Verheij and R. Franchy, Surf. Sci. **490**, L609 (2001).

[29] F.M. Pan, R. David, L.K. Verheij and R. Franchy, Thin Solid Films **400**, 22 (2001).

[30] G. Ertl and J. Küppers, *Low Energy Electrons and Surface Cchemistry* (VCH Verlagsgesellschaft, Weinheim, 1985).

[31] H. Lüth, *Surfaces and Interfaces of Solids* (Springer, Berlin, 1993).

[32] Y.M. Jeliazova, PhD Thesis, Heinrich-Heine-Universität Düsseldorf, 2002.

[33] L.E. Davis, N.C. MacDonald, P.W. Palmberg, G.E. Riach and R.E. Weber, *Handbook of Auger Electron Spectroscopy* (Physical Electronics Industries, Eden Prairie, 1976).

[34] S. Tanuma, C.J. Powell and D.R. Penn, Surf. Interface Anal. **17**, 911 (1991).

[35] S. Tanuma, C.J. Powell and D.R. Penn, Surf. Interface Anal. **17**, 927 (1991).

[36] C. Davisson and L. Germer, Phys. Rev. **30**, 705 (1927).

[37] C. Davisson and L. Germer, Rev. Sci. Inst. **31**, 112 (1960).

[38] L. de Brogli, Phil. Mag. **47**, 446 (1924).

[39] E.A. Wood, J. Appl. Phys. **35**, 1306 (1964).

[40] H. Ibach and D.L. Mills, *Electron Energy Loss Spectroscopy and Surface Vibrations* (Academic Press, New York, 1982).

[41] H. Ibach, *Electron Energy Loss Spectroscopy – The Technology of High Performance* (Springer, Berlin, 1991).

[42] G. Binnig, H. Rohrer, Ch. Gerber and E. Weibel, Appl. Phys. Lett. **40**, 178 (1982).

[43] G. Binnig, H. Rohrer, Ch. Gerber and E. Weibel, Phys. Rev. Lett. **49**, 57 (1982).

[44] R.H. Fowler and L.W. Nordheim, Proc. Roy. Soc. A **119**, 173 (1928).

[45] J. Tersoff and D.R. Hamann, Phys. Rev. Lett. **50**, 1998 (1983).

[46] J. Tersoff and D.R. Hamann, Phys. Rev. B **31**, 805 (1985).

[47] M. Bäumer and H.J. Freund, Prog. Surf. Sci. **61**, 127 (1999).

[48] T. Bertrams, A. Brodde and H. Neddermeyer, J. Vac. Sci. Technol. B **12**, 2122 (1994).

[49] U. Dürig, O. Zuger and D.W. Pohl, J. Microsc. **152**, 259 (1988).

[50] J.A. Stroscio, R.M. Feenstra and A.P. Fein, J. Vac. Sci. Technol. A **5**, 838 (1987).

[51] N.D. Lang, Phys. Rev. B **34**, 5947 (1986).

[52] R.M. Feenstra, J.A. Stroscio and A.P. Fein, Surf. Sci. **181**, 295 (1987).

[53] D.A. Bonnell (Ed.), *Scanning Probe Microscopy and Spectroscopy* (Wiley-VCH, New York, 2001).

[54] J.A. Stroscio, R.M. Feenstra and A.P. Fein, Phys. Rev. Lett. **57**, 2579 (1986).

[55] T.B. Massalski, *Binary Alloy Phase Diagrams* (American Society for Metals, Metals Park, OH, 1986).

[56] S.H. Lu, D. Tian, Z.Q. Wang, Y.S. Li and F. Jona, Solid State Comm. **67**, 325 (1988).

[57] D.J. O'Connor, M. Draeger, A.M. Molenbroek and Y.G. Shen, Surf. Sci. **357–358**, 202 (1996).

[58] A. Paciaroni, C. Petrillo and F. Sacchetti, J. Phys. (Paris) **7**, 865 (1997).

[59] M. Hansen, *Constitution of Binary Alloys* (McGraw-Hill, New York, 1958).

[60] F.A. Shunk, *Constitution of Binary Alloys, Second Supplement* (McGraw-Hill, New York, 1969).

[61] R.P. Elliot, *Constitution of Binary Alloys, First Supplement* (McGraw-Hill, New York, 1965).

[62] N.V. Ageev, *Handbook of Binary Metallic Systems Vol. 1* (Israel Program for Scientific Translations, Jerusalem, 1966).

[63] C. Greville, *Encyclopædia Britannica, 11. ed* (Encyclopædia Britannica Inc., Chicago, 1910).

[64] B. Lippens and S. Steggerda, *Physical and Chemical Aspects of Absorbants and Catalysts* (Academic Press, New York, 1970).

[65] Y.T. Chu, C.W.W.J.B. Bates and G.C. Farlow, J. Appl. Phys. **64**, 3727 (1988).

[66] H.J. v. Beek and E.J. Mittemeijer, Thin Solid Films **122**, 131 (1984).

[67] M. Liehr, P.A. Thiry, J.J. Pireaux and R. Caudano, J. Vac. Sci. Technol. A **2**, 1079 (1984).

[68] Y. Wu, E. Garfunkel and Th.E. Madey, J. Vac. Sci. Technol. A **14**, 2554 (1996).

[69] M. Fleischer and H. Meixner, Sensors and Actuators B **5**, 115 (1992).

[70] Z. Li, C. de Groot and J.S. Moodera, Appl. Phys. Lett. **77**, 3630 (2000).

[71] J.A. Kohn, G. Katz and J.D. Border, Am. Minral. **42**, 398 (1957).

[72] S. Geller, J. Chem. Phys. **33**, 676 (1960).

[73] G. Schmitz, P. Gassmann and R. Franchy, Surf. Sci. **397**, 339 (1998).

[74] N.S. Stoloff, C.T. Liu and S.C. Deevi, Intermetallics **8**, 1313 (2000).

[75] H.J. Freund and E. Umbach, *Adsorption on Ordered Surfaces of Ionic Solids and Thin Films* (Springer, Heidelberg, 1993).

[76] P.L.J. Gunter, J.W.H. Niemantsverdriet, F.H. Ribeiro and G.A. Somorjai, Catal. Rev. Sci. Eng. **39**, 77 (1997).

[77] J.S. Moodera and L.R. Kinder, J. Appl. Phys. **79**, 4724 (1996).

[78] E. Hirota, H. Sakakima and K. Inomata, *Giant Magneto-Resistance Devices* (Teubner, Berlin, 2002).

[79] W.J. Gallagher, E.J. Gallagher, S.S.P. Parkin, Yu Lu, X.P. Bian, A. Marley, K.P. Roche, R.A. Altman, S.A. Rishton, T.M. Shaw and G. Xiao, J. Appl. Phys. **81**, 3741 (1997).

[80] Ph. Mavropoulos, N. Papanikolaou and P.H. Dederichs, Phys. Rev. Lett. **85**, 1988 (2000).

[81] R. Franchy, Surf. Sci. Rep. **38**, 195 (2000).

[82] Y.G. Shen, D.J. O'Connor and R.J. MacDonald, Surf. Interface Anal. **17**, 903 (1991).

[83] G.F. Cotterill, H. Niehus and D.J. O'Connor, Surf. Rev. Lett. **3**, 1355 (1996).

[84] A. Venezia and C. Loxton, Surf. Sci. **194**, 136 (1988).

[85] R.-P. Blum and H. Niehus, Appl. Phys. A **66**, S529 (1998).

[86] R.-P. Blum, D. Ahlbehrendt and H. Niehuis, Surf. Sci. **396**, 176 (1998).

[87] V. Rose, V. Podgursky, I. Costina and R. Franchy, Surf. Sci. **541**, 128 (2003).

[88] H. Graupner, L. Hammer, K. Heinz and D.M. Zehner, Surf. Sci. **380**, 335 (1997).

[89] H. Boeve, J.D. Boeck and G. Borghs, J. Appl. Phys. **89**, 482 (2001).

[90] E. Girgis, H. Boeve, J.D. Boeck, J. Schelten, P. Rottländer, H. Kohlstedt and P. Grünberg, J. Mag. Mag. Mat. **222**, 133 (2000).

[91] J.J. Sun, R.C. Sousa, T.T.P. Galvão, V. Soares, T.S. Plaskett and P.P. Freitas, J. Appl. Phys. **83**, 6694 (1998).

[92] M. Vermeersch, F. Malengreau, R. Sporken and R. Caudano, Surf. Sci. **323**, 175 (1995).

[93] S.G. Addepalli, B. Ekstrom, N.P. Magtoto, J.-S. Lin and J.A. Kelber, Surf. Sci. **442**, 385 (1999).

[94] R. Jansen, B. Davis, C.T. Tanaka and J.S. Moodera, Surf. Sci. **463**, 109 (2000).

[95] P. Gassmann, R. Franchy and H. Ibach, J. Electron Spectrosc. Relat. Phenom. **64/65**, 315 (1993).

[96] R. Franchy, G. Schmitz, P. Gassmann and F. Bartolucci, Appl. Phys. A **65**, 551 (1997).

[97] D.R. Jennison, C. Verdozzi, P.A. Schultz and M.P. Sears, Phys. Rev. B **59**, R15605 (1999).

[98] I. Costina and R. Franchy, Appl. Phys. Lett. **78**, 4139 (2001).

[99] A. Sandell, J. Libuda, M. Bäumer and H.-J. Freund, Surf. Sci. **346**, 108 (1996).

[100] J. Toofan and P.R. Watson, Surf. Sci. **401**, 162 (1998).

[101] Q. Guo, D.Y. Kim, S.C. Street and D.W. Goodman, J. Vac. Sci. Technol. A **17**, 1887 (1999).

[102] C. Palacio and A. Arranz, J. Phys. Chem. B **104**, 9647 (2000).

[103] M. Klimenkov, S. Nepijko, H. Kuhlenbeck and H.-J. Freund, Surf. Sci. **385**, 66 (1997).

[104] A. Rosenhahn, J. Schneider, C. Becker and K. Wandelt, Appl. Surf. Sci. **142**, 169 (1999).

[105] A. Rosenhahn, J. Schneider, J. Kandler, C. Becker and K. Wandelt, Surf. Sci. **433–435**, 705 (1999).

[106] N. Cabrera and N.F. Mott, Rep. Prog. Phys. **163**, 163 (1948–1949).

[107] E.Y. Chen, R. Whig, J.M. Slaughter, D. Cronk, J. Goggin, G. Steiner and J. Tehrani, J. Appl. Phys. **87**, 6061 (2000).

[108] R. Manaila, A. Dévényi and E. Candet, Thin Solid Films **116**, 289 (1984).

[109] G. Gutierrez and B. Johansson, Phys. Rev. B **65**, 104202 (2002).

[110] H.D. Megaw, *Crystal Structures: A Working Approach* (Sanders, Philadelphia, 1973).

[111] V. Rose, Master's thesis, RWTH Aachen, 2002.

[112] M. Wutz, W. Adam and K. Jousten, *Handbuch der Vakuumphysik* (Vieweg, Braunschweig, 2000).

[113] A. Wehner, Y. Jeliazova and R. Franchy, Surf. Sci, **531**, 287 (2003).

[114] M. Bowen, V. Cros, F. Petroff, A. Fert, C.M. Boubeta, J.L. Costa-Krämer, J.V. Anguita, A. Cebollada, F. Briones, J.M. de Teresa, Morellón, M.R. Ibarra, F. Güell, Peiró and A. Cornet, Appl. Phys. Lett. **79**, 1655 (2001).

[115] M. Wulfhekel, M. Klaua, D. Ullmann, F. Zavaliche, J. Kirschner, R. Urban, T. Monchesky and B. Heinrich, Appl. Phys. Lett. **78**, 509 (2001).

[116] V. Podgursky, I. Costina and R. Franchy, Surf. Sci. **529**, 419 (2003).

[117] M.M. Thiam, V. Nehasil, V. Matolín and B. Gruzza, Surf. Sci. **487**, 231 (2001).

[118] C. Becker, K. von Bergmann, A. Rosenhahn, J. Schneider and K. Wandelt, Surf. Sci. **486**, L443 (2001).

[119] A. Wiltner, A. Rosenhahn, J. Schneider, C. Becker, P. Pervan, M. Milun, M. Kralj and K. Wandelt, Thin Solid Films **400**, 71 (2001).

[120] C.L. Pang, H. Raza, S.A. Haycock and G. Thornton, Surf. Sci. **460**, L510 (2000).

[121] M. Heemeier, S. Stempel, Sh.K. Shaikhutdinov, J. Libuda, M. Bäumer, R.J. Oldman, S.D. Jackson and H.-J. Freund, Surf. Sci. **523**, 103 (2003).

[122] A. Gupta, X.W. Li and G. Xiao, Appl. Phys. Lett. **78**, 1894 (2001).

[123] U. May, K. Samm, H. Kittur, J. Hauch, R. Calarco, U. Rüdiger and G. Güntherodt, Appl. Phys. Lett. **78**, 2026 (2001).

[124] H. Brückl, J. Schmalhorst, G. Reiss, G. Gieres and J. Wecker, Appl. Phys. Lett. **78**, 1113 (2001).

[125] B. Gruschko, R. Wittemberg, K. Bickmann and C. Freiburg, J. Alloys Comp. **233**, 279 (1996).

[126] W.F. Egelhoff Jr., P.J. Chen, R.D. McMichael, C.J. Powell, R.D. Deslattes, F.G. Serpa and R.D. Gomez, J. Appl. Phys. **89**, 5209 (2001).

[127] N.R. Shivaparan, M.A. Teter and R.J. Smith, Surf. Sci. **476**, 152 (2001).

[128] G.V. Golubkova, O.I. Lomovsky, Y.S. Kwon, A.A. Vlasov and A.L. Chuilin, J. Alloys Comp. **351**, 101 (2003).

[129] D.R. Lide, *Handbook of Chemistry and Physics* (CRC Press, Boca Raton, Fl, 1994).

[130] M. Hassel and H.-J. Freund, Surf. Sci. **325**, 163 (1995).

[131] F.G. Allen and G.W. Gobeli, Phys. Rev. **127**, 150 (1962).

[132] G. Ciarotti, S. Nannarone, R. Pastore and P. Chiaradia, Phys. Rev. B **4**, 3398 (1971).

[133] P. Chiaradia, A. Cricenti, S. Selci and G. Chiarotti, Phys. Rev. Lett. **52**, 1145 (1984).

[134] F.J. Himpsel, P. Heimann and D.E. Eastmann, Phys. Rev. B **24**, 2003 (1981).

[135] R.I. Uhrberg, G.V. Hansson, J.M. Nicholls and S.A. Flodström, Phys. Rev. Lett. **48**, 1032 (1982).

[136] P. Mårtensson, A. Cricenti and G.V. Hansson, Phys. Rev. B **32**, 6959 (1985).

[137] D. Straub, L. Ley and F.J. Himpsel, Phys. Rev. Lett. **54**, 142 (1985).

[138] K.C Pandey, Phys. Rev. Lett. **47**, 1913 (1981).

[139] J.E. Northrup and M.L. Cohen, Phys. Rev. Lett. **49**, 1349 (1982).

[140] J.M. Layet, J.Y. Hoarau, H. Lüth and J. Derrien, Phys. Rev. B **30**, 7355 (1984).

[141] R.S. Becker, J.A. Golovchenko, D.R. Hamann and B.S. Swartzentruber, Phys. Rev. Lett. **55**, 2032 (1985).

[142] R.J. Hamers, R.M. Tromp and J.E. Demuth, Phys. Rev. Lett. **56**, 1972 (1986).

[143] R.J. Hamers, R.M. Tromp and J.E. Demuth, Surf. Sci. **181**, 346 (1987).

[144] S. Heike, S. Watanabe, Y. Wada and T. Hashizume, Phys. Rev. Lett. **81**, 890 (1998).

[145] F. Xie, M. Sun and P. von Blanckenhagen, Surf. Sci. **454–456**, 1031 (2000).

[146] F.S. Ohuchi and R.H. French, J. Vac. Sci. Technol. A **6**, 1695 (1987).

[147] G. Binnig, H. Rohrer, Ch. Gerber and E. Weibel, Phys. Rev. Lett. **50**, 120 (1983).

[148] J.A. Venables, *Introduction to Surface and Thin Film Processes* (Cambridge University Press, Cambridge, UK, 2000).

[149] K. Takayanagi, Y. Tanichiro, M. Takahashi and S. Takahashi, Surf. Sci. **164**, 367 (1985).

[150] F.K. Robinson, P.H. Waskiewicz, P.H. Fuoss and L.J. Norton, Phys. Rev. B **37**, 4325 (1988).

[151] S.Y. Tong, H. Huang, C.M. Wei, W.E. Packard, F.K. Men, G. Glander and M.B. Webb, J. Vac. Sci. Technol. A **6**, 615 (1988).

[152] I. Stich, M.C. Pyane and R.D. King-Smith, Phys. Rev. Lett. **68**, 1351 (1992).

[153] K.D. Brommer, M. Needels, B.E. Larson and J.D. Joannopoulos, Phys. Rev. Lett. **68**, 1355 (1992).

[154] D.E. Eastman, F.J. Himpsel and F.J. van der Veen, Solid State Commun. **35**, 345 (1980).

[155] G.V. Hansson, R.I.G. Uhrberg and S.A. Flodström, J. Vac. Sci. Technol. **16**, 1287 (1979).

[156] P. Martensson, W.X. Ni, G.V. Hansson, J.M. Nicholls and B. Reihl, Phys. Rev. B **36**, 5974 (1987).

[157] F. Houzay, G.M. Guichar, R. Pinchaux and Y. Petroff, J. Vac. Sci. Technol. **18**, 860 (1981).

[158] T. Yokotsuka, S. Kono, S. Suzuki and T. Sagawa, Solid State Commun. **46**, 401 (1983).

[159] P. Villars and L.D. Calvert, *Pearson's Handbook of Crystallographic Data for Intermetallic Phases* (ASM, Metals Park, Ohio, 1985).

[160] C. Pflitsch, PhD Thesis, Heinrich-Heine-Universität Düsseldorf, 2001.

[161] D.A. Kovács, PhD Thesis, Heinrich-Heine-Universität Düsseldorf, 2003.

[162] Y. Kuk, F.M. Chua, P.J. Silverman and J.A. Meyer, Phys. Rev. B **41**, 12393 (1990).

[163] M. Giesen-Seibert, F. Schmitz, R. Jentjens and H. Ibach, Surf. Sci. **329**, 427 (1995).

[164] J. Åhmann, G. Svensson and J. Albertsson, Acta Crystallogr. C **52**, 1336 (1996).

[165] S. Adachi, J. Appl. Phys. **58**, R1 (1985).

[166] Ch. Hagendorf., R. Shantyr, K. Meinel, K.-M. Schindler and H. Neddermeyer, Surf. Sci. **532–535**, 346 (2003).

Acknowledgements

First I would like to express my gratitude to my supervisor Prof. R. Franchy for introducing me to the field of surface science, the good working atmosphere, and his constant support. The frequent and open discussions were of utmost value for this work.

I would like to thank Prof. H. Ibach for giving me the chance to make my PhD Thesis in the Institut für Schichten und Grenzflächen (ISG 3) of the Forschungszentrum Jülich.

I am grateful to Prof. K. Schierbaum for accepting to be the co-referee of my thesis.

I am grateful to Dr. R. David for advice concerning technical problems.

Special thanks are addressed to Mrs. Ch. Elsaesser for technical assistance during the scanning tunneling microscopy / spectroscopy measurements and to C. Steufmehl for her support.

I thank U. Linke for the fast preparation of high-quality single crystals and useful tips.

I thank also Mr. D. Strobl and all members of the mechanical workshop as well as Mr. R. Rausch and the members of the electrical workshop for rapidly and precisely done work. Thanks are also addressed to Mr. N. Tiefes and his group for support concerning PCs.

I would also like to express my gratitude to the Postdocs and PhD students of the ISG for the support and pleasant atmosphere they created. I especially thank: T. Balster, S. Bergfeld, C. Bombis, J. Costina, S. Dieluweit, J. Ikonomov, Y. Jeliazova, D.-A. Kovacs, D. Mayer, V. Podgursky, V. Rose and S. M. van Eek.